

**Quarterly Technical Report**

**Solid State Research**

1993:1

---

**Lincoln Laboratory**

MASSACHUSETTS INSTITUTE OF TECHNOLOGY

*LEXINGTON, MASSACHUSETTS*



---

Prepared for the Department of the Air Force under Contract F19628-90-C-0002.

Approved for public release; distribution is unlimited.

*new*

ADA274177



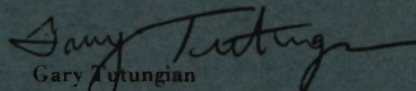
This report is based on studies performed at Lincoln Laboratory, a center for research operated by Massachusetts Institute of Technology. The work was sponsored by the Department of the Air Force under Contract F19628-90-C-0002.

This report may be reproduced to satisfy needs of U.S. Government agencies.

The ESC Public Affairs Office has reviewed this report, and it is releasable to the National Technical Information Service, where it will be available to the general public, including foreign nationals.

This technical report has been reviewed and is approved for publication.

FOR THE COMMANDER



Gary Tutungian  
Administrative Contracting Officer  
Directorate of Contracted Support Management

Non-Lincoln Recipients

PLEASE DO NOT RETURN

Permission is given to destroy this document  
when it is no longer needed.

MASSACHUSETTS INSTITUTE OF TECHNOLOGY  
LINCOLN LABORATORY

**SOLID STATE RESEARCH**

**QUARTERLY TECHNICAL REPORT**

1 NOVEMBER 1992 — 31 JANUARY 1993

30 JULY 1993

Approved for public release; distribution is unlimited.

LEXINGTON

MASSACHUSETTS

## **ABSTRACT**

This report covers in detail the research work of the Solid State Division at Lincoln Laboratory for the period 1 November 1992 through 31 January 1993. The topics covered are Electrooptical Devices, Quantum Electronics, Materials Research, Submicrometer Technology, High Speed Electronics, Microelectronics, and Analog Device Technology. Funding is provided primarily by the Air Force, with additional support provided by the Army, DARPA, Navy, SDIO, and NASA.



## TABLE OF CONTENTS

Abstract	iii
List of Illustrations	vii
List of Tables	xi
Introduction	xiii
Reports on Solid State Research	xv
Organization	xxiii
<b>1. ELECTROOPTICAL DEVICES</b>	<b>1</b>
1.1 Fabrication of Anamorphic Microlenses and Collimation of Tapered-Laser Output	1
1.2 Semiconductor Filters with Wide Acceptance Angle and Narrow Bandwidth	5
<b>2. QUANTUM ELECTRONICS</b>	<b>11</b>
2.1 Calculated Room-Temperature Threshold Current Densities for Visible II-VI ZnCdSe/ZnSe Quantum-Well Diode Lasers	11
2.2 Coherent Coupling of Microchip Arrays	17
2.3 Effects of Phase Errors on Coherent Emitter Arrays	20
<b>3. MATERIALS RESEARCH</b>	<b>25</b>
3.1 Reduction of Optical Cross Talk in PtSi Schottky-Barrier Infrared Focal Plane Arrays	25
3.2 Barrier-Thickness Dependence of Photoluminescence for Strained-Layer InGaAs/GaAs Coupled Quantum Wells	28
3.3 Growth and Characterization of MBE-Grown Epitaxial Bi <sub>0.9</sub> Sb <sub>0.1</sub> Films	32
<b>4. SUBMICROMETER TECHNOLOGY</b>	<b>37</b>
4.1 Optical Materials for Use with Excimer Lasers	37
4.2 High-Conductance, Low-Leakage Diamond Schottky Diodes	39
<b>5. HIGH SPEED ELECTRONICS</b>	<b>47</b>
5.1 Detection of Nanosecond Far-Infrared Pulses at Cryogenic Temperatures Using Multiple-Quantum-Well Structures	47

## TABLE OF CONTENTS (Continued)

6.	MICROELECTRONICS	53
6.1	Improved Ultraviolet Response of Silicon CCD Imagers	53
6.2	Epitaxial Silicon JFET Amplifier for Low-Noise Charge Detection	55
7.	ANALOG DEVICE TECHNOLOGY	61
7.1	VME-Bus-Compatible Board for an Image-Feature Extractor	61
7.2	Demonstration of a Prototype High- $T_c$ Superconductive Wideband Real-Time Spectrum-Analysis Receiver	64

## LIST OF ILLUSTRATIONS

Figure No.		Page
1-1	Collimation of astigmatic output from a tapered laser using the anamorphic microlens.	1
1-2	Stages in formation of the microlens: (a) lithographic mask, (b) etched mesa pattern, and (c) lens formed after mass transport. Part (a) is an ordinary optical micrograph, and parts (b) and (c) are perspective views obtained by using a scanning electron microscope.	2
1-3	Stylus surface profiles of an anamorphic microlens along the two major directions (curves) compared with the ideal profiles from calculations (points).	3
1-4	Far-field pattern of a narrow, nearly round beam obtained in collimation of tapered-laser output using the anamorphic microlens.	4
1-5	Calculated filter transmission for collimated light with input angles of 0 and 10°, for filters with effective indices of 2.1 and 3.2.	6
1-6	(a) Schematic of the layer structure for the quarter-wave-shifted multilayer dielectric thin-film filter at 980-nm wavelength. (b) Measured central transmission passband for the 61-layer GaAs/AlAs filter structure. The measurement spot size is < 1 mm in diameter, and the input cone angle ~ 2°.	7
1-7	Filter transmission spectrum for the 61-layer GaAs/AlAs filter structure. The filter was mounted on a glass substrate and the GaAs substrate removed. The measurement spot size was ~ 4 mm in diameter. The central transmission band peak is limited by the instrument resolution of > 1 nm.	8
1-8	Filter central wavelength uniformity of 5-cm-diam wafer. The thickness uniformity is 1.2% from edge to edge.	8
2-1	Schematic diagrams for the refractive index profile of (a) a single quantum well, (b) a multiple quantum well (MQW), and (c) a step-index separate-confinement heterostructure (STINSCH).	12
2-2	(a) Calculated maximum room-temperature gain coefficient $g_{\max}$ vs injected carrier density $n_{\text{inj}}$ for 10-nm-thick ZnCdSe/ZnSe and GaAs/GaAlAs single quantum wells, and (b) $g_{\max}$ vs nominal current density $J_{\text{nom}}$ for the same structures as in (a).	13
2-3	Calculated room-temperature threshold current densities $J_{\text{th}}$ vs quantum-well width $L_w$ for MQWs with barrier layer thickness $L_b$ of 10 nm. The structures in (a) and (b) are ZnCdSe/ZnSe and GaAs/GaAlAs, respectively.	14



## LIST OF ILLUSTRATIONS (Continued)

Figure No.		Page
2-4	Comparison of the calculated values (solid curve) of the threshold current density $J_{th}$ for ZnCdSe/ZnSe MQWs ( $N_w = 6$ , $L_w = 6$ nm, and $L_b = 10$ nm) with the experimental data of Jeon et al. [2] (points) at $T = 200$ , 250, and 273 K. The values of the band parameters were assumed to be temperature independent.	16
2-5	Calculated room-temperature threshold current densities $J_{th}$ vs the refractive index step $\Delta n = \mu_c - \mu_b$ for ZnCdSe/ZnSe and GaAs/GaAlAs quantum wells with an optimized STINSCH structure and $L_w = 10$ nm.	16
2-6	Locking range for two microchip elements vs the element separation. The curve represents a theoretical fit to the data, with parameters $w = 180$ $\mu$ m and $\delta f = 400$ MHz.	18
2-7	Schematic diagram of microchip array coupled using an external cavity.	18
2-8	Intensity profiles at output coupler for filter in and out.	19
2-9	Contour plots of Strehl ratios $S_G^{uncorr,1D}$ and $S_G^{corr,1D}$ as a function of the number of emitters and the phase-error standard deviation for one-dimensional arrays with (a) uncorrelated phase errors and (b) correlated phase errors.	22
3-1	(a) Schematic diagram showing optical cross talk in back-illuminated focal plane array (FPA). (b) Cruciform pattern formed from the image of a high-intensity source as a result of optical cross talk.	26
3-2	(a) Schematic diagram showing suppression of optical cross talk in front-illuminated FPA. (b) Medium-wavelength infrared image of the same high-intensity source as in Figure 3-1(b) but absent of the cruciform pattern.	27
3-3	Schematic diagram showing reduction of optical cross talk in thin back-illuminated FPA.	27
3-4	Horizontal video line outputs of high-intensity point-source imagery obtained from (a) a thick PtSi FPA and (b) a thin PtSi FPA.	28
3-5	Schematic structure of InGaAs/GaAs multiple-quantum-well (MQW) samples.	29
3-6	Double-crystal x-ray diffraction rocking curves of InGaAs/GaAs MQW structure: (a) simulation and (b) experiment.	30

## LIST OF ILLUSTRATIONS (Continued)

Figure No.		Page
3-7	Room-temperature emission wavelength as a function of GaAs barrier layer thickness for three-quantum-well samples with $x = 0.3$ and $t_w = 2.0$ nm. The open circles at zero and infinite barrier thickness are results for single-quantum-well samples with $t_w = 6$ and 2 nm, respectively.	31
3-8	Low-temperature (6 K) photoluminescence linewidth as a function of GaAs barrier layer thickness for the same samples as in Figure 3-7.	32
3-9	[444] x-ray diffraction lines for (a) a (111) BaF <sub>2</sub> substrate and (b) an early Bi <sub>0.9</sub> Sb <sub>0.1</sub> film grown by molecular beam epitaxy (MBE).	34
3-10	Optical micrographs of (a) a cleaved cross section of a Bi <sub>0.9</sub> Sb <sub>0.1</sub> MBE-grown film on a (111) BaF <sub>2</sub> substrate and (b) the as-grown surface of the Bi <sub>0.9</sub> Sb <sub>0.1</sub> film.	35
4-1	Plot of 193-nm-induced color centers (left-hand ordinate) and birefringence (right-hand ordinate) in a 1-cm-thick sample of Suprasil 2, as a function of the sample temperature during irradiation. The exposure conditions were $1.4 \times 10^6$ pulses, $17 \text{ mJ cm}^{-2}/\text{pulse}$ .	39
4-2	Annealing behavior of 193-nm-induced color centers (left-hand ordinate) and birefringence (right-hand ordinate) in Suprasil 2. The irradiation was performed at room temperature. The two ordinates were normalized to their respective values after exposure and prior to heating.	39
4-3	Pre-irradiation absorption coefficient at 193 nm of standard Corning 7940, as a function of the sample's location in the boule (left-hand ordinate). The broken line represents the density of laser-induced color centers generated by $2 \times 10^6$ pulses at $50 \text{ mJ cm}^{-2}/\text{pulse}$ in the same samples (right-hand ordinate). While the top of the boule is more transparent and more damage resistant, there does not seem to be a one-to-one correlation between initial absorption and amount of color center formation.	40
4-4	Color centers induced in CaF <sub>2</sub> with a 193-nm laser at a fluence of $100 \text{ mJ cm}^{-2}/\text{pulse}$ . The three grades form color centers at rates differing by 2 orders of magnitude, as shown by the scaling factors next to the curves and the number of pulses required to obtain each curve.	40
4-5	Leakage currents for $20 \times 500\text{-}\mu\text{m}$ Al Schottky diodes fabricated on (111)-oriented substrate, for several plasma treatments. In this plot the measured currents were divided by the perimeter of the diodes.	42

## LIST OF ILLUSTRATIONS (Continued)

Figure No.		Page
4-6	Inverse of a Hg Schottky diode capacitance squared as a function of bias voltage, for several annealing temperatures. The inset compares the current-voltage characteristics of the forward-biased Hg Schottky diodes before and after annealing at 660°C for 2 s. Before fabricating the diode, this diamond substrate was etched using ion-beam-assisted etching, to a depth of $\sim 1 \mu\text{m}$ , with a 0.1-mA ion beam composed of 500-eV $\text{Xe}^+$ in the presence of $\text{NO}_2$ . This etching was used to form a 1.2- $\mu\text{m}$ -thick compensated layer.	43
4-7	Current-voltage curve of a diamond-Hg Schottky diode at 110°C and for comparison a Pt-PtSi-Si Schottky diode at 25°C.	44
5-1	Response at $T \approx 10 \text{ K}$ to 2.6-ns-wide, 292- $\mu\text{m}$ -wavelength superradiant pulses for (a) a multiple-quantum-well (MQW) detector and (b) a Schottky diode. Source configuration: $\text{CO}_2$ pulse energy before plasma shutter, 150 mJ; plasma shutter, $p = 50 \text{ Torr}$ ; $\text{NH}_3$ , $p = 0.60 \text{ Torr}$ .	48
5-2	Response at $T \approx 90 \text{ K}$ to 2.6-ns-wide, 292- $\mu\text{m}$ -wavelength superradiant pulses for (a) an MQW detector and (b) a Schottky diode. The source configuration is the same as in Figure 5-1.	49
5-3	Responsivity as a function of wavelength for the MQW sample at $T \approx 10 \text{ K}$ . The CW laser was chopped at 200 Hz.	50
6-1	Calculated (curves) and measured (points) external quantum efficiency of back-illuminated charge-coupled device (CCD) imagers.	54
6-2	Effect of $\text{SiO}_2$ layers on quantum efficiency.	54
6-3	(a) Cross section and (b) top view of $p$ -channel charge-sense amplifier as implemented in a conventional three-phase buried-channel CCD process.	56
6-4	Operating sequence for detecting charge with the $p$ -channel junction field-effect transistor amplifier: (a) image, (b) sense, and (c) reset.	57
6-5	Transmission electron micrograph showing cross section of the epitaxial silicon layer that has been grown from seed holes in a thermal field oxide.	58
7-1	Digital control board.	62
7-2	Analog control board.	62
7-3	Example of an input/output format for the charge-coupled device (CCD) image-feature-extractor (IFE) VME board.	63



## LIST OF ILLUSTRATIONS (Continued)

Figure No.		Page
7-4	Output waveform of the CCD IFE VME board as a feature extractor. Shown at the top are feature templates.	63
7-5	Block diagram of demonstration system intended for the Navy's Second High-Temperature Superconductor Space Experiment (HTSSE II). This is a multiply-convolve chirp-transform configuration for a compressive receiver.	65
7-6	Detailed system diagram of the spectrum-analysis receiver for HTSSE II. The compressed-pulse signal, envelope-detected signal, and ECL-compatible logic signal are shown in the signal path.	66
7-7	Photograph of assembled prototype receiver components. The high- $T_c$ superconductive chirp filter, room-temperature electronics box, and power supply box are shown.	67
7-8	Screen display for slowly swept input signal. Frequency-bin data are updated at a slow rate of every 0.25 s so that a human operator can follow the display. The update rate could be much faster in an all-electronic system.	68

## LIST OF TABLES

Table No.		Page
2-1	Room-Temperature Values of the Material and Device Parameters for the GaAs/GaAlAs and ZnCdSe/ZnSe Quantum-Well Lasers	15
3-1	Some Physical Properties of MBE-Grown Epitaxial BiSb Films	36

## INTRODUCTION

### 1. ELECTROOPTICAL DEVICES

Precision large-numerical-aperture anamorphic microlenses have been fabricated by mass-transport smoothing of a set of closely spaced mesas of varying widths. The astigmatic output from a tapered laser has been collimated to an almost round beam with a nearly diffraction-limited divergence of  $0.43^\circ$ .

Precision semiconductor growth techniques have been applied to the fabrication of very narrow bandwidth (0.6 nm) optical filters, with 90% peak transmission at 980 nm. These filters have applications in fiber and free-space communications systems.

### 2. QUANTUM ELECTRONICS

Room-temperature threshold current densities for the visible II-VI ZnCdSe/ZnSe semiconductor quantum-well diode lasers have been calculated using a simple model for the quantum-well gain and spontaneous radiative recombination rate. It is shown that by tailoring the epitaxial structure for optimum optical confinement, it should be possible to achieve room-temperature operation of the ZnCdSe/ZnSe quantum-well lasers with current densities as low as  $400 \text{ A/cm}^2$  for a 1-mm cavity length and uncoated laser facets.

One-dimensional arrays of solid state microchip lasers have been coherently coupled using both nearest-neighbor and external cavity techniques. These coherently coupled arrays can be far brighter than incoherent arrays.

The effect of uncorrelated and nearest-neighbor-correlated Gaussian phase deviations on the Strehl ratios of rectangular-aperture, rectangular-grid, coherent-emitter arrays has been analyzed. Effects on far-field intensity patterns, central-lobe angular widths, and central-lobe pointing have also been calculated.

### 3. MATERIALS RESEARCH

Low-level optical cross talk, which shows up as cruciform patterns from very bright objects in PtSi Schottky-barrier infrared focal plane arrays, has been greatly reduced. In front-illuminated arrays the cross talk was eliminated by using *p-on-p*<sup>+</sup> epitaxial Si wafers to absorb the radiation transmitted by the PtSi, and in back-illuminated arrays it was greatly suppressed by thinning the wafers to about  $15 \mu\text{m}$ .

Coupling between strained-layer  $\text{In}_{0.3}\text{Ga}_{0.7}\text{As}$  quantum wells as a function of GaAs barrier thickness has been investigated by x-ray and photoluminescence (PL) measurements. In agreement with calculations, broadening of low-temperature PL linewidths was observed as well as shifts in room-temperature PL emission peaks to longer wavelengths for GaAs barrier thicknesses  $< 8 \text{ nm}$ .

Epitaxial  $\text{Bi}_{0.9}\text{Sb}_{0.1}$  films with low carrier concentrations and record high electron mobilities have been grown on barium fluoride substrates by molecular beam epitaxy. Electron mobilities as high as  $26\,000 \text{ cm}^2/\text{V s}$  at 300 K and  $665\,000 \text{ cm}^2/\text{V s}$  at 77 K were obtained for material with electron carrier concentrations as low as  $6.3 \times 10^{16} \text{ cm}^{-3}$  at 77 K.

#### **4. SUBMICROMETER TECHNOLOGY**

Synthetic ultraviolet-grade fused silica and crystalline fluorides have been evaluated for transparency and durability at 193 nm. Although most bulk materials eventually develop color centers, and fused silica also changes its density and index of refraction, the rate at which these changes occur and their magnitude vary strongly with material, grade, and other more subtle details.

Schottky diodes of Al, Au, and Hg on diamond have been characterized after various plasma treatments and thermal annealing cycles. Based on these experiments, surface passivation techniques and methods for removing subsurface compensation layers were developed that led to improved diamond Schottky diodes.

#### **5. HIGH SPEED ELECTRONICS**

Experiments with multiple-quantum-well GaAs/AlGaAs samples have shown that they are fast detectors of pulsed 100–500- $\mu\text{m}$  radiation at temperatures between 10 and 90 K. Response times  $< 1$  ns have been measured at temperatures above 77 K, offering considerable promise for developing a relatively sensitive far-infrared photodetector capable of liquid-nitrogen temperature with subnanosecond speed.

#### **6. MICROELECTRONICS**

The ultraviolet (UV) response of back-surface charge-coupled device (CCD) imagers has been improved to near theoretical limits by growing a passivating oxide on the exposed surface, implanting boron through this oxide, and annealing in a conventional furnace, rather than ion implanting into the bare Si surface and annealing with a pulsed excimer laser beam. This new technique is reproducible, stable under UV exposure, shows low dark current, low back-surface recombination of photogenerated electrons, and good antireflection-coating properties as well as near reflection-limited quantum efficiency in the UV and visible.

A *p*-channel junction field-effect transistor (JFET), to be fabricated in selectively grown single-crystal silicon regions, has been designed for low-noise and high-frequency charge detection. The proposed device structure has been simulated, and  $n^+/p$  junction diodes have been fabricated and electrically characterized to verify the feasibility of the JFET amplifier.

#### **7. ANALOG DEVICE TECHNOLOGY**

A CCD image-feature extractor has been embedded on a VME-bus-compatible board. The board can be used as a high-speed co-processor with a host computer to speed up simulations in various image and neural network applications.

A real-time spectrum-analysis receiver with a 3-GHz instantaneous analysis bandwidth has been demonstrated using high- $T_c$  superconductive tapped-delay-line chirp filters. This compressive receiver is a prototype of the receiver to be space qualified for use in the Navy's Second High-Temperature Superconductor Space Experiment (HTSSE II).



## REPORTS ON SOLID STATE RESEARCH

1 NOVEMBER 1992 THROUGH 31 JANUARY 1993

### PUBLICATIONS

Flow Regime Map and Deposition Rate Uniformity in Vertical Rotating-Disk OMVPE Reactors	C. R. Biber* C. A. Wang S. Motakef*	<i>J. Cryst. Growth</i> <b>123</b> , 545 (1992)
Laser-Chemical Three-Dimensional Writing for Microelectromechanics and Application to Standard-Cell Microfluidics	T. M. Bloomstein D. J. Ehrlich	<i>J. Vac. Sci. Technol. B</i> <b>10</b> , 2671 (1992)
Stereo Laser Micromachining of Silicon	T. M. Bloomstein D. J. Ehrlich	<i>Appl. Phys. Lett.</i> <b>61</b> , 708 (1992)
Photonic-Crystal Planar Antennas	E. R. Brown C. D. Parker E. Yablonovitch*	<i>Opt. Photon. News</i> <b>3</b> (12), 37 (1992)
Real-Time CCD-Based Neural Network Systems for Pattern Recognition Applications	A. M. Chiang J. R. LaFranchise	<i>1992 Government Microcircuit Applications Conf. Dig. of Papers</i> , Vol. 18, p. 285
Nonlinear Microwave Electrodynamics of Superconducting NbN and Nb Thin Films	C. C. Chin* D. E. Oates G. Dresselhaus* M. S. Dresselhaus*	<i>Advances in Superconductivity IV: Proc. 4th Int. Symp. on Superconductivity</i> , H. Hayakawa and N. Koshizuka, eds. (Springer-Verlag, Tokyo, 1992), p. 167
Optimizing the Efficiency and Stored Energy in Quasi-Three-Level Lasers	T. Y. Fan	<i>IEEE J. Quantum Electron.</i> <b>28</b> , 2692 (1992)

---

\*Author not at Lincoln Laboratory.

Sr <sub>2</sub> AlTaO <sub>6</sub> Films for Multilayer High-Temperature Superconducting Device Applications	A. T. Findikoglu* C. Doughty* S. Bhattacharya* Q. Li* X. X. Xi* T. Venkatesan* R. E. Fahey A. J. Strauss J. M. Phillips*	<i>Appl. Phys. Lett.</i> <b>61</b> , 1718 (1992)
Diamond and Diamondlike Carbon	M. W. Geis	In <i>Encyclopedia of Applied Physics</i> , Vol. 5 (VCH Publishers, New York, 1993), p. 1
InGaAs/GaInAsP/GaInP Strained-Layer Quantum Well Separate-Confinement Heterostructures Grown by OMVPE	S. H. Groves	<i>J. Cryst. Growth</i> <b>124</b> , 747 (1992)
Surface Imaging Resists for 193 nm Lithography	D. W. Johnson* M. A. Hartney	<i>Jpn. J. Appl. Phys. Pt. 1</i> <b>31</b> , 4321 (1992)
Wet-Developed Bilayer Resists for 193-nm Excimer Laser Lithography	R. R. Kunz M. W. Horn P. A. Bianconi* D. A. Smith* J. R. Eshelman*	<i>J. Vac. Sci. Technol. B</i> <b>10</b> , 2554 (1992)
Surface-Imaged Silicon Polymers for 193-nm Excimer Laser Lithography	R. R. Kunz M. W. Horn G. M. Wallraff* P. A. Bianconi* R. D. Miller* R. B. Goodman D. A. Smith* J. R. Eshelman* E. J. Ginsberg*	<i>Jpn. J. Appl. Phys. Pt. 1</i> <b>31</b> , 4327 (1992)

---

\*Author not at Lincoln Laboratory.

- |  |  |   |
|--|--|---|
| Buried-Channel CCDs with High Charge Transfer Efficiency and Large Charge Capacity for Low-Temperature Readout of Long-Wavelength Infrared Detectors | A. L. Lattes<br>B-Y. Tsaur   | <i>Proc. SPIE</i> <b>1684</b> , 212 (1992)  |
| High-Power, Continuous-Wave, Nd:YAG Microchip Laser Array  | C. D. Nabors<br>A. Sanchez<br>A. Mooradian   | <i>Opt. Lett.</i> <b>17</b> , 1587 (1992)   |
| Measurements and Modeling of Linear and Nonlinear Effects in Striplines  | D. E. Oates<br>P. P. Nguyen*<br>G. Dresselhaus*<br>M. S. Dresselhaus*<br>C. W. Lam*<br>S. M. Ali*                      | <i>J. Superconduct.</i> <b>5</b> , 361 (1992)   |
| Photolithography at 193 nm   | M. Rothschild<br>R. B. Goodman<br>M. A. Hartney<br>M. W. Horn<br>R. R. Kunz<br>J. H. C. Sedlacek<br>D. C. Shaver       | <i>J. Vac. Sci. Technol. B</i><br><b>10</b> , 2989 (1992)                               |
| Superconductive Circuits for Sampled-Data Signal Processing at Bandwidths beyond 10 GHz  | J. P. Sage<br>J. B. Green<br>K. Tam  | <i>1992 Government Microcircuit Applications Conf. Dig. of Papers</i> , Vol. 18, p. 491 |
| Multiquantum-Well Detection of Nanosecond Far-Infrared Superradiant Pulses at Temperatures above 77 K  | J. Waldman*<br>D. B. Moix*<br>D. P. Scherrer*<br>F. K. Kneubühl*<br>W. D. Goodhue<br>E. R. Mueller*<br>M. J. Coulombe* | <i>Infrared Phys.</i> <b>33</b> , 487 (1992)  |

---

\*Author not at Lincoln Laboratory.



# ACCEPTED FOR PUBLICATION

Measurements of Optical-Heterodyne Conversion in Low-Temperature-Grown GaAs	E. R. Brown K. A. McIntosh F. W. Smith M. J. Manfra C. L. Dennis	<i>Appl. Phys. Lett.</i>
Enhanced Negative Differential Resistance in a Resonant Tunneling Structure	E. R. Brown C. D. Parker A. R. Calawa M. J. Manfra	<i>Appl. Phys. Lett.</i>
Genosensors: Microfabricated Devices for Automated DNA Sequence Analysis	M. D. Eggers* M. E. Hogan* R. K. Reich J. B. Lamture* K. L. Beattie* M. A. Hollis D. J. Ehrlich B. B. Kosicki J. M. Shumaker* R. S. Varma* R. A. Murphy D. D. Rathman	<i>Proc. SPIE</i>
Heat Generation in Nd:YAG and Yb:YAG	T. Y. Fan	<i>IEEE J. Quantum Electron.</i>
Diode-Pumped, Q-Switched Yb:YAG Laser	T. Y. Fan S. Klunk* G. Henein*	<i>Opt. Lett.</i>
Physics of Lasers	P. L. Kelley J. J. Zayhowski	In <i>Encyclopedia of Applied Physics</i> (VCH Publishers, New York)
The Role of Hydrogen in Excimer Laser Induced Damage of Fused Silica	D. H. Levy* K. K. Gleason* M. Rothschild J. H. C. Sedlacek	<i>J. Appl. Phys.</i>

---

\*Author not at Lincoln Laboratory.

A Nonlinear Transmission Line  
Model for Superconducting Stripline  
Resonators

J. H. Oates\*  
R. T. Shin\*  
D. E. Oates  
M. J. Tsuk\*  
P. P. Nguyen\*

*IEEE Trans. Appl.  
Superconduct.*

Optical Materials for Excimer Laser  
Applications

M. Rothschild

*Opt. Photon. News*

Excimer Laser Induced Degradation  
in Bulk Fused Silica

M. Rothschild  
J. H. C. Sedlacek

*Proc. SPIE*

Studies of Carrier Heating in  
InGaAs/AlGaAs Strained-Layer  
Quantum-Well Diode Lasers Using  
a Multiple Wavelength Pump Probe  
Technique

C. K. Sun\*  
H. K. Choi  
C. A. Wang  
F. G. Fujimoto\*

*Appl. Phys. Lett.*

#### PRESENTATIONS<sup>†</sup>

Modeling of the Vapor Etching of GaAs  
by CH<sub>3</sub>I

C. W. Krueger  
M. Flytzani-  
Stephanopoulos\*  
R. A. Brown\*  
C. A. Wang

American Institute of Chemical  
Engineers,  
Miami Beach, Florida,  
1–6 November 1992

Silane and Siloxane Polymers for  
ArF Bilayer Resist Applications

R. R. Kunz

IEEE Lithography Workshop,  
Albuquerque, New Mexico,  
3–6 November 1992

Pattern Transfer of Surface-Imaged Resists  
Using a Helical Resonator Reactor

M. W. Horn  
M. A. Hartney  
R. R. Kunz  
B. Chapman\*  
R. Vanos\*  
I. DelaRoosa\*

39th National Symposium of the  
American Vacuum Society,  
Chicago, Illinois,  
9–13 November 1992

---

\*Author not at Lincoln Laboratory.

†Titles of presentations are listed for information only. No copies are available for distribution.

Optical Materials for Excimer Lasers	J. H. C. Sedlacek M. Rothschild	SPIE's OE/Technology '92, Boston, Massachusetts, 15-20 November 1992
Measurements of Optical Damage in LiNbO <sub>3</sub> Waveguides at 1320 nm	G. E. Betts F. J. O'Donnell K. G. Ray	IEEE Lasers and Electro-Optics Society Annual Meeting, Boston, Massachusetts, 16-19 November 1992
Mid-Infrared Diode Lasers	S. J. Eglash H. K. Choi	
Large-Numerical-Aperture Microlenses by One-Step Ion-Beam Etching and Mass-Transport Smoothing	Z. L. Liao D. E. Mull C. L. Dennis R. G. Waarts*	
Coherent Coupling of Microchip Arrays	C. D. Nabors	
High-Power Nd:YAG Microchip Laser Array	C. D. Nabors A. Sanchez A. Mooradian	
Free-Space Optical Interconnections for Digital Systems	D. Z. Tsang	
High Power Tapered Semiconductor Amplifiers and Oscillators at 980 nm	J. N. Walpole E. S. Kintzer J. C. Livas C. A. Wang S. R. Chinn L. J. Missaggia	Fall Optical Society of America OPTCON '92 Meeting, Boston, Massachusetts, 17-19 November 1992
Eyesafe Diode Lasers from 1.5 to 5 $\mu$ m	S. J. Eglash H. K. Choi	
193-Nanometer Lithography and Beyond	M. Rothschild	
Quantum Well Nonlinearities	H. Q. Le	Technical Seminar, University of Virginia, Charlottesville, Virginia, 20 November 1992

---

\*Author not at Lincoln Laboratory.

Resonant-Tunneling-Diode Circuits	T. C. L. G. Sollner E. R. Brown R. A. Calawa C. L. Chen C. G. Fonstad* W. D. Goodhue R. H. Mathews J. P. Sage F. W. Smith	Advanced Heterostructure Transistors Conference, Kona, Hawaii, 29 November–4 December 1992
Effects of Substrate Bombardment During Sputter-Deposition of YBaCuO	A. C. Anderson	1992 Fall Meeting of the Materials Research Society, Boston, Massachusetts, 30 November–4 December 1992
Near-Future Applications of Laser Microchemical Processing	D. J. Ehrlich	
Surface Resistance and Phase Noise of YBCO Microstrip Linear Resonators	J. D. Goettee* P. M. Mankiewich* E. I. DeObaldia* W. J. Skocpol* M. L. O'Malley* D. E. Oates A. C. Anderson	
Device Applications of Low- Temperature-Grown GaAs	F. W. Smith	
Recent Advances in Diode Lasers and Diode-Pumped Solid State Lasers	I. Melngailis	
III-V MQW Structures for Detection of Normal-Incidence Radiation without Gratings and Laser-Heterodyne Detection with Ultrawide Bandwidths	E. R. Brown	Laser '92 Conference, Houston, Texas, 9 December 1992  DARPA Infrared Focal Plane Reviews, McLean, Virginia, 10 December 1992

---

\*Author not at Lincoln Laboratory.



Surface Imaging Resists for 193-nm Lithography	D. W. Johnson* M. A. Hartney	8th Meeting of Optical Engineering, Tel Aviv, Israel, 14 December 1992
Multiple-Quantum-Well Detectors for Pulsed Submillimeter Radiation	J. Waldman* E. Mueller* M. Coulombe* W. D. Goodhue D. Moix* D. Scherrer* F. Kneubühl*	17th International Conference on Infrared and Millimeter Waves, Pasadena, California, 14–18 December 1992
Diode-Pumped Ytterbium Lasers	T. Y. Fan	Winter Colloquium on Quantum Electronics, Snowbird, Utah, 7 January 1993
Single-Spatial-Mode Tapered Amplifiers and Oscillators	J. N. Walpole E. S. Kintzer S. R. Chinn C. A. Wang L. J. Missaggia	SPIE's OE/LASE '93, Los Angeles, California, 16–23 January 1993
Improvements in Passive, Low-Noise-Figure Optical Links	G. E. Betts F. J. O'Donnell	3rd Annual DARPA Symposium on Photonics Systems for Antenna Applications, Monterey, California, 20–22 January 1993
A Resonant-Tunneling Transmission-Line Relaxation Oscillator for Picosecond-Pulse and Terahertz Continuous-Wave Applications	E. R. Brown	Ultrafast Electronics Symposium, San Francisco, California, 25 January 1993

---

\*Author not at Lincoln Laboratory.

## ORGANIZATION

### SOLID STATE DIVISION

A. L. McWhorter, *Head*  
I. Melngailis, *Associate Head*  
E. Stern, *Associate Head*  
D. C. Shaver, *Assistant Head*  
J. F. Goodwin, *Assistant*  
  
D. J. Ehrlich, *Senior Staff*  
N. L. DeMeo, Jr., *Associate Staff*  
J. W. Caunt, *Assistant Staff*  
K. J. Challberg, *Administrative Staff*

### SUBMICROMETER TECHNOLOGY

M. Rothschild, *Leader*  
T. M. Lyszczarz, *Assistant Leader*

Astolfi, D. K.	Hartney, M. A.
Craig, D. M.	Horn, M. W.
Dennis, C. L.	Keast, C. L.
DiNatale, W. F.	Kunz, R. R.
Doran, S. P.	Maki, P. A.
Efremow, N. N., Jr.	Melngailis, J. <sup>†</sup>
Forte, A. R.	Sedlacek, J. H. C.
Geis, M. W.	Twichell, J. C.
Goodman, R. B.	Uttaro, R. S.

### QUANTUM ELECTRONICS

A. Sanchez-Rubio, *Leader*  
T. Y. Fan, *Assistant Leader*

Aggarwal, R. L.	Hsu, L.*
Cook, C. C.	Jeys, T. H.
Daneu, V.	Kelley, P. L. <sup>‡</sup>
DeFeo, W. E.	Le, H. Q.
DiCecca, S.	Nabors, C. D.
Dill, C. D., III	Ochoa, J. R.
Hancock, R. C.	Sullivan, D. J.
Hotaling, T. C.	Zayhowski, J. J.

### ELECTRONIC MATERIALS

B-Y. Tsaur, *Leader*  
D. L. Spears, *Assistant Leader*

Anderson, C. H., Jr.	Krohn, L., Jr.
Button, M. J.	Marino, S. A.
Chen, C. K.	Mastromattei, E. L.
Choi, H. K.	McGilvary, W. L.
Connors, M. K.	Nitishin, P. M.
Eglash, S. J.	Pantano, J. V.
Fahey, R. E.	Reinold, J. H., Jr.
Finn, M. C.	Turner, G. W.
Harman, T. C.	Wang, C. A.
Iseler, G. W.	

### HIGH SPEED ELECTRONICS

R. A. Murphy, *Leader*  
M. A. Hollis, *Assistant Leader*

Bozler, C. O.	Mathews, R. H.
Brown, E. R.	Mattia, J. P.*
Chen, C. L.	McIntosh, K. A.
Clifton, B. J. <sup>‡</sup>	Nichols, K. B.
Crenshaw, D. L.*	Parker, C. D.
Goodhue, W. D.	Rabe, S.
Harris, C. T.	Rathman, D. D.
Lincoln, G. A., Jr.	Smith, F. W.
Mahoney, L. J.	Vera, A.
Manfra, M. J.	

---

\* Research Assistant

† Part Time

‡ Leave of Absence

## ELECTROOPTICAL DEVICES

R. C. Williamson, *Leader*  
L. M. Johnson, *Assistant Leader*

Aull, B. F.  
Bailey, R. J.  
Betts, G. E.  
Donnelly, J. P.  
Ferrante, G. A.  
Golubovic, B.\*  
Groves, S. H.  
Hovey, D. L.  
Liau, Z. L.  
Lind, T. A.

Missaggia, L. J.  
Mull, D. E.  
O'Donnell, F. J.  
Palmacci, S. T.  
Palmateer, S. C.  
Reeder, R. E.  
Roussell, H. V.  
Tsang, D. Z.  
Walpole, J. N.  
Woodhouse, J. D.

## ANALOG DEVICE TECHNOLOGY

R. W. Ralston, *Leader*  
T. C. L. G. Sollner, *Assistant Leader*  
A. C. Anderson, *Senior Staff*  
A. M. Chiang, *Senior Staff*

Arsenault, D. R.  
Boisvert, R. R.  
Brogan, W. T.  
Curd, D. R.\*  
Delin, K. A.  
Denneno, J. M.  
Fitch, G. L.  
Green, J. B.†  
Holtham, J. H.  
LaFranchise, J. R.

Lyons, W. G.  
Macedo, E. M., Jr.  
Mankiewich, P. M.  
Oates, D. E.  
Sage, J. P.  
Seaver, M. M.  
Slattery, R. L.  
Whitley, D. B.  
Yu-Jahnes, L. S.\*

## MICROELECTRONICS

E. D. Savoye, *Leader*  
B. B. Kosicki, *Assistant Leader*  
B. E. Burke, *Senior Staff*

Clark, H. R., Jr.  
Daniels, P. J.  
Doherty, C. L., Jr.  
Dolat, V. S.  
Donahue, T. C.

Felton, B. J.  
Gregory, J. A.  
Johnson, K. F.  
Loomis, A. H.  
McGonagle, W. H.

Mountain, R. W.  
Percival, K. A.  
Pichler, H. H.  
Reich, R. K.  
Young, D. J.

---

\* Research Assistant

† Leave of Absence

# 1. ELECTROOPTICAL DEVICES

## 1.1 FABRICATION OF ANAMORPHIC MICROLENSES AND COLLIMATION OF TAPERED-LASER OUTPUT

Precision anamorphic microlenses with large numerical aperture are needed for collimating the astigmatic output of gain-guided and/or unstable-resonator lasers, including ones with laterally tapered gain regions. Such lenses offer a means to realize simple and compact optical systems exploiting the demonstrated high-power capability of tapered devices [1],[2]. In this report we describe the fabrication of the first anamorphic microlens by mass transport and the collimation, using this lens, of the output of a tapered unstable-resonator laser into a nearly round, narrow beam.

As illustrated in Figure 1-1, the lens has been designed by considering the two distinct wavefront curvatures in the tapered-laser output. Because of propagation in the tapered active region (typically 2 mm in length) and refraction at the output facet, the output light in the junction plane appears as if it originated from a virtual source  $\sim 600 \mu\text{m}$  inside the active region. The exiting light also undergoes a large diffraction perpendicular to the junction plane, owing to the tight heterostructure optical confinement in the active region. The optical path lengths of the rays and the lens profile required for their collimation have been accurately formulated in analytical expressions. It is worth noting that, because of the two distinct curvatures, the lens surface approximates a small portion of a torus.

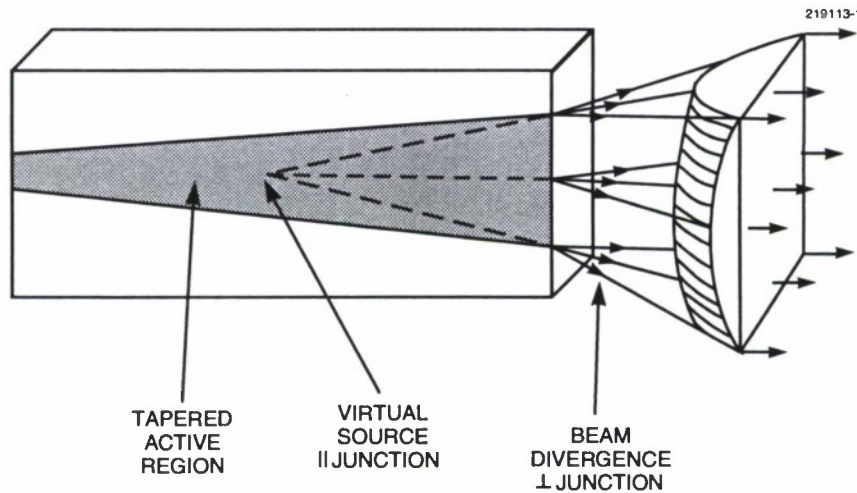
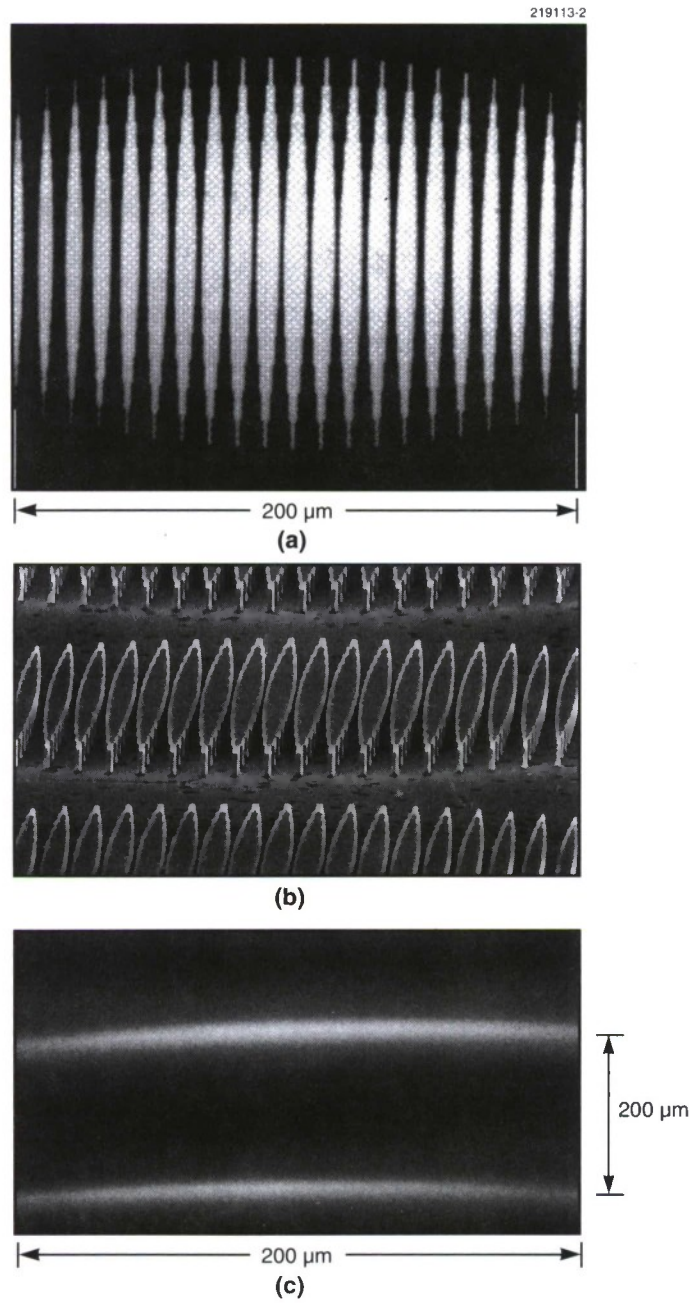


Figure 1-1. Collimation of astigmatic output from a tapered laser using the anamorphic microlens.





*Figure 1-2. Stages in formation of the microlens: (a) lithographic mask, (b) etched mesa pattern, and (c) lens formed after mass transport. Part (a) is an ordinary optical micrograph, and parts (b) and (c) are perspective views obtained by using a scanning electron microscope.*

The microlenses have been formed in a GaP substrate by ion-beam-assisted etching, followed by mass-transport smoothing [3]. To etch the lens preform, a photolithographic mask was first made by electron-beam exposure. The mask consists of a set of spindle-shaped patterns as shown in Figure 1-2(a). The spindles are on 10- $\mu\text{m}$  centers and have a width variation directly proportional to the desired lens height variation. Thus, the mesa formed after ion-beam-assisted etching, as illustrated in Figure 1-2(b), has the same average mass distribution as the desired lens profile. The lens is then formed, as shown in Figure 1-2(c), after coalescence and smoothing, i.e., mass transport, of these mesas by heat treatment at 900°C for 21 h and 1070°C for 238 h.

Figure 1-3 shows stylus surface profiles of a fabricated anamorphic microlens. The distinct curvatures in the two directions, as designed, can clearly be seen. The focal lengths in the fast and slow directions are 165 and 770  $\mu\text{m}$ , respectively. The profiles have been compared with ideal ones and show close agreement. It should be noted, however, that lenses with distorted profiles were also observed, and more work is needed for optimized mass-transport parameters.

The anamorphic microlenses have been tested for collimating the output from a tapered unstable-resonator laser [2]. For this purpose, the tapered device was cleaved to a 2-mm length for a close match with the anamorphic lens focal lengths. (By Snell's law, the distance between the virtual source and the output facet is equal to the device length divided by the effective refractive index. That distance plus the focal length in the fast direction must equal the focal length in the slow direction, as can be seen in

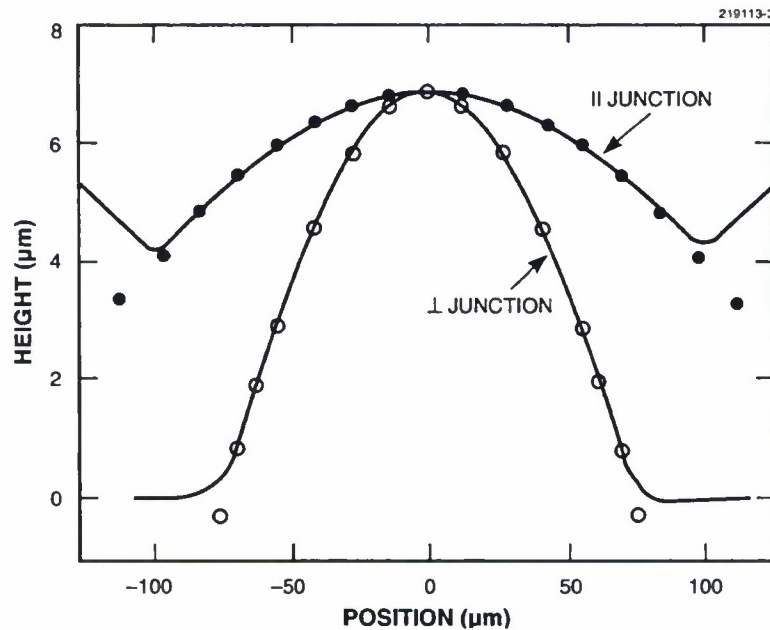


Figure 1-3. Stylus surface profiles of an anamorphic microlens along the two major directions (curves) compared with the ideal profiles from calculations (points).

Figure 1-1.) To avoid potential complications due to possible external reflections, the output facet was not coated for reduced reflectivity, as is usually done for optimized external efficiency. Also, the device was moderately operated at 1 A with an output of 95 mW, to avoid the more complicated spatial mode behavior that could set in at higher-power operation [2]. For the 0.98- $\mu\text{m}$  wavelength, the anamorphic lens wafer was antireflection coated with evaporated SiO on both sides. The lens wafer was mounted on a micromanipulator [4] capable of both translational and angular positioning. The lens was first aligned to the laser for the tightest, oval beam spot on a monitor screen. The far field was then more accurately measured by scanning an optical fiber (receiver) of a 20- $\mu\text{m}$  core diameter placed at a distance of 40 cm from the anamorphic lens.

Figure 1-4 shows measured far-field scans parallel and perpendicular to the junction plane, with beam divergences of 0.32 and 0.43°, respectively. These are very close to the 0.30 and 0.40° divergences expected from  $\lambda/D$  for the effective apertures  $D$  of the lens of  $\sim 190$  and 140  $\mu\text{m}$  (cf. Figure 1-3), respectively. This near diffraction-limited performance is consistent with the accurate lens profiles (Figure 1-3). However, the numerical apertures of the present lenses are not sufficient to completely collect the laser output. (The output end of the tapered region is 200  $\mu\text{m}$  in width, and the beam divergences parallel and perpendicular to the junction plane are 21 and 35°, respectively, with the latter being full width at half-maximum of an approximately Gaussian beam profile.) When a large-area detector is placed at a close distance to collect all the light, there is nonetheless no difference in measured powers with or without the lens wafer. This indicates negligible reflection and transmission losses through the lens wafer.

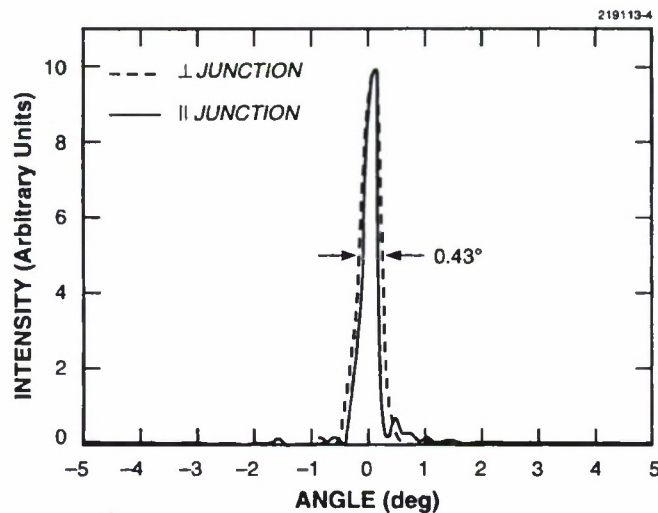


Figure 1-4. Far-field pattern of a narrow, nearly round beam obtained in collimation of tapered-laser output using the anamorphic microlens.

Instead of collimation, the anamorphic lens can also be designed to focus the astigmatic beam to a round spot comparable to the core of a single-mode fiber (typically 10  $\mu\text{m}$  in diameter) and thus facilitate a direct coupling of the laser output into fiber. Such a system is potentially very simple and compact compared to that employing bulk optics.

In conclusion, the first large-numerical-aperture anamorphic microlenses have been demonstrated with accurate profiles. A near diffraction-limited narrow beam has been obtained in the collimation of the astigmatic output from an unstable-resonator laser with a tapered active region. These microlenses are very promising for simplified optics for the coupling of high-power lasers to optical fibers.

Z. L. Liao            L. J. Missaggia  
J. N. Walpole       C. L. Dennis  
D. E. Mull

## **1.2 SEMICONDUCTOR FILTERS WITH WIDE ACCEPTANCE ANGLE AND NARROW BANDWIDTH**

Dielectric optical filters are widely used in fiber and free-space optical communications systems for background noise reduction and channel selection. Such filters require low insertion loss and optical bandwidths of a nanometer or less, to match the narrow linewidths and the close channel spacing possible with laser sources. An additional requirement for free-space satellite communications is a large filter area and wide field of view, i.e., low sensitivity to input angle. Commercially available filters are usually fabricated from materials of low refractive index, typically oxides or fluorides with  $n < 2.5$ , which limit their performance. Use of high-index III-V semiconductor materials improves filter performance and allows for on-chip integration with other III-V devices. Gas-source molecular beam epitaxy (GSMBE) has been used to fabricate narrowband filters in a GaAs/AlAs multilayer structure on a GaAs substrate for applications at 980 and 1550 nm. We project that these filters will provide a wide field of view.

Narrow optical bandwidths can be realized with quarter-wave-shifted, multilayer thin-film filters. Spectrally, these filters have a narrow transmission resonance centered within a wide, flat stopband. Such filters are realized using multilayer structures of two alternating materials with different refractive indices and thicknesses. Each layer thickness must be one-quarter of the desired center resonance wavelength. To produce the central passband, the grating period, i.e., the sum of the different layer thicknesses, is interrupted at the center of the filter to produce a quarter-wave shift.

From Snell's law the field of view of multilayer filters, for a given optical bandwidth, increases as the material refractive index is increased. High refractive indices ( $3 < n < 4$ ) can be obtained by using semiconductors such as silicon or III-V compound semiconductors. The higher refractive index of the semiconductor material compared to commercial filter materials allows for a larger angular field of view for a given bandwidth. Compared to commercial thin-film dielectric filters, semiconductor filters also have excellent single-crystal optical properties with little residual material absorption or scattering loss.



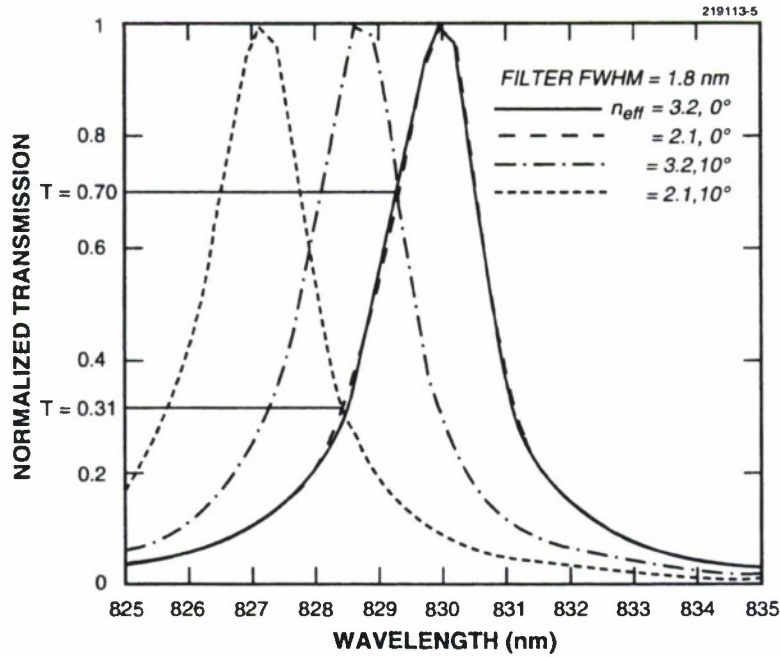


Figure 1-5. Calculated filter transmission for collimated light with input angles of 0 and 10°, for filters with effective indices of 2.1 and 3.2.

We have calculated the theoretical transmission characteristics for multilayer structures numerically using the matrix method [5]. Figure 1-5 shows the normalized filter transmission calculated for collimated light with input angles of 0 and 10° and for effective indices  $n_{\text{eff}} = 2.1$  and 3.2. The filter full width at half-maximum (FWHM) is held constant at 1.8 nm. The minimum transmission across the band for a single-frequency source for the  $n_{\text{eff}} = 3.2$  case is 70%, while that for the  $n_{\text{eff}} = 2.1$  case is 31%. The filters with higher effective index also have less transmission variation over the full range of angles compared to those with lower effective index. For narrower filter bandwidths, both cases would have reduced minimum transmission values, but the higher effective index degrades more slowly with angle than the lower effective index. For free-space communication, there will be trade-offs regarding filter bandwidth and minimum transmission, depending on system requirements.

Precision semiconductor growth techniques, such as GSMBE, allow fabrication of filters with extremely narrow central passbands (< 1 nm) and high transmission. The GSMBE process is ideally suited for the growth of large-area filters because of its excellent lateral uniformity. Also inherent to GSMBE is precise control of growth rate and alloy composition by using in-situ reflection high-energy electron diffraction measurements, which ensures long-term stability and reproducibility of the filter center frequency. We have fabricated filters with 0.6-nm FWHM and 90% peak-transmission resonance passbands at 980-nm wavelengths, in agreement with the theoretical prediction [5]. The filter structure, which consists of 61 layers of alternating AlAs and GaAs, is shown in Figure 1-6(a). The measured filter transmission of the central passband, obtained using a tunable Ti:sapphire CW laser source, is shown in

Figure 1-6(b). The filter central wavelength was within 1% of the design wavelength. A wider spectral scan measured with a spectrometer is shown in Figure 1-7, indicating a blocking band ~ 1200 nm wide. In this measurement, the transmission passband peak is limited by the wavelength resolution of the instrument. The spot diameter was ~ 4 mm for this measurement.

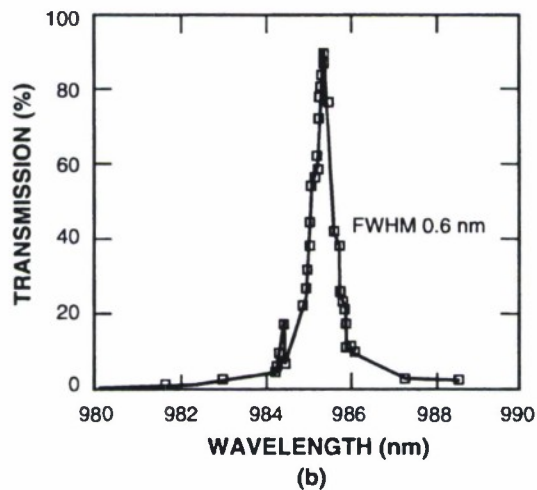
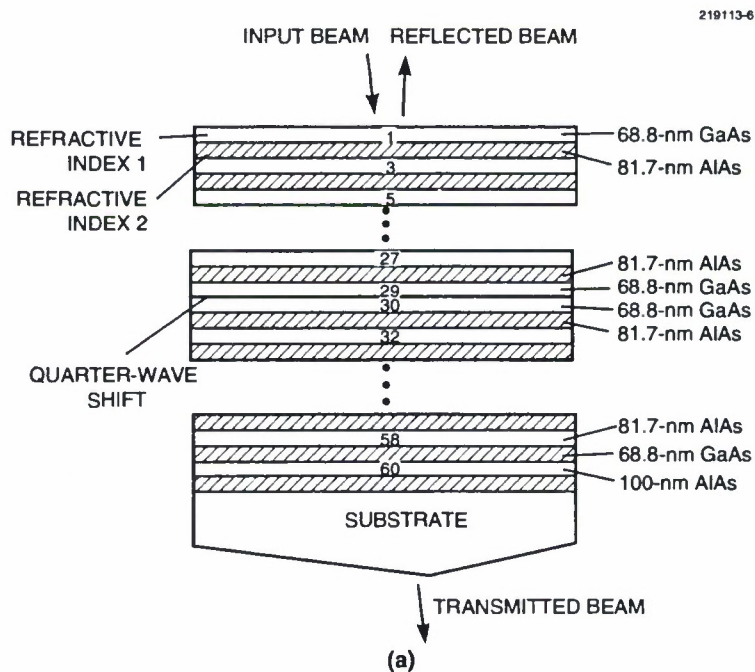


Figure 1-6. (a) Schematic of the layer structure for the quarter-wave-shifted multilayer dielectric thin-film filter at 980-nm wavelength. (b) Measured central transmission passband for the 61-layer GaAs/AlAs filter structure. The measurement spot size is < 1 mm in diameter, and the input cone angle ~ 2°.

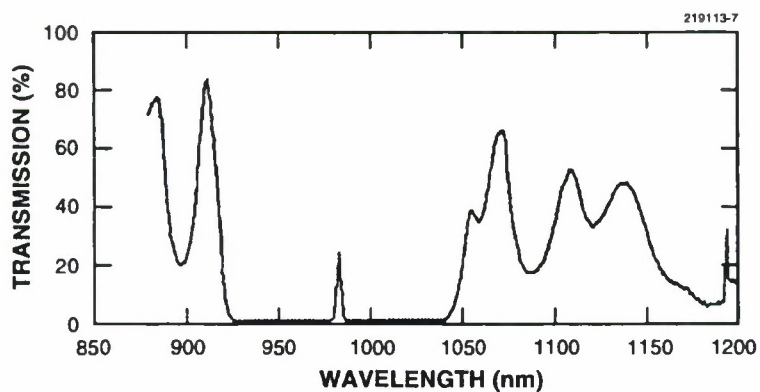


Figure 1-7. Filter transmission spectrum for the 61-layer GaAs/AlAs filter structure. The filter was mounted on a glass substrate and the GaAs substrate removed. The measurement spot size was  $\sim 4$  mm in diameter. The central transmission band peak is limited by the instrument resolution of  $> 1$  nm.

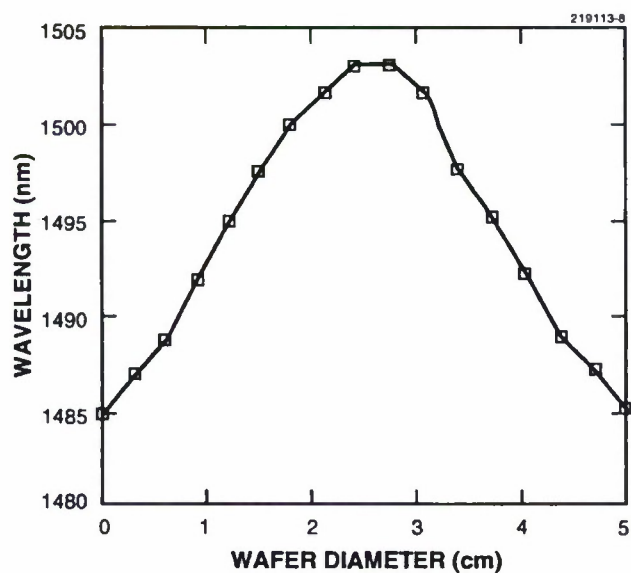


Figure 1-8. Filter central wavelength uniformity of 5-cm-diam wafer. The thickness uniformity is 1.2% from edge to edge.

At 1500-nm wavelengths, we have achieved filters with 0.9-nm FWHM measured by reflectivity. The filter structure consists of 61 layers of AlAs and GaAs whose thicknesses are 131 and 110 nm, respectively. The transmission spectra of these filters have not been measured. The filter central wavelength uniformity is shown in Figure 1-8 for a 5-cm-diam wafer. These results indicate the excellent material quality and uniformity we can achieve. Previous data [6] near this wavelength exhibited a 1.2-nm FWHM, and 40% transmission for the transmission resonance peak centered around 1600 nm. The author claimed that these results were limited by layer uniformity and free-carrier absorption losses.

In conclusion, large-area high-uniformity multilayer optical filters have been fabricated by GSMBE. Optical bandwidths as narrow as 0.6 nm have been achieved. The high refractive index of the GaAs/AlAs layers should provide a wide field of view.

S. C. Palmateer  
K. Rauschenbach  
P. A. Maki

#### REFERENCES

1. J. N. Walpole, E. S. Kintzer, S. R. Chinn, C. A. Wang, and L. J. Missaggia, *Appl. Phys. Lett.* **61**, 740 (1992).
2. J. N. Walpole, E. S. Kintzer, S. R. Chinn, C. A. Wang, and L. J. Missaggia, *Conf. Lasers Electro-Optics Tech. Dig.* (Optical Society of America, Washington, D.C., 1992), Paper CWN1.
3. Solid State Research Report, Lincoln Laboratory, MIT, 1992:2, p. 3.
4. J. W. Caunt and V. Diadiuk, *Appl. Opt.* **29**, 2311 (1990).
5. H. A. Macleod, *Thin-Film Optical Filters*, 2nd ed. (Adam Hilger, Bristol, England, 1986).
6. P. C. Kemeny, *J. Appl. Phys.* **64**, 610 (1988).



## 2. QUANTUM ELECTRONICS

### 2.1 CALCULATED ROOM-TEMPERATURE THRESHOLD CURRENT DENSITIES FOR VISIBLE II-VI ZnCdSe/ZnSe QUANTUM-WELL DIODE LASERS

Blue-green lasing from the wide-bandgap II-VI ZnCdSe/ZnSe semiconductor quantum-well diode lasers was first reported in the pulsed mode (500-ns pulses at 2000 Hz) at 77 K by Haase et al. [1]. More recently, CW operation at 77 K has been reported by Jeon et al. [2], Yu et al. [3], and Sony Corp. [4]. Jeon et al. [2] also obtained pulsed operation at temperatures between 77 K and room temperature. To date, CW room-temperature operation has not been possible because of thermal problems resulting from large turn-on voltages and high threshold current densities ( $\sim 1600 \text{ A/cm}^2$  in Ref. 2). Here we show that by tailoring the epitaxial structure for optimum optical confinement the calculated threshold current densities can be reduced to acceptable levels ( $\sim 400 \text{ A/cm}^2$ ) for CW operation; we do not consider the problem of large turn-on voltages.

The room-temperature threshold current densities of  $\text{Zn}_{0.83}\text{Cd}_{0.17}\text{Se/ZnSe}$  (henceforth ZnCdSe/ZnSe) quantum-well lasers have been calculated using the simple model of Dutta [5] for the quantum-well gain and spontaneous radiative recombination rate. This model neglects the effects of strain, band nonparabolicity, intraband scattering, and excitonic and nonradiative recombination; the details of the calculations are reported elsewhere [6]. The calculated results for the ZnCdSe/ZnSe quantum-well lasers are compared with similar results for the well-developed infrared III-V GaAs/Ga<sub>0.5</sub>Al<sub>0.5</sub>As (henceforth GaAs/GaAlAs) quantum-well lasers in order to gain insight into the basic similarities and differences between these two diode laser systems.

The room-temperature values of the material and device parameters used in the calculations for the GaAs/GaAlAs and ZnCdSe/ZnSe quantum-well lasers are given in Table 2-1. The symbols  $m_e$ ,  $m_{lh}$ , and  $m_{hh}$  are the electron, light-hole, and heavy-hole masses, respectively,  $E_g$  is the energy gap,  $\Delta$  is the spin-orbit splitting energy of the valence band,  $\delta V_c$  and  $\delta V_v$  are the conduction and valence band offsets of the quantum-well material relative to the barrier material,  $\mu_w$  and  $\mu_b$  are the refractive indices of the well and barrier material at the lasing wavelength,  $\alpha_a$  is the average absorption coefficient of the well and barrier layers, and  $L$  is the laser cavity length. We note that the values of the electron, light-hole, and heavy-hole masses for ZnCdSe are more than a factor of 2 larger than those for GaAs.

Schematic diagrams for the refractive index profile of a single quantum well (SQW), a multiple quantum well (MQW), and a step-index separate-confinement heterostructure (STINSCH) are presented in Figures 2-1(a), 2-1(b), and 2-1(c), respectively. Calculated values of maximum quantum-well gain  $g_{\max}$  for the ZnCdSe/ZnSe and GaAs/GaAlAs SQW structure shown in Figure 2-1(a), with well layer thickness  $L_w = 10 \text{ nm}$ , are plotted as a function of the injected carrier density  $n_{\text{inj}}$  and nominal current density  $J_{\text{nom}}$  in Figures 2-2(a) and 2-2(b), respectively. Our results for  $g_{\max}$  vs  $n_{\text{inj}}$  are fairly consistent with those calculated by Ahn et al. [7] using a multiband effective mass theory and the density matrix formalism with intraband scattering taken into account. The injected carrier densities (the nominal current densities) required to achieve the same gain are approximately a factor of 3 larger for the ZnCdSe quantum wells than for the GaAs quantum wells. This is due to larger values of  $m_e$ ,  $m_{lh}$ , and  $m_{hh}$  for the ZnCdSe system.

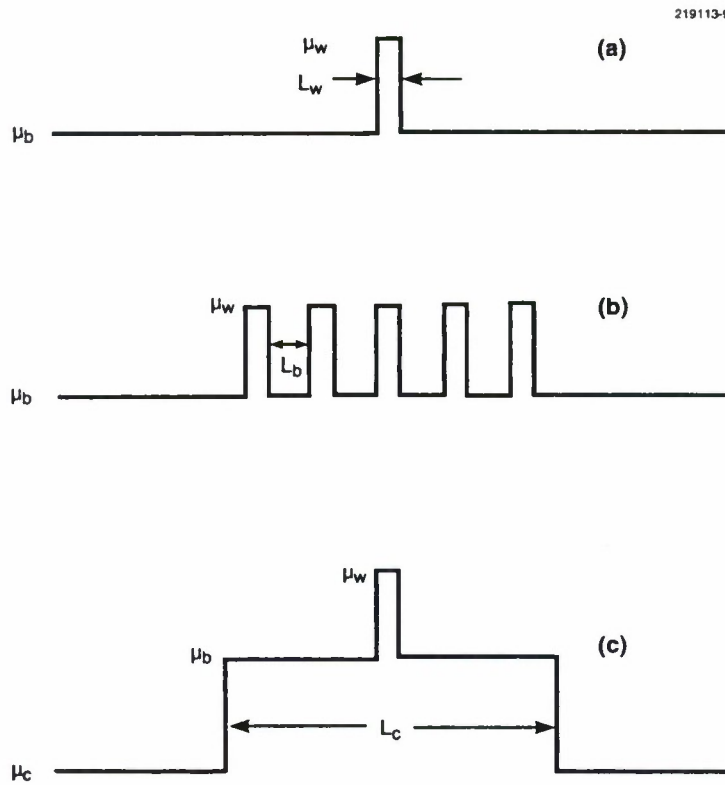
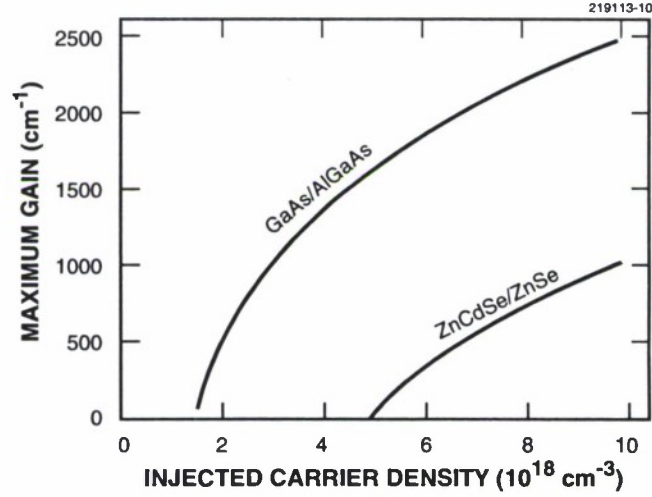
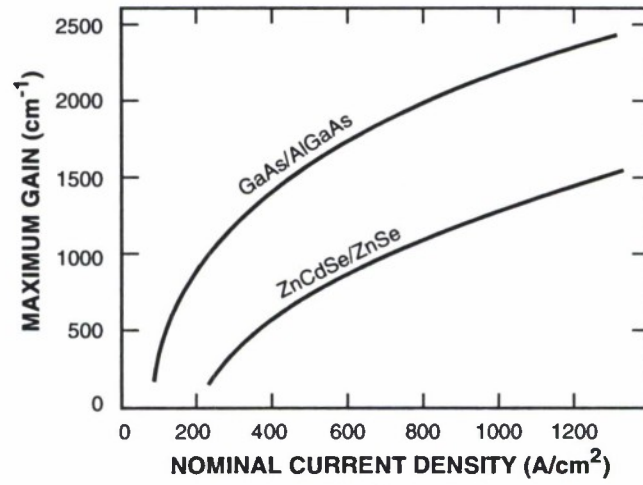


Figure 2-1. Schematic diagrams for the refractive index profile of (a) a single quantum well, (b) a multiple quantum well (MQW), and (c) a step-index separate-confinement heterostructure (STINSCH).



(a)



(b)

Figure 2-2. (a) Calculated maximum room-temperature gain coefficient  $g_{\max}$  vs injected carrier density  $n_{\text{inj}}$  for 10-nm-thick ZnCdSe/ZnSe and GaAs/GaAlAs single quantum wells, and (b)  $g_{\max}$  vs nominal current density  $J_{\text{nom}}$  for the same structures as in (a).

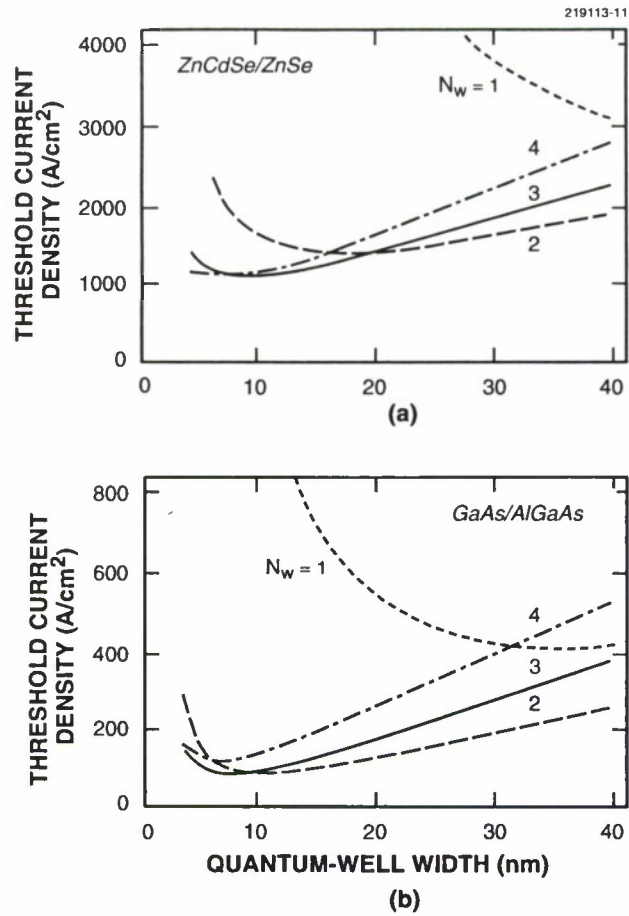


Figure 2-3. Calculated room-temperature threshold current densities  $J_{th}$  vs quantum-well width  $L_w$  for MQWs with barrier layer thickness  $L_b$  of 10 nm. The structures in (a) and (b) are ZnCdSe/ZnSe and GaAs/GaAlAs, respectively.

TABLE 2-1

Room-Temperature Values of the Material and Device Parameters for the GaAs/GaAlAs and ZnCdSe/ZnSe Quantum-Well Lasers\*

Parameter	GaAs/GaAlAs	ZnCdSe/ZnSe
$m_e/m_0$	0.071	0.16
$m_{tr}/m_0$	0.081	0.57
$m_{hh}/m_0$	0.45	1.0
$E_g$ (eV)	1.42	2.40
$\Delta$ (eV)	0.34	0.43
$\delta V_c$ (eV)	0.42	0.18
$\delta V_v$ (eV)	0.21	0.08
$\mu_w$	3.59	2.8
$\mu_b$	3.26	2.7
$\alpha_a$ (cm <sup>-1</sup> )	3.5	3.5
$L$ (mm)	1.0	1.0
*From Ref. 6.		

The threshold gain coefficient  $g_{th}$  is obtained by dividing the round-trip cavity loss coefficient by the confinement factor. If nonradiative recombination is neglected,  $J_{th}$  is obtained from  $J_n$  by setting  $g_{max}$  equal to  $g_{th}$ . The resulting  $J_{th}$  values for the ZnCdSe/ZnSe and GaAs/GaAlAs MQW structure illustrated in Figure 2-1(b) are shown as a function of quantum-well width in Figures 2-3(a) and 2-3(b), respectively. In each case we used barrier layer thickness  $L_b = 10$  nm. In both systems the lowest values of  $J_{th}$  occur for  $L_w \approx 10$  nm and number of wells  $N_w = 3$  or 4. At this point,  $J_{th}$  is  $\sim 1100/\text{cm}^2$  for the ZnCdSe/ZnSe MQWs and  $\sim 240 \text{ A/cm}^2$  for the GaAs/GaAlAs MQWs.

The calculated values of  $J_{th}$  for ZnCdSe/ZnSe MQWs with  $N_w = 6$ ,  $L_w = 6$  nm, and  $L_b = 10$  nm are compared in Figure 2-4 with the pulsed data of Jeon et al. [2] at  $T = 200, 250$ , and  $273$  K. The relatively good agreement between the observed and calculated values of  $J_{th}$  provides some support for the theoretical model used here, even though exciton effects have been neglected.

Further reduction in  $J_{th}$  can be achieved using a SQW in a STINSCH structure, shown in Figure 2-1(c). (As a result of the transparency condition, the threshold current is minimized by using only one quantum well in the STINSCH.) The calculated values of  $J_{th}$  for an optimized STINSCH structure are plotted in Figure 2-5 against the refractive index step  $\Delta\mu = \mu_c - \mu_b$  for the ZnCdSe/ZnSe and



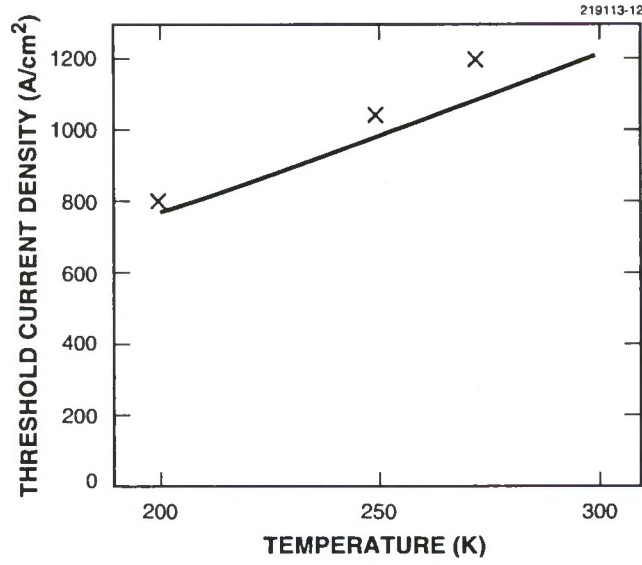


Figure 2-4. Comparison of the calculated values (solid curve) of the threshold current density  $J_{th}$  for ZnCdSe/ZnSe MQWs ( $N_w = 6$ ,  $L_w = 6$  nm, and  $L_b = 10$  nm) with the experimental data of Jeon et al. [2] (points) at  $T = 200$ , 250, and 273 K. The values of the band parameters were assumed to be temperature independent.

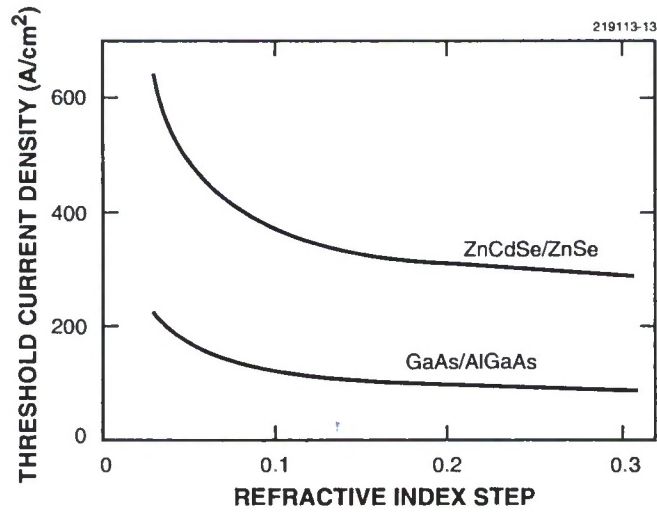


Figure 2-5. Calculated room-temperature threshold current densities  $J_{th}$  vs the refractive index step  $\Delta\mu = \mu_c - \mu_b$  for ZnCdSe/ZnSe and GaAs/AlGaAs quantum wells with an optimized STINSCH structure and  $L_w = 10$  nm.

GaAs/GaAlAs quantum wells with  $L_w = 10$  nm. For  $\Delta\mu = 0.1$ ,  $J_{th}$  is reduced to  $< 400$  A/cm<sup>2</sup> for the ZnCdSe/ZnSe and 125 A/cm<sup>2</sup> for the GaAs/GaAlAs quantum wells. Either ZnCdS or some other II-VI ternary or quaternary material that could be lattice matched to the barrier layers and substrate may be a suitable candidate for the confining layers of the ZnCdSe/ZnSe STINSCH structure.

The calculated low value (400 A/cm<sup>2</sup>) for the threshold current density of the ZnCdSe/ZnSe quantum-well lasers with the STINSCH structure should make its room-temperature CW operation possible, once the problem of good ohmic contacts to the epitaxial structure is resolved.

R. L. Aggarwal  
J. J. Zayhowski  
B. Lax

## 2.2 COHERENT COUPLING OF MICROCHIP ARRAYS

Arrays of diode-pumped solid state microchip lasers [8],[9] are a promising architecture for creating scalable, high-power, rugged sources of laser radiation. Here, we discuss one issue that arises in the field of laser arrays, namely, the potential for coherently coupling the individual lasing elements to reduce the beam divergence.

The on-axis intensity from an array of incoherent emitters scales as the number of emitters  $N$ , and from a coherent array as  $N^2$ . The factor of  $N$  improvement for proposed microchip arrays with  $N = 50$  to 100 per square centimeter is significant. For some proposed systems the benefit to beam brightness is significant for  $N$  as small as 4. This report presents results on coherent coupling of microchip array elements using both evanescent coupling and external cavity techniques.

Microchip lasers are low-loss, low-gain devices with output couplings of only a few percent. Any method to couple the elements of a microchip array must not introduce additional loss to the cavity. Evanescent mode coupling is a method that does not introduce loss, but does require that elements be no more than a few mode radii apart. The coupling strength for two Gaussian modes of radius  $w$  spaced  $s$  apart is  $\eta = \exp(-s^2/2w^2)$ . For  $w = 100$   $\mu\text{m}$  and  $s = 300$   $\mu\text{m}$  (which from the point of view of diode pumping is very close together),  $\eta \approx 0.01$ , so it can be seen that in general mode couplings are very weak. In practice, the spatial modes of microchip lasers have non-Gaussian tails, so that the coupling efficiency is higher than one would calculate for Gaussian modes of the same width. The maximum difference in frequency that two emitters can have and still be locked is  $\Delta f = 2\eta\delta f_{cav}$  where  $\delta f_{cav}$  is the cold-cavity linewidth. This requirement is severe for the microchip array from the point of view of fabrication and pump uniformity, and mandates active control.

We investigated evanescent mode coupling using a Ti:sapphire laser as a pump source. The Ti:sapphire laser beam was divided into as many as four beams, which were imaged onto a 2.2-mm-thick microchip array wafer. The distance between the pump spots could be varied so that the effect of separation on coupling strength could be measured. We observed coherent coupling with two or three spots in a linear arrangement, but not with all four elements lasing. The relative powers in the beams were adjusted with waveplates and polarizers. The microchip lasers had tuning rates of 13 MHz/mW under these pumping conditions. The mode size for a single microchip laser at large separations was 90  $\mu\text{m}$ .

With only two spots being pumped, the differential pump power was adjusted so as to tune the oscillators through the coherent locking range. Measurements were taken at various spot separations. The results and the best fit to the model  $\Delta f = 2\eta\delta f_{\text{cav}} \exp(-s^2/2w^2)$  for element separation  $s$  are plotted in Figure 2-6. The best-fit spot size is twice the measured single-element spot size, showing what is believed to be the effect of the non-Gaussian tail of the microchip lasing mode.

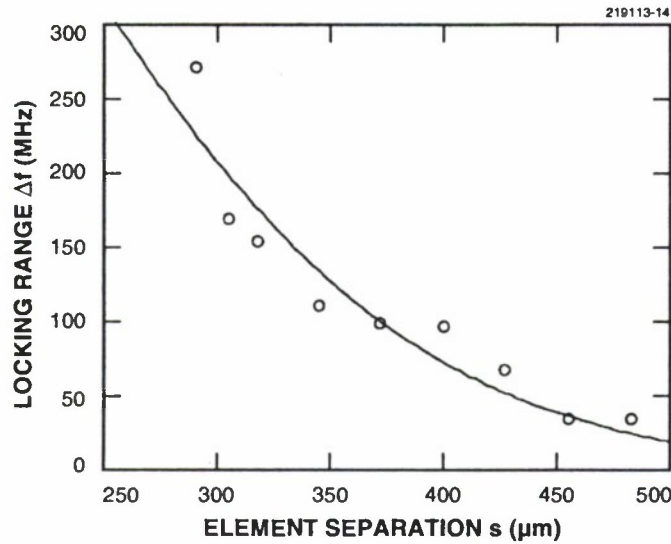


Figure 2-6. Locking range for two microchip elements vs the element separation. The curve represents a theoretical fit to the data, with parameters  $w = 180 \mu\text{m}$  and  $\delta f = 400 \text{ MHz}$ .

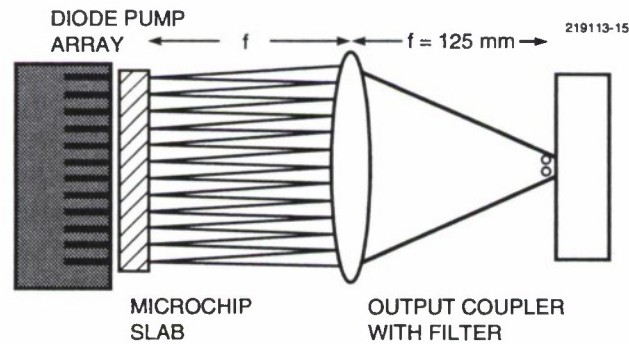


Figure 2-7. Schematic diagram of microchip array coupled using an external cavity.

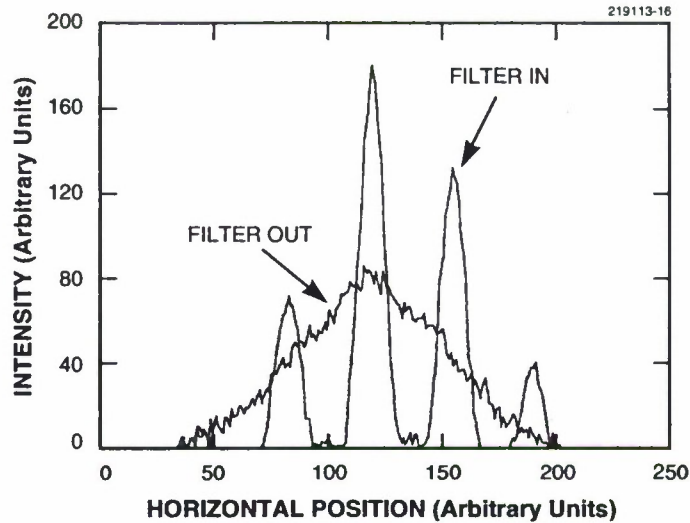


Figure 2-8. Intensity profiles at output coupler for filter in and out.

Another technique for coupling arrays of lasers is to use an external cavity with a diffractive coupler (sometimes regarded as a spatial filter). The coupling element may be placed at a Talbot plane, or at a plane that is a Fourier image of the array. In our work we used an external cavity as shown in Figure 2-7, with a lossy spatial filter at the output coupler. The 2-mm-thick Nd:YAG microchip slab was antireflection coated on the side facing the output coupler. The filter consisted of two 50- $\mu\text{m}$  gold wires spaced a nominal 160  $\mu\text{m}$  apart. The image at the output coupler is a transform image of the pattern at the microchip slab, where there is maximum discrimination between coupled and uncoupled operation of the cavity. An alternative view of the situation is that the filter strongly scatters light into angles determined by the separation of the wires and injects light from one array element into the others.

In the experiments a one-dimensional array of 12 emitters oscillated in six modes, in the inverting imaging cavity. Figure 2-8 shows profiles of the beam for the case when the diffractive wire coupler was either in position or removed. The measured far-field on-axis intensity increased by a factor of 2.1, with the total power of the beam reduced by < 10%. By examining the interference patterns between pairs of elements, we learned that the pattern shown in Figure 2-8 was produced when the elements of the array were locked into two subsets of six elements each. In addition, it was possible to force the array to oscillate with eight elements locked, with the outermost four elements nonlasing. We have also used a phase-only diffractive coupler to coherently lock a linear array of eight microchip lasers. The performance with this configuration was similar to that with the system using the lossy coupler described above, but alignment sensitivity was greatly eased.

C. D. Nabors

### 2.3 EFFECTS OF PHASE ERRORS ON COHERENT EMITTER ARRAYS

Coherent emitter arrays are often put forward as a means for achieving diffraction-limited output beams from a large ensemble of (possibly) low-power optical sources. Agile beam steering and shaping are also potential benefits of coherent arrays, in analogy to phased-array radar antenna technology [10]. Semiconductor lasers have most often been considered for the application of this technique [11]-[14], but research has also been carried out on gas [15] and solid state [16] lasers.

Here, we consider the effect of phase errors in coherent arrays on far-field beam properties. The cases of zero-mean, uncorrelated Gaussian phase errors (the uncorrelated case) and that where nearest-neighbor phase differences (rather than the element phases themselves) are zero-mean Gaussian variables (the correlated case) will be treated.

The uncorrelated phase-error case might apply to a system where a single master oscillator injection locks an ensemble of slave oscillators with identical frequencies but nonzero phase errors. The use of a master oscillator with multiple parallel amplifiers would also lead to uncorrelated phase errors. Correlated phase errors would come about through any scheme (e.g., evanescent-wave or weak diffractive coupling in a common cavity) that phase locks an oscillator array via nearest-neighbor interaction or through series-feed distribution [10] of the array frequency in either an oscillator or amplifier array.

The emitter array is taken to be an  $N_x \times N_y$  rectangular grid with array periods  $d_x$  and  $d_y$ , element phase errors  $\Phi_{jk}$ , and single-element power-normalized field functions  $u_0(x, y)$ . If the near field of the array is denoted by  $u(x, y)$ , the far field  $U(s_x, s_y)$  at angle  $s_x \equiv \theta_x/\lambda$ ,  $s_y \equiv \theta_y/\lambda$  is found in the Fraunhofer theory by taking the Fourier transform [17] of  $u(x, y)$ . The far field can be decomposed as the product of two terms, the single-element far field  $U_0(s_x, s_y)$ , given by

$$U_0(s_x, s_y) = \int u_0(x, y) \exp\left[2\pi i(s_x x + s_y y)\right] dx dy \quad , \quad (2.1)$$

and the far-field grating function  $G(s_x, s_y)$ , given by

$$G(s_x, s_y) = \sum_{j=1}^{N_x} \sum_{k=1}^{N_y} \exp\left(2\pi i j s_x d_x + 2\pi i k s_y d_y + i\Phi_{jk}\right) \quad , \quad (2.2)$$

so that

$$U(s_x, s_y) = U_0(s_x, s_y) G(s_x, s_y) \quad . \quad (2.3)$$



The far-field intensity is calculated by taking the expectation value of the modulus-squared of the far-field amplitude, or

$$\begin{aligned}
 I(s_x, s_y) &= \left\langle \left| U(s_x, s_y) \right|^2 \right\rangle \\
 &= \left| U_0(s_x, s_y) \right|^2 \left\langle \left| G(s_x, s_y) \right|^2 \right\rangle \\
 &= I_0 I_G \quad .
 \end{aligned} \tag{2.4}$$

Note that the far-field grating-function intensity  $I_G$  carries all of the effects of the phase errors, and that in each principal direction it is periodic in  $sd$  with period  $sd = 1$ , or in other words, periodic in angle with period  $\theta = \lambda/d$ . Throughout the following, we define the various  $\phi$ 's as zero-mean uncorrelated Gaussian variables and use them to construct the element phases  $\Phi_{jk}$ . In the uncorrelated case, we take  $\Phi_{jk} = \phi_{jk}$ . In the correlated phase-error case, we take  $\Phi_{jk} - \Phi_{j\pm 1, k} = \phi_{j\pm, k}$  and  $\Phi_{jk} - \Phi_{j, k\pm 1} = \phi_{j, k\pm}$ , so that random-walk statistics apply. The far-field intensity patterns  $I_G$  for the two phase-error cases have been calculated, along with central-lobe angular widths and central-lobe pointing errors. The effects of phase errors on Strehl ratios are presented below as an example of the results.

The Strehl ratio  $S$ , defined as the ratio of peak far-field intensity of a beam divided by the peak intensity from a uniformly illuminated aperture having the same total power, may be decomposed in a manner similar to the far-field intensity as the single-element Strehl ratio

$$S_0 = \frac{|U_0(0,0)|^2}{d_x d_y} \tag{2.5}$$

and the grating-function Strehl ratio

$$S_G = \frac{\langle |G(0,0)|^2 \rangle}{N_x^2 N_y^2} \tag{2.6}$$

so that

$$S = S_0 S_G \quad . \tag{2.7}$$

The Strehl ratio is found for the uncorrelated case to be

$$S_G^{\text{uncorr}} = \exp(-\sigma_\phi^2) + \frac{1}{N_x N_y} \left[ 1 - \exp(-\sigma_\phi^2) \right] \quad , \tag{2.8}$$

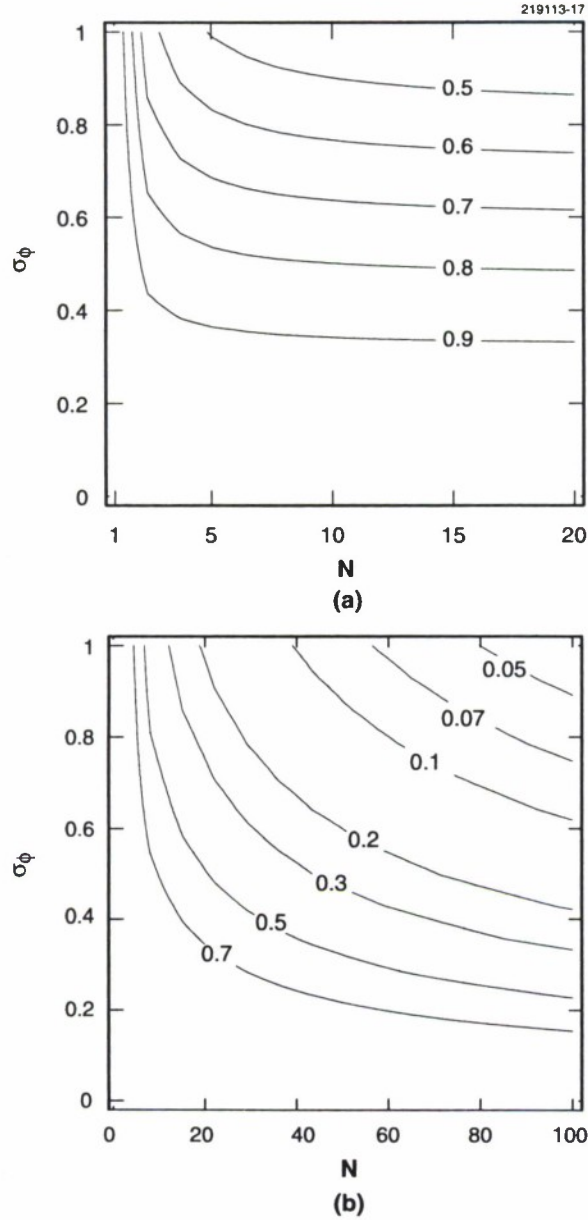


Figure 2-9. Contour plots of Strehl ratios  $S_G^{\text{uncorr},1D}$  and  $S_G^{\text{corr},1D}$  as a function of the number of emitters and the phase-error standard deviation for one-dimensional arrays with (a) uncorrelated phase errors and (b) correlated phase errors.

where  $\sigma_\phi^2$  is the variance of  $\phi$ . A contour plot of this function for a one-dimensional array ( $N_y \rightarrow 1$ ) is shown in Figure 2-9(a). In the limit of large  $N_x N_y$ , the grating-function Strehl ratio becomes  $S_G^{\text{uncorr}} = \exp(-\sigma_\phi^2)$ , in agreement with the continuum case. In the limit of large  $\sigma_\phi$ , the Strehl ratio becomes  $S_G^{\text{uncorr}} = 1/N_x N_y$ , which is the same as that for an incoherent array.

The grating-function Strehl ratio for the correlated one-dimensional case is

$$S_G^{\text{corr,1D}} = \frac{-2\alpha + 2\alpha^{N+1} + N - N\alpha^2}{N^2(1-\alpha)^2} \quad , \quad (2.9)$$

where  $\alpha \equiv \exp(-\sigma_\phi^2/2)$  and  $\beta \equiv 2\pi sd$ ; the two-dimensional result may be found by multiplying one-dimensional results. A contour plot of this function is shown in Figure 2-9(b).

In the limit of large  $\sigma_\phi$ , the grating-function Strehl ratio for the correlated case again approaches  $1/N$ , as in the uncorrelated case. If we first take the limit of large  $N$  and then the limit of small  $\sigma_\phi$ , we find

$$S_G^{\text{corr,1D}} \approx 4/N\sigma_\phi^2 \quad . \quad (2.10)$$

We can define a characteristic number of emitters

$$N_0 \equiv 4/\sigma_\phi^2 \quad , \quad (2.11)$$

and for heuristic purposes assume that we can approximate

$$S_G^{\text{corr,1D}} \approx \frac{1}{1 + N/N_0} \quad . \quad (2.12)$$

The above approximation proves to be accurate to better than 15% for all  $N > 7$ ,  $\sigma_\phi < 1$ . Here  $N_0$  may be interpreted as the effective size of coherent subsets of the array of  $N$  emitters. For  $N > N_0$  the on-axis far-field intensity is only  $N_0$  times greater than for the case of an incoherent array. Note that for an rms emitter-to-emitter phase-difference error of  $2\pi/10$ , i.e., a tenth-wave error between emitters, the largest subset size is only  $\sim 10$ .

In summary, closed-form solutions for far-field intensities for emitter arrays with uncorrelated and nearest-neighbor-correlated phase errors were calculated. For the correlated case, an effective coherent subset size of  $N_0 = 4/\sigma_\phi^2$  was discovered, based on Strehl ratio considerations. These results could be useful in specifying phase-error tolerances, and thus array fabrication and operating tolerances, in coherent arrays to ensure that the maximum benefit of coherent operation be achieved.

C. D. Nabors

## REFERENCES

1. M. A. Haase, J. Qiu, J. M. DePuydt, and H. Cheng, *Appl. Phys. Lett.* **59**, 1272 (1991).
2. H. Jeon, M. Hagerott, J. Ding, A. V. Nurmiko, W. Xie, D. C. Grillo, M. Kobayashi, R. L. Gunshore, G. C. Hua, and N. Otsuka, presented at the IEEE 50th Annual Conference on Device Research, Cambridge, Mass., 22–24 June 1992.

3. Z. Yu, J. Ren, B. Sneed, K. Bowers, J. W. Cook, Jr., J. F. Schetzina, G. C. Hua, and N. Otsuka, presented at the IEEE 50th Annual Conference on Device Research, Cambridge, Mass., 22–24 June 1992.
4. *New Technol. Jpn.* **20**(6), 6 (1992).
5. N. K. Dutta, *J. Appl. Phys.* **53**, 7211 (1982); G. P. Agrawal and N. K. Dutta, *Long-Wavelength Semiconductor Lasers* (Van Nostrand Reinhold, New York, 1986).
6. R. L. Aggarwal, J. J. Zayhowski, and B. Lax, submitted to *Appl. Phys. Lett.*
7. D. Ahn, T.-K. Yoo, and H. Y. Lee, *Appl. Phys. Lett.* **59**, 2669 (1991).
8. J. J. Zayhowski and A. Mooradian, *Opt. Lett.* **14**, 24 (1989).
9. C. D. Nabors, A. Sanchez, and A. Mooradian, *Opt. Lett.* **17**, 1587 (1992).
10. M. Skolnik, ed., *Radar Handbook*, 2nd ed. (McGraw Hill, New York, 1990), Chap. 7.
11. D. Botez and D. E. Ackley, *IEEE Circuits Devices Mag.* **2**, 8 (1986).
12. N. W. Carlson, G. A. Evans, J. M. Hammer, M. Lurie, S. L. Palfrey, and A. Dohlakia, *Appl. Phys. Lett.* **50**, 1301 (1987).
13. J. R. Leger, M. L. Scott, and W. B. Veldkamp, *Appl. Phys. Lett.* **52**, 1771 (1988).
14. C. J. Corcoran and R. H. Rediker, *Appl. Phys. Lett.* **59**, 759 (1991).
15. A. A. Golubentsev, O. R. Kachurin, F. V. Lebedev, and A. P. Napartovick, *Sov. J. Quantum Electron.* **20**, 934 (1990).
16. C. D. Nabors, presented at the IEEE Lasers and Electro-Optics Society Annual Meeting, Boston, Mass., 16–19 November 1992.
17. J. W. Goodman, *Introduction to Fourier Optics* (McGraw-Hill, San Francisco, 1968), Chap. 4.

### 3. MATERIALS RESEARCH

#### 3.1 REDUCTION OF OPTICAL CROSS TALK IN PtSi SCHOTTKY-BARRIER INFRARED FOCAL PLANE ARRAYS

Optical cross talk is a commonly observed phenomenon in infrared staring focal plane arrays (FPAs). Such cross talk is undesirable because it causes smearing of the object image and therefore affects the ability to identify and accurately track a target. For PtSi Schottky-barrier FPAs, where sensing of photoelectrons takes place in regions of the thin silicide film that are physically separated, optical cross talk between adjacent pixels should be negligible. However, images of very high intensity sources obtained with back-illuminated FPAs exhibit cross talk that is characterized by a cruciform pattern. It has been proposed [1] that this pattern is caused by the combined effects of diffraction and reflection at the Si/air interface, as shown schematically in Figure 3-1(a). When incident radiation passes through the Si substrate onto the pixel, a small fraction is reflected off axis because the regular pattern of features in the pixel acts as a reflective diffraction grating. The diffracted radiation is then reflected from the back surface of the Si, and a small fraction is collected by adjacent pixels. An example of the cruciform pattern is shown in Figure 3-1(b), which is a medium-wavelength infrared (MWIR) image obtained from a  $320 \times 244$ -element PtSi array. The intense radiation from a freshly extinguished match, which is estimated to be at a temperature of several hundred degrees centigrade, generates multiple well-defined intensity lobes along the vertical and horizontal directions. The location and magnitude of these lobes depend on the pixel geometry and FPA thickness.

One scheme to reduce optical cross talk is to use the front-illuminated configuration. As shown in Figure 3-2(a), the radiation that is transmitted through the pixel is completely absorbed in the heavily doped  $p^+$ -Si substrate because of high free-carrier absorption. As a result, the cruciform pattern is totally absent from the MWIR image shown in Figure 3-2(b). The disadvantage of the front-illuminated configuration is that an optical cavity structure [2] cannot be applied, and the FPA sensitivity is therefore reduced by about a factor of 2–3. However, for applications where the target signature is intense and localized, and precise determination of target position is important, the front-illuminated configuration should be an attractive candidate.

Another scheme to reduce optical cross talk is to use the thin back-illuminated configuration, as shown in Figure 3-3. In this approach, a lightly doped Si substrate is chemically thinned from a typical thickness of  $350\text{ }\mu\text{m}$  to  $\sim 15\text{ }\mu\text{m}$ . Since almost all the absorption losses occur in the PtSi layer, the total loss per round trip of the reflected light, and therefore the effective number of round trips, is essentially independent of the thickness of the Si substrate. Under those circumstances, the lateral spreading of the radiation is proportional to substrate thickness, so decreasing the thickness by a factor of 20 reduces the extent of the cruciform pattern by the same factor. Figures 3-4(a) and 3-4(b) show horizontal-line video outputs of high-intensity point-source imagery obtained from a thick PtSi array and a thin PtSi array, respectively. Both arrays were operated in the back-illumination mode. The blackbody point-source target is set at  $260^\circ\text{C}$ , resulting in a detector output that is  $\sim 20$  times the saturation level. As can be seen in Figure 3-4, the imagery from the thick array clearly shows first- and second-order sidelobes, whereas the



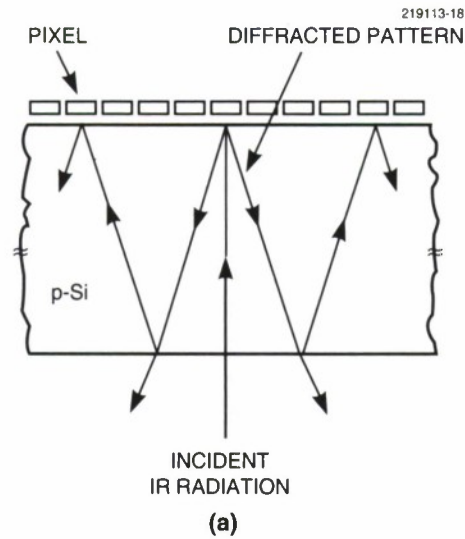


Figure 3-1. (a) Schematic diagram showing optical cross talk in back-illuminated focal plane array (FPA). (b) Cruciform pattern formed from the image of a high-intensity source as a result of optical cross talk.

imagery from the thin array shows a gradual decrease of the central lobe without any sidelobes. Compared to the front-illuminated configuration described above, the thin back-illuminated approach is not as effective in suppressing cross talk but has the advantage of higher sensitivity because the optical cavity structure can still be applied in this case. In addition, microlens arrays [3] can be incorporated on the back side of the thin Si substrate to further improve array sensitivity.

B-Y. Tsaur  
A. H. Loomis  
C. K. Chen

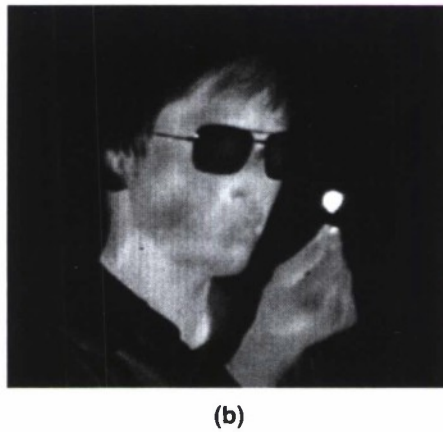
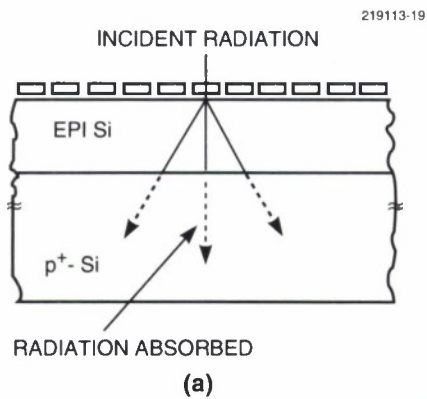


Figure 3-2. (a) Schematic diagram showing suppression of optical cross talk in front-illuminated FPA. (b) Medium-wavelength infrared image of the same high-intensity source as in Figure 3-1(b) but absent of the cruciform pattern.

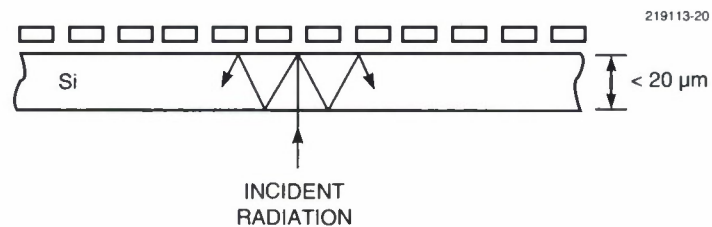


Figure 3-3. Schematic diagram showing reduction of optical cross talk in thin back-illuminated FPA.

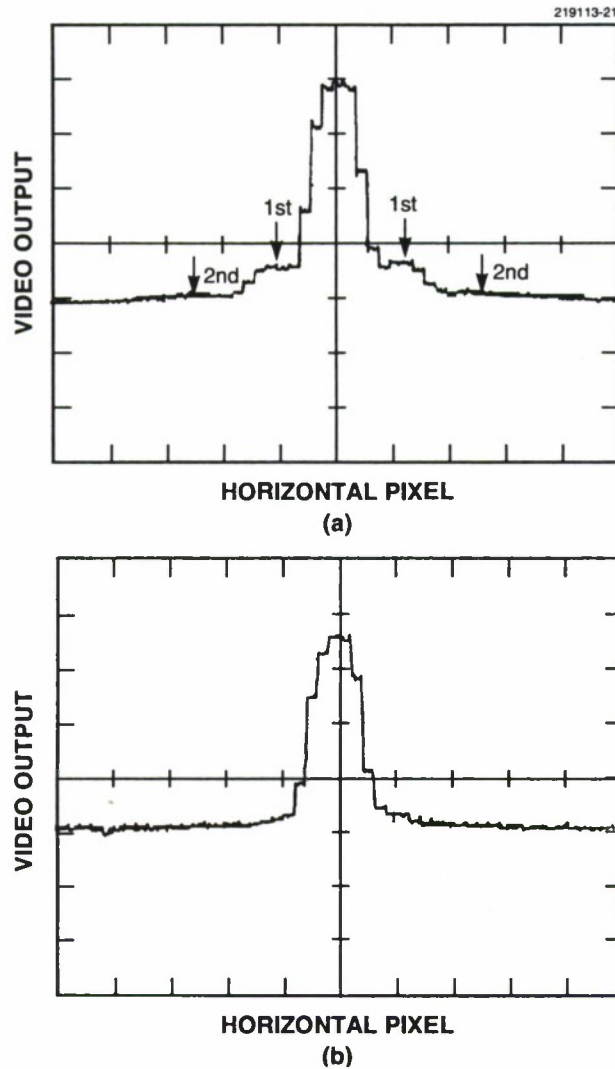


Figure 3-4. Horizontal video line outputs of high-intensity point-source imagery obtained from (a) a thick PtSi FPA and (b) a thin PtSi FPA.

### 3.2 BARRIER-THICKNESS DEPENDENCE OF PHOTOLUMINESCENCE FOR STRAINED-LAYER InGaAs/GaAs COUPLED QUANTUM WELLS

Strained-layer InGaAs/(Al)GaAs quantum-well diode lasers are of great interest because these devices can have emission wavelengths in the range 0.9–1.1  $\mu\text{m}$  (between the wavelength for lattice-matched GaAs- and InP-based lasers) and can exhibit low threshold current density, high output power, high modulation bandwidth, and good reliability. In designing laser structures that contain strained-layer

multiple quantum wells (MQWs), it is necessary to consider the structural and optical qualities of such structures. Previously, we have shown [4] that the critical thickness for InGaAs/GaAs MQW structures depends on the thickness of the GaAs barrier layer, and can be described by the Matthews and Blakeslee force-balance model [5] assuming misfit dislocations formed by the single-kink mechanism. Here, we report photoluminescence (PL) properties of coupled strained-layer InGaAs/GaAs MQWs as a function of the GaAs barrier thickness.

The MQW structures were grown by organometallic vapor phase epitaxy in a vertical rotating-disk reactor on  $n^+$ -GaAs substrates oriented  $2^\circ$  off (001) toward the nearest [110]. The source materials were trimethylgallium, trimethylindium, and 100% arsine. The  $\text{In}_x\text{Ga}_{1-x}\text{As}/\text{GaAs}$  MQW layers were grown at  $625^\circ\text{C}$  with a V/III ratio of 300. The growth rates of InGaAs and GaAs layers were determined *ex situ* by double-crystal x-ray diffraction (DCXRD) and Dektak step height measurements. The MQW structure shown in Figure 3-5 consists of three  $\text{In}_{0.3}\text{Ga}_{0.7}\text{As}$  quantum wells (QWs) separated by GaAs barrier layers and was grown on a  $0.4\text{-}\mu\text{m}$ -thick GaAs buffer layer. The QW thickness  $t_w$  ranged from 2.0 to 2.8 nm and the GaAs barrier layer thickness  $t_B$  ranged from 0.8 to 16 nm. The InGaAs layers are fully strained without misfit dislocations according to the Matthews-Blakeslee model. The samples were characterized by means of DCXRD and PL at room temperature and 6 K.

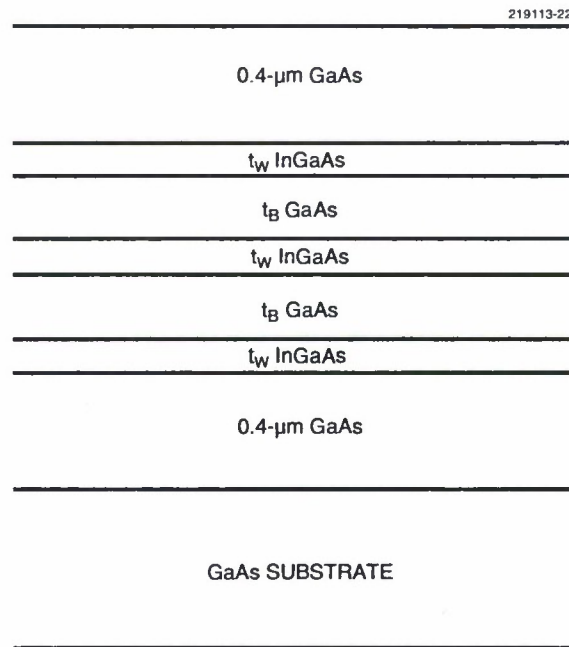


Figure 3-5. Schematic structure of InGaAs/GaAs multiple-quantum-well (MQW) samples.

To confirm the structure of the samples, experimental DCXRD rocking curves were compared with simulated curves. Figure 3-6 shows the experimental curve for a three-QW structure intended to have  $t_w = 2$  nm,  $t_B = 16$  nm, and  $x = 0.3$ , and the simulated curve calculated according to the Taupin-Tagachi solution to dynamical x-ray diffraction theory. Since the layers are below the critical thickness for dislocation formation, the InGaAs layers are considered to be completely strained. Agreement between the curves was obtained by using values of  $t_w = 2$  nm,  $t_B = 15.9$  nm, and  $x = 0.32$  in the simulation, which confirms the accuracy of our growth calibrations and control of the growth of extremely thin layer structures.

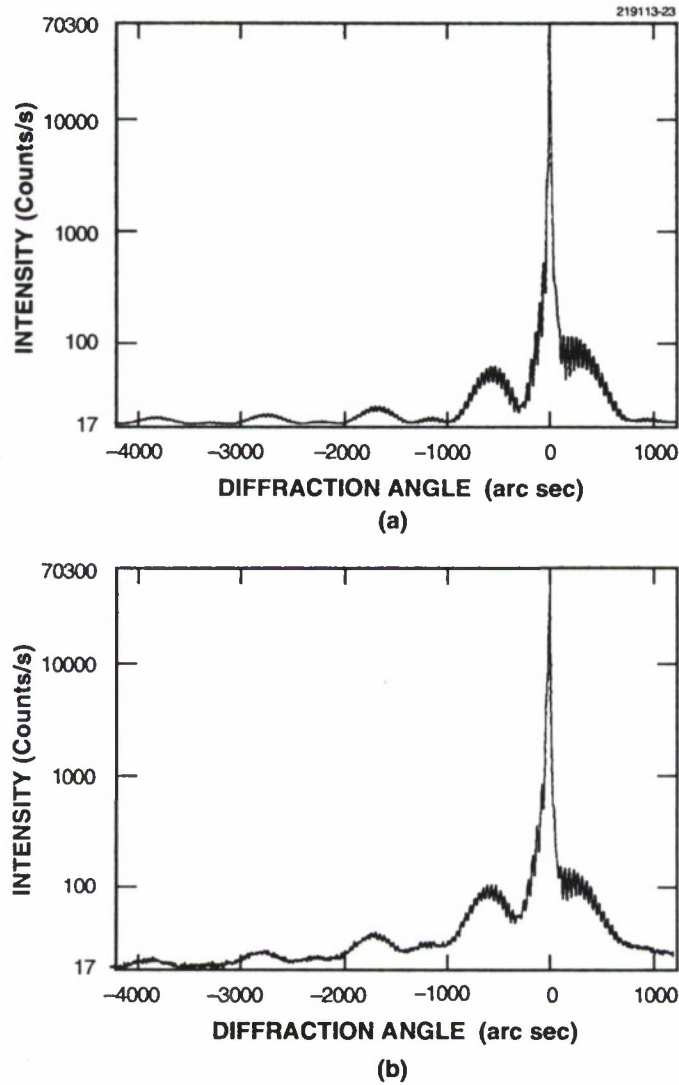


Figure 3-6. Double-crystal x-ray diffraction rocking curves of InGaAs/GaAs MQW structure: (a) simulation and (b) experiment.



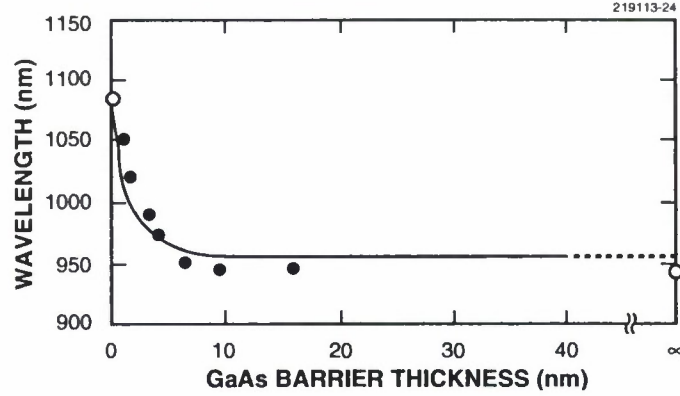


Figure 3-7. Room-temperature emission wavelength as a function of GaAs barrier layer thickness for three-quantum-well samples with  $x = 0.3$  and  $t_w = 2.0$  nm. The open circles at zero and infinite barrier thickness are results for single-quantum-well samples with  $t_w = 6$  and  $2$  nm, respectively.

The dependence of room-temperature PL emission wavelength  $\lambda$  on  $t_B$  is shown in Figure 3-7 for three-QW samples with  $x = 0.3$  and  $t_w = 2.0$  nm. The open circles at zero and infinite barrier thickness are results for single-quantum-well (SQW) samples with  $t_w = 6$  and  $2$  nm, respectively. The value of  $\lambda$  shifts to longer wavelengths with decreasing  $t_B$  because of the increasing coupling of the electronic wave functions for the individual wells. The upper and lower limits on  $\lambda$  are given by the extreme cases of three QWs with zero or infinite barrier thicknesses, respectively. An SQW of  $t_w = 6$  nm has  $\lambda = 1084$  nm, while an SQW of  $t_w = 2$  nm has  $\lambda = 948$  nm. The solid curve shown in Figure 3-7 is the wavelength associated with the lowest calculated transition energy of the three-QW system. The calculation takes account of the increase in bulk energy gap and the splitting of the heavy- and light-hole valence bands which results from the biaxial compressive strain. Square potential wells were assumed and continuous probability-current-density boundary conditions were used [6]. For  $\text{In}_{0.3}\text{Ga}_{0.7}\text{As}$  on GaAs, we employed a strained energy gap of  $1.067$  eV, a conduction band offset of  $0.252$  eV, and a heavy-hole valence band offset of  $0.105$  eV. For  $t_B > 8$  nm, the QWs are essentially uncoupled and the wavelength is constant. As  $t_B$  decreases, each of the degenerate quantized levels in the three wells splits into three levels of the coupled system. The splitting decreases the lowest transition energy as indicated in Figure 3-7. As  $t_B$  approaches zero, the lowest energy of the  $n = 1$  split level of the coupled QWs approaches that of the  $n = 1$  level of an SQW whose thickness is 3 times that of the individual wells. Similar results were obtained for the thicker QWs having  $t_w = 2.4$  and  $2.8$  nm, but with narrower wavelength ranges, as expected. Therefore, in designing MQW strained-layer diode laser structures for emission within a specific wavelength range, this variation in  $\lambda$  with  $t_B$  must be considered.

The low-temperature PL linewidth (full width at half-maximum [FWHM]) for the samples of Figure 3-7 are shown in Figure 3-8. The FWHM is a minimum of  $15$  meV for both SQW samples with  $t_w = 2$  and  $6$  nm, while the coupled QWs have higher FWHM with a maximum occurring for  $1.6 \text{ nm} < t_B < 4$  nm. The intensity of PL spectra was similar for all samples except the SQW with  $t_w = 6$  nm, whose

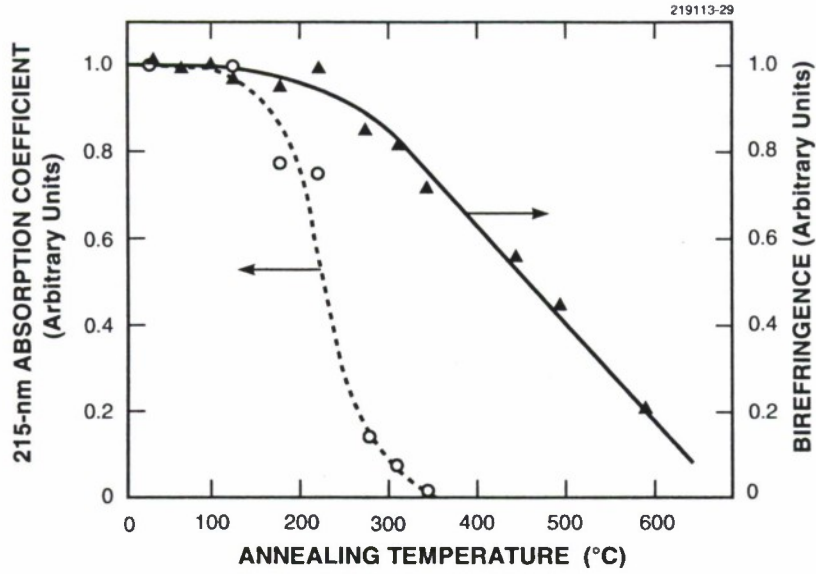


Figure 3-8. Low-temperature (6 K) photoluminescence linewidth as a function of GaAs barrier layer thickness for the same samples as in Figure 3-7.

intensity was about 3 times greater. The PL linewidth depends on the quality of the layers and abruptness of interfaces. Broadening of ternary QWs can be due to intrinsic and extrinsic mechanisms. Intrinsic broadening is the alloy broadening from potential fluctuations resulting from the random distribution of the Ga and In atoms. Extrinsic broadening is due to well thickness fluctuations. For MQW structures, variations in well and/or barrier thicknesses can lead to PL broadening. Splitting of the QW levels might also play a role. However, for  $t_B = 1.6$  nm, where the FWHM is a maximum, the splitting is comparable to the FWHM. Since the FWHM for the 2- and 6-nm SQW samples is the same, we conclude that well thickness fluctuations of the individual well are small. The small increase in FWHM to 21 meV for  $t_B = 16$  nm when the wells are uncoupled indicates that well-to-well thickness variations are small. The large increase in FWHM for  $1.6 \text{ nm} < t_B < 4 \text{ nm}$  can therefore be attributed to coupling effects.

C. A. Wang	J. P. Donnelly
J. H. Reinold	D. R. Calawa

### 3.3 GROWTH AND CHARACTERIZATION OF MBE-GROWN EPITAXIAL $\text{Bi}_{0.9}\text{Sb}_{0.1}$ FILMS

Epitaxial  $\text{Bi}_{0.9}\text{Sb}_{0.1}$  films with low carrier concentrations and record high electron mobilities at 77 K have been grown on large ( $18 \times 18 \times 1$  mm), [111]-oriented, cleaved, single-crystal  $\text{BaF}_2$  substrates by molecular beam epitaxy (MBE). Electron mobilities as high as  $26\,000 \text{ cm}^2/\text{V s}$  at 300 K and  $665\,000$

$\text{cm}^2/\text{Vs}$  at 77 K were obtained. Electron carrier concentrations as low as  $6.3 \times 10^{16} \text{ cm}^{-3}$  at 77 K were determined. These electrical properties represent a substantial improvement over previously reported values for epitaxial BiSb alloys [7].

Several years ago the growth of epitaxial single-crystal BiSb films was reported for the first time [7]. Here, a second BiSb epitaxial film growth investigation is reported. The BiSb films were grown using a modified Varian 360 MBE system which has ion-pumped load-lock and growth chambers. The base pressure in the growth chamber during growth was kept in the range  $3$  to  $5 \times 10^{-10}$  Torr. The growth chamber is equipped with a quadruple mass analyzer, beam-flux-monitoring and base-monitoring ion gauges, and a reflection high-energy electron diffraction (RHEED) system. Growth rates were in the range  $1$ – $3 \text{ } \mu\text{m/h}$ .

After the growth of a thin nucleation layer [7] at  $100^\circ\text{C}$  (growth time 75 s), the substrate temperature during growth was held constant at  $250^\circ\text{C}$ . RHEED streaks typical of high-quality epitaxy were observed during and at the end of growth.

The lattice constants of the cubic  $\text{BaF}_2$  substrate and the grown rhombohedral (slightly distorted cubic)  $\text{Bi}_{0.9}\text{Sb}_{0.1}$  films were calculated from x-ray diffraction measurements along the [444] crystallographic direction. Diffraction patterns from a  $\text{BaF}_2$  substrate and an early  $\text{Bi}_{0.9}\text{Sb}_{0.1}$  epilayer are shown in Figure 3-9. The lattice constant of the cubic  $\text{BaF}_2$  substrate is  $0.6201 \text{ nm}$  as calculated from the results shown in Figure 3-9(a), which is in good agreement with the literature value of  $0.6200 \text{ nm}$ . The lattice constant of the  $\text{Bi}_{0.9}\text{Sb}_{0.1}$  epilayer is  $0.6804 \text{ nm}$  as calculated from the results in Figure 3-9(b). However, diffraction data in Figure 3-9(b) are for the trigonal direction. The lattice constant relevant to substrate lattice match and crystal growth quality is that in the growth plane, which is the crystalline direction normal to the trigonal axis. The average cubic lattice parameter of  $0.6534 \text{ nm}$  obtained from bulk crystal data [8],[9] was used to calculate an in-trigonal-plane lattice parameter of  $0.6402 \text{ nm}$ , which is only 3.2% larger than the lattice constant of  $\text{BaF}_2$ . The clear resolution of the two  $K_a$  lines indicates that good-quality epilayer growth and good alloy homogeneity have been achieved. Figure 3-10(a) shows an optical photomicrograph of a (111) cleaved cross section of a  $20\text{-}\mu\text{m}$ -thick  $\text{Bi}_{0.9}\text{Sb}_{0.1}$  layer, and Figure 3-10(b) shows a typical as-grown surface. The surface morphology is smooth, except for cleavage steps from the cleaved  $\text{BaF}_2$  surface and shallow ( $< 1 \text{ } \mu\text{m}$  deep), oriented, triangular-shaped, thermal dislocation etch pits ( $\sim 5 \text{ } \mu\text{m}$  on a side), which are observed over the entire surface. The RHEED observations, x-ray diffraction measurements, and surface morphology results indicate that high-quality epilayers are being grown.

Hall coefficient and electrical resistivity of the  $\text{Bi}_{0.9}\text{Sb}_{0.1}$  epilayers were measured at 300 and 77 K. Also the Seebeck coefficient (sometimes referred to as thermopower) was measured at room temperature. For the Hall measurements a magnetic field strength of 5 kG was used, and the magnetic field direction was oriented perpendicular to the film plane. The Hall coefficient components and the resistivity are isotropic in the trigonal plane because of crystal symmetry. Results of measurements made on  $9 \times 9\text{-mm}$  samples using the van der Pauw technique are displayed in Table 3-1. The mobility values are for the electrons along the binary axis of the three L-conduction band ellipsoids. The average in-plane mobility of all electrons or the conductivity mobility is 55% of the values displayed in Table 3-1. Sample T-46 was removed from the substrate, and electrical measurements were made on the free-standing  $20\text{-}\mu\text{m}$ -thick foil. The unusually high mobility and low carrier concentration at 77 K are believed to be due to

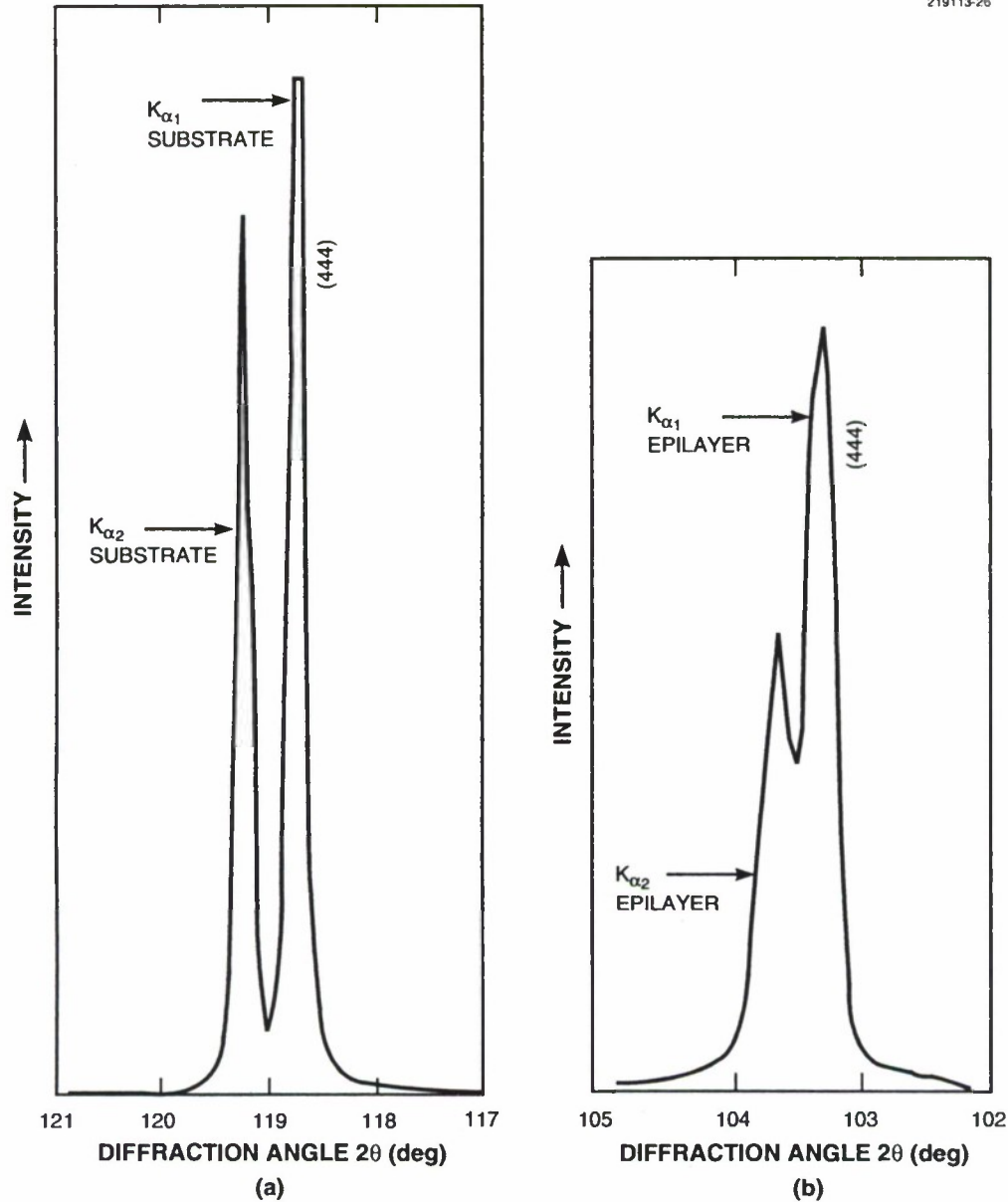


Figure 3-9. [444] x-ray diffraction lines for (a) a (111)  $\text{BaF}_2$  substrate and (b) an early  $\text{Bi}_{0.9}\text{Sb}_{0.1}$  film grown by molecular beam epitaxy (MBE).

a change from a semimetal at 300 K to a zero or a very small energy gap semiconductor at 77 K. The results in Table 3-1 show that as the growth rate increases the purity of the layers improves. It is believed that the background flux is doping the films and the higher BiSb flux reduces the effect of the background dopant. From the Seebeck coefficient and electrical resistivity measurements the value for the thermoelectric



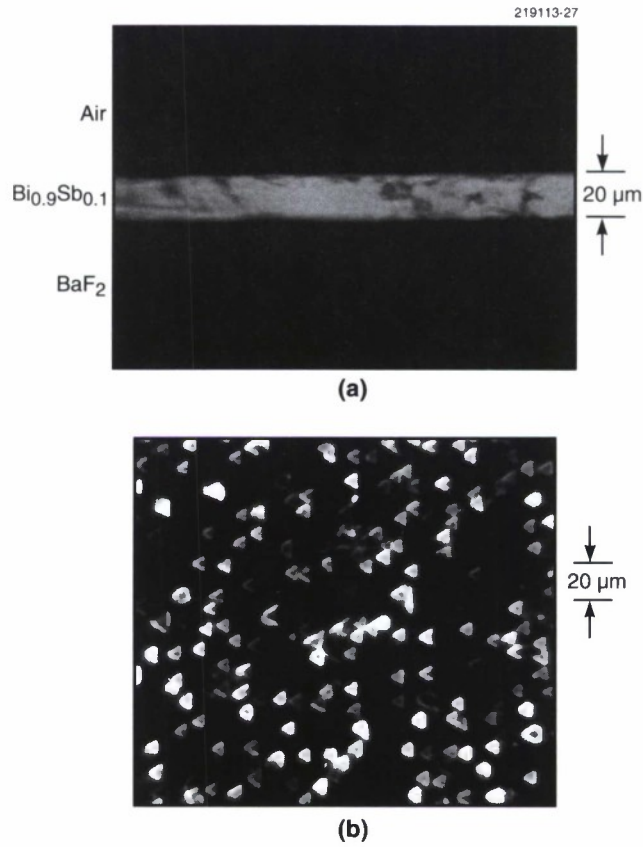


Figure 3-10. Optical micrographs of (a) a cleaved cross section of a  $\text{Bi}_{0.9}\text{Sb}_{0.1}$  MBE-grown film on a (111)  $\text{BaF}_2$  substrate and (b) the as-grown surface of the  $\text{Bi}_{0.9}\text{Sb}_{0.1}$  film.

figure of merit  $ZT$  is calculated to be 0.35 for sample T-26 using the Wiedemann-Franz law and the literature value of  $9\ \text{mW cm}^{-1}\text{K}^{-1}$  for the lattice thermal conductivity. Within experimental uncertainty this  $ZT$  value is equivalent to the highest room-temperature bulk crystal value of 0.36 for undoped BiSb in the trigonal plane. In conclusion, BiSb layers of crystal quality comparable with the best bulk material have been prepared by MBE.

T. C. Harman



**TABLE 3-1**  
**Some Physical Properties of MBE-Grown Epitaxial BiSb Films**

Sample	Growth Rate ( $\mu\text{m/h}$ )	300-K Mobility ( $\text{cm}^2/\text{V s}$ )	300-K Carrier Concentration ( $\text{cm}^{-3}$ )	77-K Mobility ( $\text{cm}^2/\text{V s}$ )	77-K Carrier Concentration ( $\text{cm}^{-3}$ )	300-K Seebeck Coefficient ( $\mu\text{V/K}$ )
Ref. 7	—	—	$2.1 \times 10^{18}$	120 000	$3.2 \times 10^{17}$	—
T-16	1	3 300	$3.8 \times 10^{19}$	6 700	$4.1 \times 10^{19}$	−50
T-26	2	12 000	$7.6 \times 10^{18}$	63 000	$5.6 \times 10^{17}$	−81
T-45	3	24 000	$2.9 \times 10^{18}$	665 000	$6.3 \times 10^{16}$	−79
T-46*	3	26 000	$3.5 \times 10^{18}$	420 000	$6.9 \times 10^{16}$	—
*Free foil.						

### REFERENCES

1. J. M. Mooney, *Proc. SPIE* **1107**, 2 (1989).
2. W. F. Kosonocky, F. V. Shallcross, T. S. Villani, and J. V. Groppe, *IEEE Trans. Electron Devices* **ED-32**, 1564 (1985).
3. Solid State Research Report, Lincoln Laboratory, MIT, 1992:1, p. 18.
4. Solid State Research Report, Lincoln Laboratory, MIT, 1992:3, p. 19.
5. J. W. Matthews and A. E. Blakeslee, *J. Cryst. Growth* **27**, 118 (1974).
6. H. Kawai, J. Kaneko, and N. Watanabe, *J. Appl. Phys.* **58**, 1263 (1985).
7. D. T. Morelli, D. L. Partlin, and J. Heremans, *Semicond. Sci. Technol.* **5**, S257 (1990).
8. M. H. Coppen, L. M. Falicov, and S. Golin, *IBM J. Res. Dev.* **8**, 215 (1964).
9. P. Cucka and C. S. Barrett, *Acta Crystallogr.* **15**, 865 (1962).

## 4. SUBMICROMETER TECHNOLOGY

### 4.1 OPTICAL MATERIALS FOR USE WITH EXCIMER LASERS

Optical lithography for semiconductor device fabrication has been shifting in recent years to shorter wavelengths. As the dimensions of integrated circuits are reduced to the 0.25- $\mu\text{m}$  regime and below, it is widely expected that mainstream photolithographic systems will employ 248- or 193-nm excimer laser radiation. One area of concern at these wavelengths, however, is the availability of adequate optical materials from which lenses, mirrors, output couplers, and other optical components can be fabricated. Specifically, candidate optical materials should be fully transparent at their intended wavelength of use, and their properties (including transparency) should not be degraded by extended irradiation with the excimer laser. In this report, we present results of studies of optical materials at 193 nm, which were aimed at evaluating their suitability for lithographic applications. These results may be extended to other wavelengths and applications using appropriate scaling factors.

Only a few optical materials are transparent at 193 nm. These include high-purity synthetic fused silica and some high-purity crystalline fluorides (calcium, magnesium, lithium, barium, and sodium); sapphire ( $\text{Al}_2\text{O}_3$ , ultraviolet [UV] grade) is only partially transparent at 193 nm because of an absorptive band centered at  $\sim 200$  nm, which is caused by a crystalline defect. Although fused silica and the fluorides listed above are nominally fully transparent at 193 nm, in practice absorption coefficients ranging from 0.005 to 0.10  $\text{cm}^{-1}$  have been measured, depending on the material, the grade, and the supplier. It should be noted that the suitability of a particular material for an intended application is also impacted by other properties. For instance,  $\text{MgF}_2$  and  $\text{Al}_2\text{O}_3$  are birefringent, and NaF and LiF are hygroscopic and mechanically soft.

Synthetic UV-grade fused silica is frequently the material of choice for optical components to be used with excimer lasers. Several suppliers offer a variety of materials, which differ in index homogeneity and amount of impurities. The most common impurity is hydroxyl (OH) radicals. In fact, fused silica is sometimes classified as "wet" or "dry," depending on whether the OH concentration is  $\sim 100$ –1000 ppm or 10 ppm, respectively. From our experience wet fused silica is significantly better suited for excimer use than the dry variety, and the remainder of this report will discuss only the wet kind. Other impurities may include Cl ions (up to  $\sim 100$  ppm if the material is grown in flame hydrolysis of  $\text{SiCl}_4$ ) as well as a range of metal ions (typically at ppm levels and below). Index inhomogeneity can be as low as 0.5 ppm over a 6-in. slab. The lowest absorption coefficient of fused silica at 193 nm has been measured to be 0.005  $\text{cm}^{-1}$  (base  $e$ ). This degree of transparency is sufficient for most photolithographic system designs.

Irradiation of fused silica at 193 nm induces two changes, which in the grades we have tested are constant at least for several weeks and probably for several months [1],[2]: formation of absorptive color centers with peaks at  $\sim 215$  nm and densification (compaction) of the material. The color centers are ascribed to  $\text{E}'$  centers [3], which are oxygen vacancies in the  $\text{SiO}_2$  network, with an unpaired electron on the silicon atom. The compaction has two consequences: reduction of the geometrical thickness of the material and increase of its index of refraction. Both effects are typically at the 1–50-ppm level and

therefore may not be of practical significance except in the most demanding applications, such as photolithography. The net change in optical path is readily observed with a phase-measuring interferometer. The compaction is also observed indirectly, by the stress-induced birefringence in the zones adjacent to the irradiated area, which connect the compacted portion to the uncompacted one. Although currently not fully understood on the atomic level, the compaction is apparently related to the glassy structure of fused silica and to changes in its medium-range order [4].

The formation of color centers and the compaction are both initiated by the same two-photon absorption process. At 193 nm, the coefficient for two-photon absorption is  $\alpha_1 \approx 2 \times 10^{-3}$  cm/MW, while at 248 nm it is  $\sim 10$  times smaller [5]. Thus, for a typical 20-ns-long pulse, at a moderate fluence of 100 mJ cm<sup>-2</sup>/pulse, the Beer-Lambert absorption coefficient is  $\sim 0.01$  cm<sup>-1</sup> at 193 nm and 0.001 cm<sup>-1</sup> at 248 nm. The two-photon absorption model predicts a quadratic dependence of color centers and compaction on laser fluence and a linear dependence on the number of pulses. Indeed, such behavior has been observed experimentally at low defect densities. Saturation-like effects are noted when the laser-induced peak absorption at 215 nm exceeds  $\sim 0.10$  cm<sup>-1</sup> and the compaction exceeds  $\sim 20$  ppm.

As mentioned above, two-photon absorption is the initiating step for the formation of color centers and compaction. The absorbed energy is converted into excitons and conduction electrons, whose nonradiative decay leads eventually to the observed material changes [6]. Figure 4-1 shows the effect of irradiation temperature on the amount of E' centers and compaction: in the range 20–100°C, defect formation increases rapidly with substrate temperature during irradiation. This behavior is attributed to changes with temperature in the branching ratio between the radiative and nonradiative decay paths of excitons. Above  $\sim 100^\circ\text{C}$  the color centers seem to undergo partial self-annealing, while the compaction does not. Figure 4-2 further demonstrates the difference between the two phenomena. In this figure the 215-nm absorption coefficient and the compaction-induced birefringence are plotted as functions of post-irradiation annealing temperature. The E' centers are fully annealed at  $\sim 350^\circ\text{C}$ , and in agreement with Figure 4-1 partial annealing starts at  $\sim 100^\circ\text{C}$ . In contrast, partial annealing of the compaction begins at  $\sim 150^\circ\text{C}$ , and full annealing is not achieved even at 600°C. These results indicate that the E' centers and compaction are not directly related to each other. Rather they are the outcomes of two different sequences of solid state reactions that start with the same two-photon absorption.

While the model presented above predicts a functional dependence of laser-induced defects on irradiation parameters, it cannot predict the quantitative values of the laser-induced absorption or the compaction. Such values depend on the details of the solid state reactions following the two-photon absorption, and these reactions are strongly affected by subtle differences in the glassy structure and level of impurities. Indeed, the amount of laser-induced color center formation varies from grade to grade and may strongly depend on the details of material formation and any other pre-irradiation treatments. For instance, Suprasil 311 can be pretreated to cause a sevenfold reduction in the excimer-induced density of E' centers. Note, however, that the same treatment does not affect the amount of laser-induced compaction, in agreement with the results of Figure 4-2 above. Figure 4-3 shows that even within the same grade of fused silica the color center formation may vary significantly with a subtle variable such as location in the boule. It is therefore apparent that a careful choice of materials used in excimer applications is required, and preselection and pretesting may be desirable.



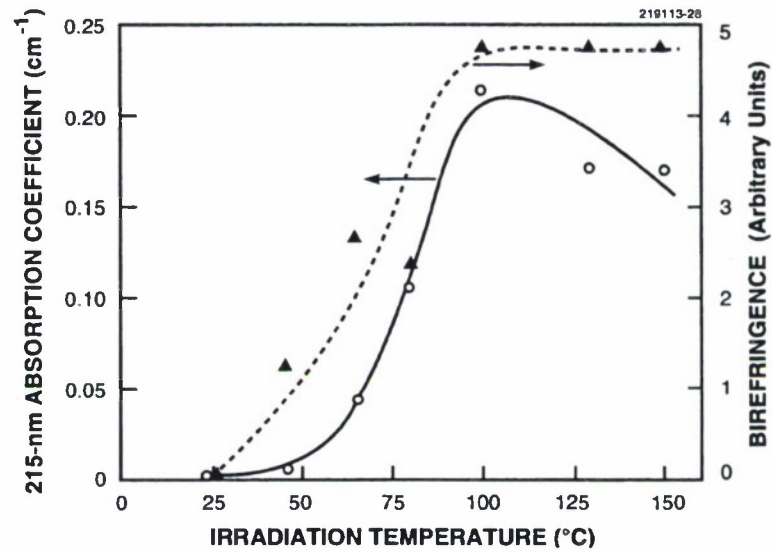


Figure 4-1. Plot of 193-nm-induced color centers (left-hand ordinate) and birefringence (right-hand ordinate) in a 1-cm-thick sample of Suprasil 2, as a function of the sample temperature during irradiation. The exposure conditions were  $1.4 \times 10^6$  pulses,  $17 \text{ mJ cm}^{-2}/\text{pulse}$ .

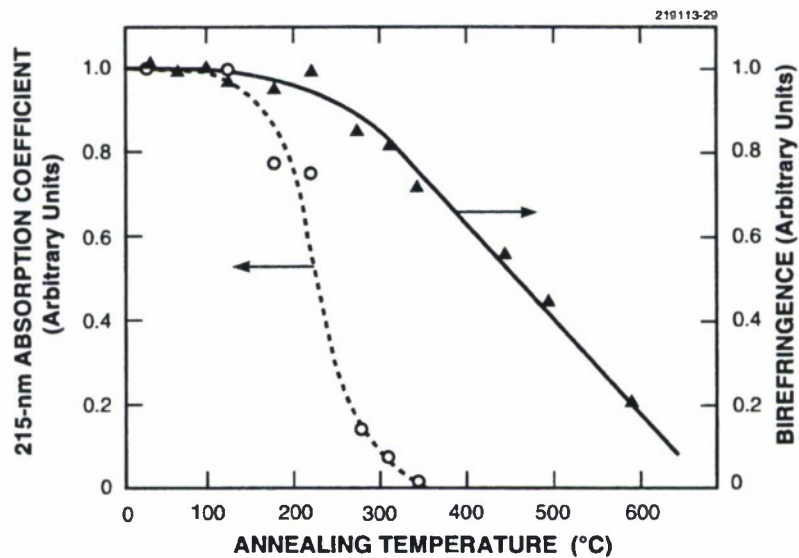


Figure 4-2. Annealing behavior of 193-nm-induced color centers (left-hand ordinate) and birefringence (right-hand ordinate) in Suprasil 2. The irradiation was performed at room temperature. The two ordinates were normalized to their respective values after exposure and prior to heating.

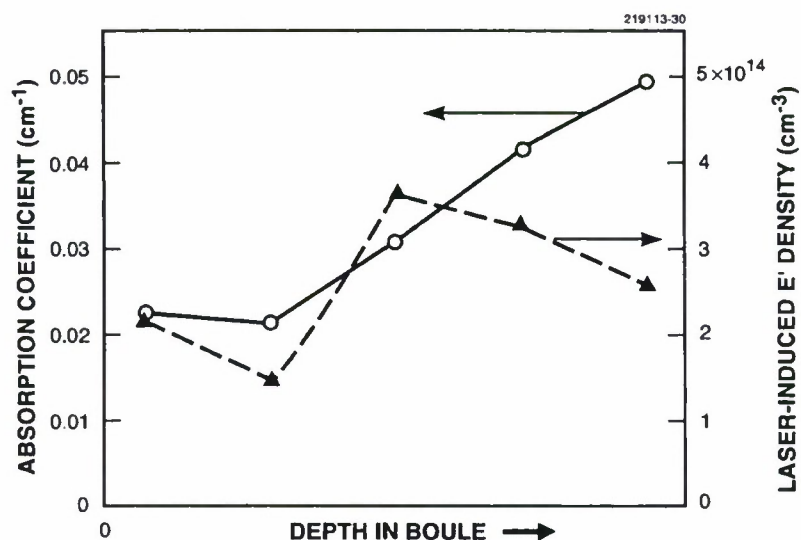


Figure 4-3. Pre-irradiation absorption coefficient at 193 nm of standard Corning 7940, as a function of the sample's location in the boule (left-hand ordinate). The broken line represents the density of laser-induced color centers generated by  $2 \times 10^6$  pulses at  $50 \text{ mJ cm}^{-2}/\text{pulse}$  in the same samples (right-hand ordinate). While the top of the boule is more transparent and more damage resistant, there does not seem to be a one-to-one correlation between initial absorption and amount of color center formation.

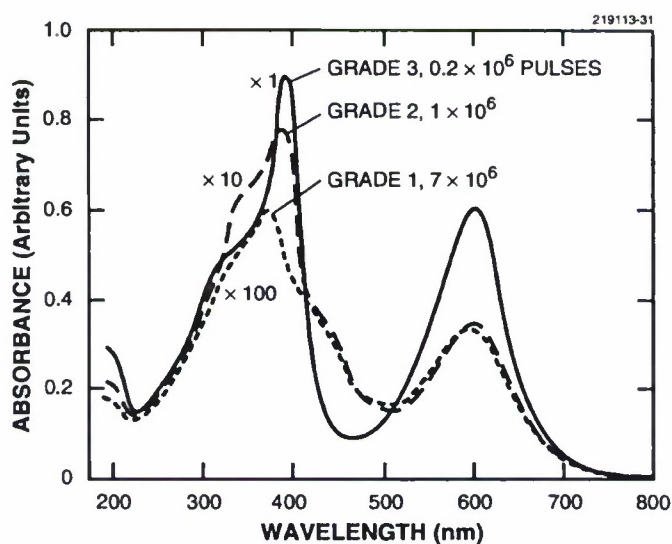


Figure 4-4. Color centers induced in  $\text{CaF}_2$  with a 193-nm laser at a fluence of  $100 \text{ mJ cm}^{-2}/\text{pulse}$ . The three grades form color centers at rates differing by 2 orders of magnitude, as shown by the scaling factors next to the curves and the number of pulses required to obtain each curve.



Among the fluorides listed above, calcium fluoride is the most promising all-purpose material. Its index of refraction at 193 nm is lower than that of fused silica, and therefore the availability of high-quality  $\text{CaF}_2$  would enable the design and fabrication of mixed  $\text{SiO}_2/\text{CaF}_2$  optical systems with a wider performance range than that of systems built of  $\text{SiO}_2$  alone. At shorter wavelengths, such as 157 nm, where  $\text{SiO}_2$  is opaque,  $\text{CaF}_2$  would be the optical material of choice. The index homogeneity of high-quality  $\text{CaF}_2$  has been measured to be in the 2–5-ppm range, and its absorption coefficient at 193 nm is  $< 0.01 \text{ cm}^{-1}$ . Irradiation at 193 nm can, however, cause formation of absorptive color centers, with peaks in the UV and visible. The laser-induced absorbance increases rapidly in the first few hundred thousand pulses, and then it typically exhibits strong saturation. It appears that in  $\text{CaF}_2$ , unlike in  $\text{SiO}_2$ , the excimer-induced color centers are formed via preexisting defects and that impurities may play a critical role in the process. Figure 4-4 shows absorption spectra generated in three different grades of  $\text{CaF}_2$ . Their magnitude varies by orders of magnitude, indicating that the purity of the raw materials and the details of the crystal growth process are important determinants of susceptibility to laser-induced damage.

M. Rothschild  
J. H. C. Sedlacek

## 4.2 HIGH-CONDUCTANCE, LOW-LEAKAGE DIAMOND SCHOTTKY DIODES

Diamond's high breakdown field ( $5 \text{ to } 10 \times 10^6 \text{ V cm}^{-1}$ ) [7] and wide bandgap should make possible high-voltage, high-temperature diodes that exhibit high conductance with low reverse leakage. Although several groups have fabricated diamond Schottky diodes [8]–[12] that have operated up to  $700^\circ\text{C}$  [10], most diamond diodes suffer from both high reverse leakage currents and low forward conductance. High-resistance ohmic contacts to the back of the diamond substrate were once thought responsible for the low forward conductance, but even with low-resistance ohmic contacts the diode's forward conductance is still below that predicted by theory. This report describes the use of Schottky diodes to characterize the electrical properties of diamond as a function of surface treatment and annealing. Improved diamond Schottky diodes were fabricated.

Schottky diodes were formed of Al, Au, and Hg on natural, boron-doped, *p*-type, IIb diamonds that were cut and polished to within  $3^\circ$  of either the (100) or the (111) plane. The Al diodes were fabricated by using standard lithographic techniques and wet chemical etching to pattern  $\sim 1 \text{ }\mu\text{m}$  of Al by electron-beam evaporation on cleaned [13] diamond substrates, the Au diodes by depositing Au through a stencil mask by ion-assisted deposition, and the Hg diodes by dropping Hg onto the diamond with a micropipet to form an  $\sim 300\text{-}\mu\text{m}$ -diam contact. In all three cases, back side ohmic contacts consisted of electron-beam-evaporated Al, annealed in air at temperatures  $> 500^\circ\text{C}$  and then contacted with silver paint. These ohmic contacts were of sufficiently low contact resistance that Schottky diode capacitance measurements were nearly independent of frequency from 0.05 Hz to 1 MHz and of temperature from  $-25$  to  $125^\circ\text{C}$ .

The surface electrical properties of diamond were characterized by measuring the reverse-bias leakage current of Al Schottky diodes after exposure to a plasma formed from one of several gases,

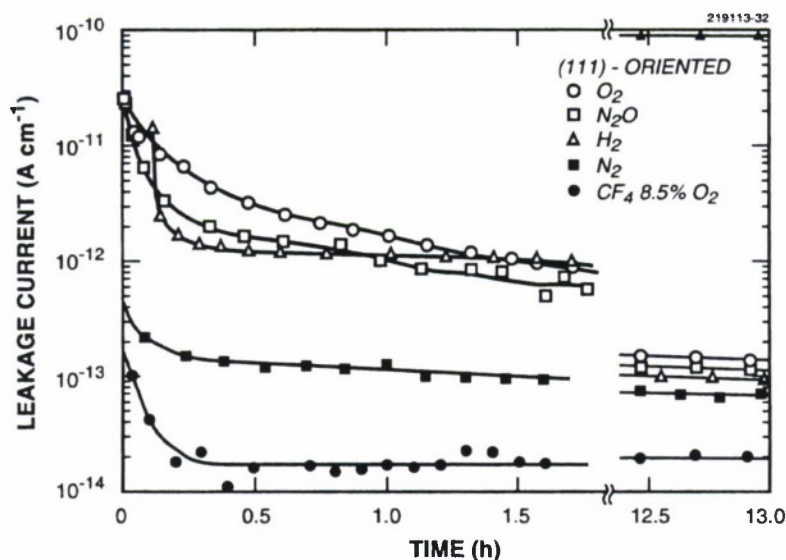


Figure 4-5. Leakage currents for  $20 \times 500\text{-}\mu\text{m}$  Al Schottky diodes fabricated on (111)-oriented substrate, for several plasma treatments. In this plot the measured currents were divided by the perimeter of the diodes.

including  $\text{N}_2$ ,  $\text{CF}_4$  with 8.5%  $\text{O}_2$ ,  $\text{O}_2$ ,  $\text{H}_2$ , and  $\text{N}_2\text{O}$ . The diodes were subjected to the plasma for 2 min, at  $\sim 0.5$  Torr, in a quartz tube, using 100 W of 13.5-MHz RF power. Nitrogen,  $\text{CF}_4$  with 8.5%  $\text{O}_2$ , and  $\text{O}_2$  were found by Auger analysis to chemically bind N, F, and O to the diamond surface, respectively. The plasma formed from  $\text{H}_2$  is believed to bind H to the surface [14], and the surface chemistry after a  $\text{N}_2\text{O}$  plasma is unknown. The N-, F-, and O-covered surfaces were stable in air with the surface atoms consistent with the last plasma treatment. No measurable diamond etching ( $< 20$  nm) occurred after repeated plasma exposures to these various gases.

Reverse leakage currents in air after treatment with various plasma gases are shown in Figure 4-5. Diodes exposed to plasmas of  $\text{O}_2$ ,  $\text{N}_2\text{O}$ , and  $\text{H}_2$  exhibited a leakage current, which decreased over several hours. The diode capacitance was unaffected by the plasma treatments, indicating that the bulk acceptor concentration remained constant during these experiments. Surface metal contacts located on the diamond  $\sim 20\text{ }\mu\text{m}$  from the reverse-biased Schottky diode intercept the reverse leakage current, showing that most of the leakage is due to surface conduction.

To determine the effect of various treatments on the diamond directly under the contacts, Hg Schottky diodes were used. After each treatment the diamond was characterized with a new Hg-drop Schottky diode, after which the Hg was removed by cleaning [13]. The most dramatic effect was the near-surface compensation of boron atoms. When the diamond is subjected to a plasma formed from either

$N_2$  or  $CF_4$  with 8.5%  $O_2$ , to low-energy ion beams, or to physical polishing, the subsurface boron acceptors become compensated to a depth from 10 to 1000 nm. The depth of this compensation can be determined by plotting the inverse of the diode capacitance squared as a function of bias voltage. This plot does not take the form of a straight line that can be extrapolated through the Schottky barrier height but instead exhibits a step near the Schottky barrier-height voltage,  $\sim 2$  V. An example of such a plot for an ion-beam-etched substrate [15] is shown in Figure 4-6. The depth of compensation  $X$  is estimated from

$$X = A\epsilon_s/C \quad , \quad (4.1)$$

where  $A$  is the diode area,  $\epsilon_s$  is the permittivity of diamond, and  $C$  is the Schottky diode capacitance at the barrier-height voltage.

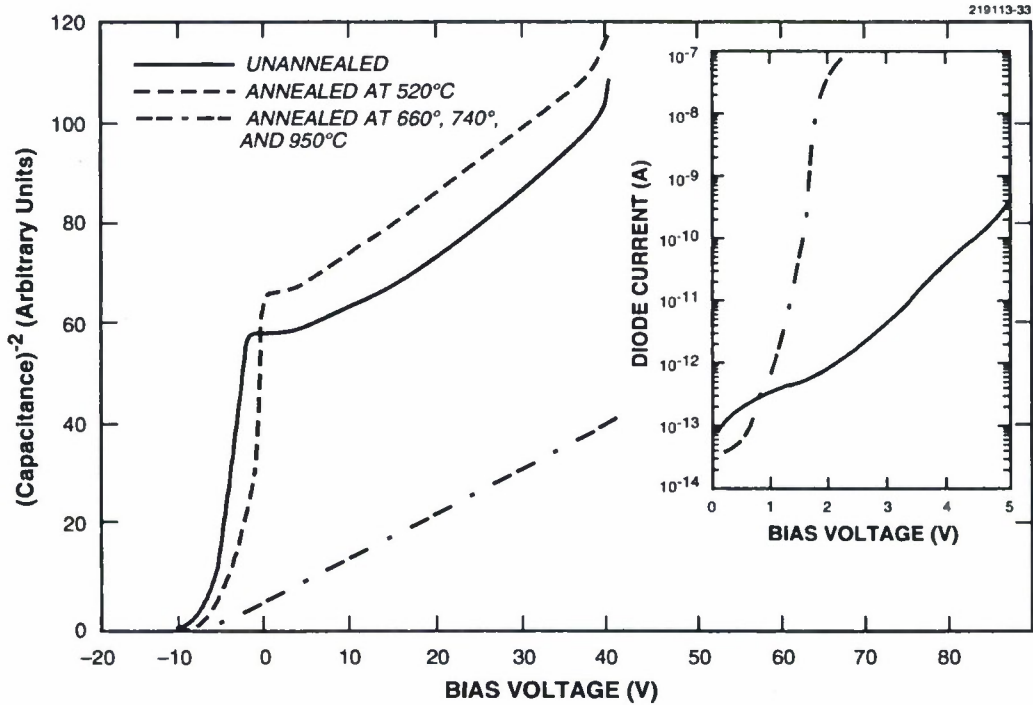


Figure 4-6. Inverse of a Hg Schottky diode capacitance squared as a function of bias voltage, for several annealing temperatures. The inset compares the current-voltage characteristics of the forward-biased Hg Schottky diodes before and after annealing at 660°C for 2 s. Before fabricating the diode, this diamond substrate was etched using ion-beam-assisted etching, to a depth of  $\sim 1 \mu m$ , with a 0.1-mA ion beam composed of 500-eV  $Xe^+$  in the presence of  $NO_2$ . This etching was used to form a 1.2- $\mu m$ -thick compensated layer.

The compensated region was characterized by subjecting the Hg Schottky diode to 40-V reverse bias for several days and to visible and bandgap UV radiation. This changes the slope of the straight line portion in Figure 4-6, as previously discussed by Lightowers and Collins [9], but the step in the curve near the barrier height remains unaffected. This indicates that the compensated region is not influenced by either extended periods of time at large electric fields ( $> 10^5 \text{ V cm}^{-1}$ ) or optical radiation.

This compensated layer can be removed by heating the diamond in air on a graphite strip heater to  $660^\circ\text{C}$  for 2 s, as shown in Figure 4-6. This heat treatment, which anneals away  $\sim 1 \mu\text{m}$  of compensation, is expected to remove only  $\sim 10 \text{ nm}$  of the diamond surface by oxidation. Additional heat treatments to  $900^\circ\text{C}$ , which cause pitting of the diamond surface, result in no additional changes in the capacitance-voltage curves. Removing the compensated layer increases the forward-bias conductance of Hg Schottky diodes, and this improves the  $n$ -factor of the diode. An ideal diode would have an  $n$ -factor equal to 1, and values  $> 1$  represent an exponential decrease in the diode's conductance. The inset of Figure 4-6 compares the current-voltage (I-V) characteristics of the same substrate before and after annealing at  $660^\circ\text{C}$ . Before annealing the  $n$ -factor of the diode is  $\sim 20$ , while after annealing it is 1.9. We have obtained some of the lowest reported  $n$ -factors, 2 to 1.3, with this annealing technique. Although the Hg was removed before annealing, in other experiments with Au Schottky diodes the compensation was annealed away with the Au in place and similar results were achieved.

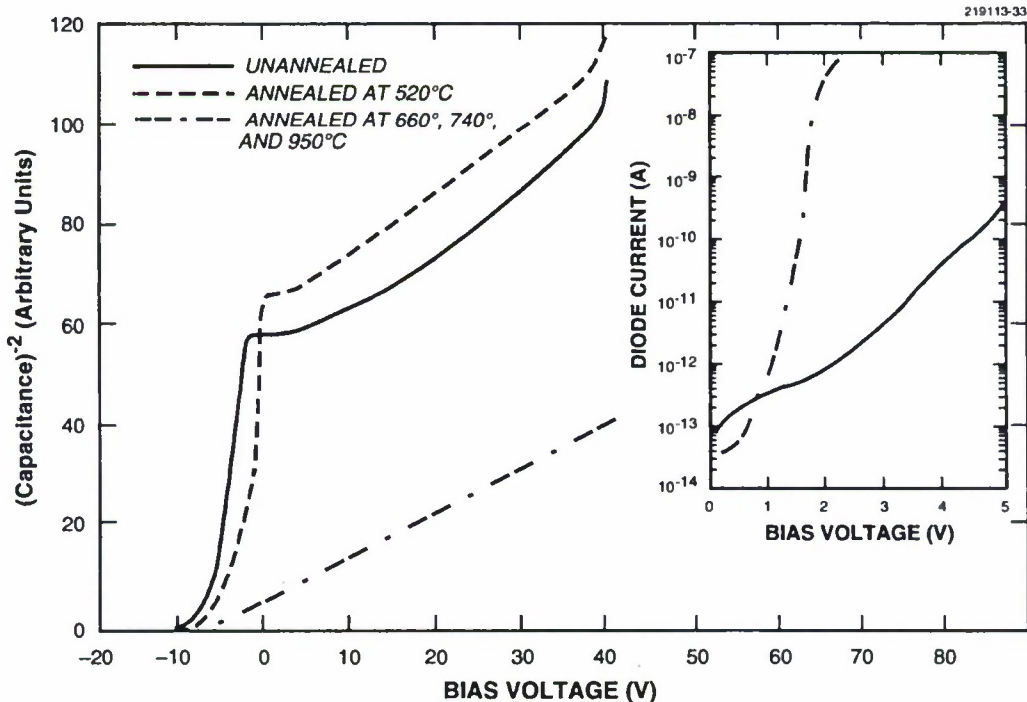


Figure 4-7. Current-voltage curve of a diamond-Hg Schottky diode at  $110^\circ\text{C}$  and for comparison a Pt-PtSi-Si Schottky diode at  $25^\circ\text{C}$ .



Once the surface leakage has been minimized with a plasma treatment and any subsurface compensation layer has been removed, high-quality Schottky diamond diodes can be fabricated. Figure 4-7 shows the I-V curve of a Hg Schottky diode at 110°C in dry nitrogen. The diamond substrate was heated to 660°C to remove the compensation and then plasma treated with a gas mixture of He, CF<sub>4</sub>, and O<sub>2</sub> that was found to passivate the diamond surface while not forming a measurable compensated region. Each data point in Figure 4-7 is the average of 200 individual current measurements taken over a period of ~ 10 min. These diodes have the lowest reverse leakage currents reported for any Schottky diode and the highest forward conductance of any diamond diode.

M. W. Geis  
N. N. Efremow  
J. A. von Windheim\*

## REFERENCES

1. M. Rothschild, D. J. Ehrlich, and D. C. Shaver, *Appl. Phys. Lett.* **55**, 1276 (1989).
2. W. P. Leung, M. Kulkarni, D. Krajnovich, and A. C. Tam, *Appl. Phys. Lett.* **58**, 551 (1991).
3. R. A. Weeks and E. Sonder, in *Paramagnetic Resonance*, W. Low, ed. (Academic, New York, 1963), Vol. 2, p. 869.
4. T. E. Tsai, D. L. Griscom, and E. J. Friebele, *Phys. Rev. B* **40**, 6374 (1989).
5. R. K. Brimacombe, R. S. Taylor, and K. E. Leopold, *J. Appl. Phys.* **66**, 4035 (1989).
6. T. E. Tsai and D. L. Griscom, *Phys. Rev. Lett.* **67**, 2517 (1991).
7. V. K. Bazhenov, I. M. Vilkulin, and A. G. Gontar, *Sov. Phys. Semicond.* **19**, 829 (1985).
8. G. H. Glover, *Solid-State Electron.* **16**, 973 (1973).
9. E. C. Lightowers and A. L. Collins, *J. Phys. D* **9**, 951 (1976).
10. M. W. Geis, D. D. Rathman, D. J. Ehrlich, R. A. Murphy, and W. T. Lindley, *IEEE Electron Device Lett.* **EDL-8**, 341 (1987).
11. G. Sh. Gildenblat, S. A. Grot, C. R. Wronski, and A. R. Badzian, *Proc. IEEE* **79**, 647 (1991).
12. T. Tachibana, B. E. Williams, and J. T. Glass, *Phys. Rev. B* **42**, 11972 (1992).
13. M. W. Geis, J. A. Gregory, and B. B. Pate, *IEEE Trans. Electron Devices* **38**, 619 (1991).
14. B. B. Pate, *Surf. Sci.* **165**, 83 (1986).
15. N. N. Efremow, M. W. Geis, D. C. Flanders, G. A. Lincoln, and N. P. Economou, *J. Vac. Sci. Technol. B* **3**, 416 (1985).

---

\*Author not at Lincoln Laboratory.



## 5. HIGH SPEED ELECTRONICS

### 5.1 DETECTION OF NANOSECOND FAR-INFRARED PULSES AT CRYOGENIC TEMPERATURES USING MULTIPLE-QUANTUM-WELL STRUCTURES

Measurements of the fast photoconductive response by a lightly doped multiple-quantum-well (MQW) sample have been made at temperatures between 10 and 90 K using ultrashort far-infrared superradiant pulses and compared to measurements obtained using a conventional corner-cube-mounted Schottky diode detector [1]. The sample consisted of fifty 28-nm-wide quantum wells separated by 30-nm-wide  $\text{Al}_{0.30}\text{Ga}_{0.70}\text{As}$  barriers with only the middle third of each quantum well intentionally doped, this doping being *n*-type at a level of  $3 \times 10^{15} \text{ cm}^{-3}$ . Details of the sample-contact scheme have been described elsewhere [2]. The noise level at high frequencies ( $> 1 \text{ MHz}$ ) and responsivity of the detector system near 10 K are estimated to be  $10 \text{ nV/Hz}^{1/2}$  and  $10^{-1} \text{ V/W}$ , respectively.

The responses at 10 K of the MQW and Schottky diode detectors to separate but closely spaced  $292\text{-}\mu\text{m}$ -wavelength, ultrashort, superradiant pulses are shown in Figures 5-1(a) and 5-1(b), respectively. The measured rise time of the MQW system is 2.6 ns. The Schottky detector, which is known to be sufficiently fast to measure the true pulse shape, gives a pulse rise time of 1.7 ns and a pulse width of 2.6 ns. The true response time of the MQW detector at  $T \approx 10 \text{ K}$  is  $\tau_R = 2 \text{ ns}$ , assuming  $\tau_R^2(\text{system}) = \tau_R^2(\text{pulse}) + \tau_R^2(\text{detector})$ . Here,  $\tau_R$  is defined as the time interval between occurrence of the 10 and 90% values of the detector peak response. The sign of the voltage signal was opposite to that of the applied dc voltage, indicating a *positive* photoresponse, i.e., the MQW sample's conductivity has increased during illumination.

A response measurement was also carried out at  $\sim 90 \text{ K}$  using the same superradiant pulse conditions described for Figure 5-1. The result is shown in Figure 5-2 and demonstrates that the MQW detector is able to respond as fast as the Schottky diode detector to nanosecond far-infrared pulses. The responsivity of the MQW detector, when compared with that near 10 K, is down by approximately 3 orders of magnitude. However,  $\tau_R$  has decreased with increasing temperature. Consequently, there is no discernible difference between the pulse shape as measured by the Schottky and MQW detector, implying a subnanosecond response time for the latter.

The detector response to CW radiation at  $T \approx 10 \text{ K}$  was measured at the following far-infrared wavelengths: 117.7, 134.0, 158.5, 191.8, 214.5, 287.7, 570.6, 662.8, and  $890.0 \mu\text{m}$ . The power ranged from 3.4 mW to  $70 \mu\text{W}$ . As seen in Figure 5-3, the MQW detector shows a trend of increasing responsivity with wavelength. Based on our previous MQW work [3],[4], the small peak in Figure 5-3 between 150 and  $225 \mu\text{m}$  may be due to the  $1s \rightarrow 2p$  electronic impurity transition in the GaAs quantum wells. The low frequency noise level is estimated to be  $10 \mu\text{V/Hz}^{1/2}$ . The uncertainty in the data point at  $890.0 \mu\text{m}$  is quite large owing to the difficulty of measuring low power levels ( $< 100 \mu\text{V}$ ) at long wavelengths.

Absorption of far-infrared radiation by free electrons can produce a positive photoconductive response by means of the hot-electron effect [5], a process well understood [6] and successfully applied to far-infrared detection in InSb [7]. Based on the results described above, we attribute the observed detector

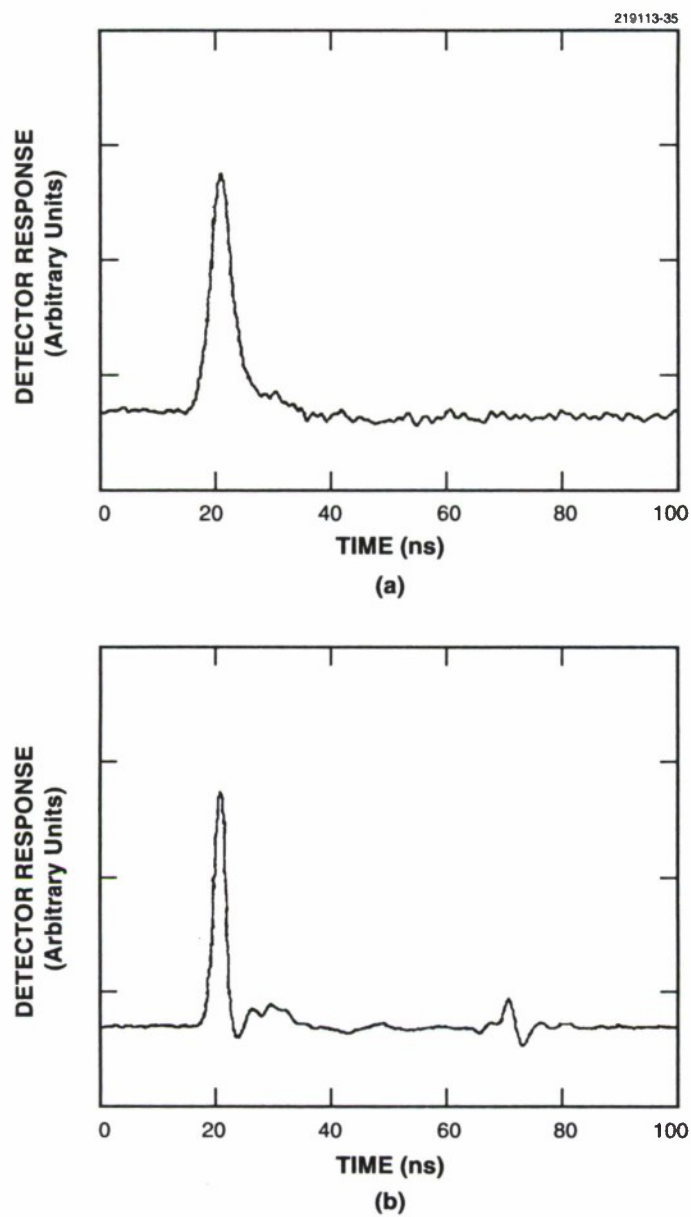


Figure 5-1. Response at  $T = 10\text{ K}$  to 2.6-ns-wide, 292- $\mu\text{m}$ -wavelength superradiant pulses for (a) a multiple-quantum-well (MQW) detector and (b) a Schottky diode. Source configuration:  $\text{CO}_2$  pulse energy before plasma shutter, 150 mJ; plasma shutter,  $p = 50\text{ Torr}$ ;  $\text{NH}_3$ ,  $p = 0.60\text{ Torr}$ .

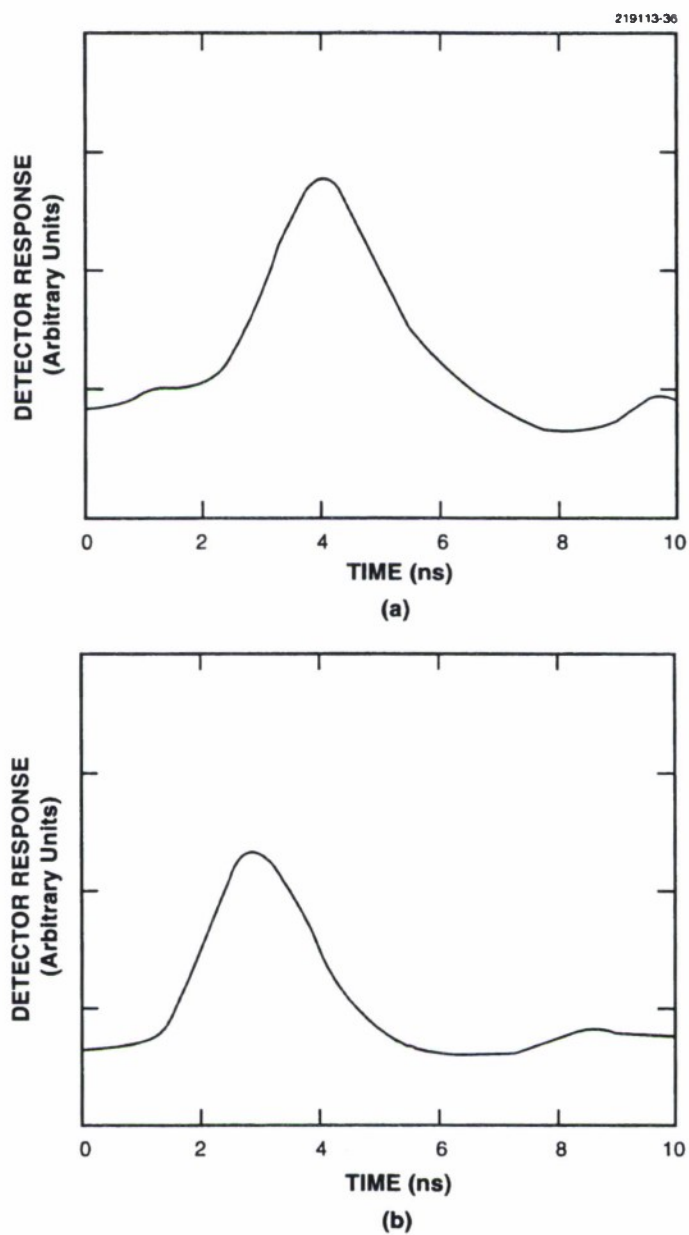


Figure 5-2. Response at  $T = 90$  K to 2.6-ns-wide, 292- $\mu\text{m}$ -wavelength superradiant pulses for (a) an MQW detector and (b) a Schottky diode. The source configuration is the same as in Figure 5-1.

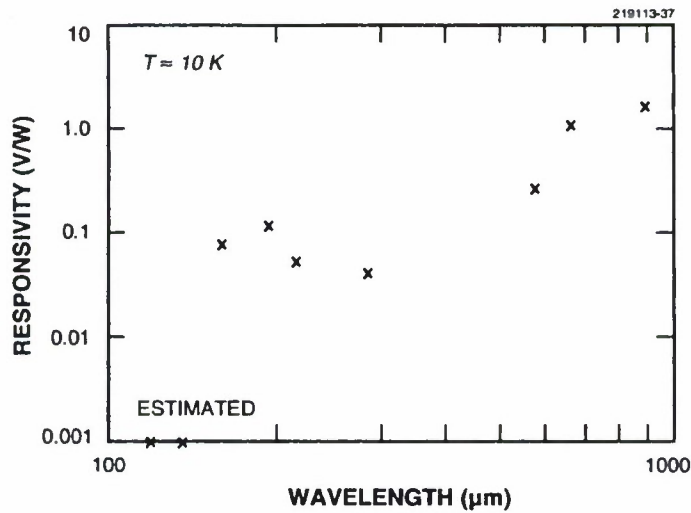


Figure 5-3. Responsivity as a function of wavelength for the MQW sample at  $T \approx 10$  K. The CW laser was chopped at 200 Hz.

response to hot-electron conductivity in GaAs quantum wells. A similar conclusion was reached by Rosencher et al. [8] from the observation of normal-incidence, positive photoconductive response at  $10.6 \mu\text{m}$  using a GaAs/(Ga,Al)As MQW sample with 6-nm-wide Si-doped wells. These authors also report a peak photoconductive response at low temperature ( $T = 15$  K), an order-of-magnitude reduction in sensitivity at 77 K, and continued detection up to 200 K. Given the early stage of this effort, considerable promise exists for developing a relatively sensitive far-infrared photodetector capable of operating at liquid-nitrogen temperature with subnanosecond speed. Such a detector would be much more rugged than the present corner-cube-mounted, whisker-contacted, GaAs Schottky barrier diode and would thus be able to operate in severe electrical and mechanical environments.

J. Waldman*	W. D. Goodhue
E. R. Mueller*	D. B. Moix*
E. S. Jacobs*	D. P. Scherrer*
M. J. Coulombe*	F. K. Kneubuhl*

---

\*Author not at Lincoln Laboratory.

## REFERENCES

1. J. Waldman, D. B. Moix, D. P. Scherrer, F. K. Kneubühl, W. D. Goodhue, E. R. Mueller, and M. J. Coulombe, *Infrared Phys.* **33**, 487 (1992).
2. E. R. Mueller, W. D. Goodhue, D. M. Larsen, J. W. Bales, and J. Waldman, *Phys. Rev. B* **44**, 1754 (1991).
3. E. R. Mueller, Ph.D. thesis, University of Massachusetts Lowell, 1992.
4. R. T. Grimes, M. B. Stanaway, J. M. Chamberlain, J. L. Dunn, M. Henini, O. H. Hughes, and G. Hill, *Semicond. Sci. Technol.* **5**, 306 (1990).
5. B. V. Rollin, *Proc. Phys. Soc. London* **77**, 1102 (1961).
6. S. M. Kogan, *Sov. Phys. Solid State* **4**, 1396 (1963).
7. E. H. Putley, in *Semiconductors and Semimetals*, R. W. Willardson and A. C. Beer, eds., Vol. 12 (Academic, New York, 1977), p. 143.
8. E. Rosencher, E. Martinet, E. Böckenhoff, Ph. Bois, S. Delaitre, and J. P. Hirtz, *Appl. Phys. Lett.* **58**, 2589 (1991).



## 6. MICROELECTRONICS

### 6.1 IMPROVED ULTRAVIOLET RESPONSE OF SILICON CCD IMAGERS

Front-illuminated charge-coupled-device (CCD) imagers have demonstrated excellent performance in the visible and near-infrared portions of the spectrum. However, losses due to optical absorption in the polysilicon CCD gates cause moderate degradation of quantum efficiency in the visible and severe degradation in the blue and ultraviolet (UV). A number of laboratories have utilized a back-illuminated configuration to avoid these losses [1],[2]. We have developed and report here an improved process for back-illuminated CCD imagers that provides near-reflection-limited UV quantum efficiency together with excellent stability under UV exposure.

The processing sequence begins with use of wet chemistry to thin a silicon wafer, containing CCD imagers [3], to a thickness of 10–20  $\mu\text{m}$ . An oxide is grown on the back surface, and boron is implanted at a low energy followed by annealing in a conventional furnace. The thinned wafer is mounted with the back surface exposed and is patterned so that contact can be made to the Al bonding pads using a process similar to that described in Ref. 4.

The photoresponse of back-illuminated CCD imagers produced with this process is shown in Figure 6-1. Here the external quantum efficiency at  $-50^\circ\text{C}$  is plotted for two such devices (635-5 and 609-5). Device 635-5 was fabricated on a bulk silicon wafer with resistivity exceeding 6000  $\Omega\text{ cm}$ , and device 609-5 was formed on a 40- $\Omega\text{ cm}$  epitaxial silicon wafer in a different wafer lot. Despite these differences, it is seen that the results from these two devices agree very well and closely approach the calculated reflection-limited response shown as the dashed curve on this figure. The theoretical curve has been calculated assuming more than one electron-hole pair may be generated by each absorbed photon for part of this wavelength range [5]. Also shown in Figure 6-1 is the calculated quantum efficiency of sample 171-1, which was fabricated using an earlier laser anneal process [4]. The measured quantum efficiency of this device has been revised to include a hypothetical  $\text{SiO}_2$  antireflective coating. It is apparent that the oxide-coated devices (635-5 and 609-5) show an improvement in response beyond that resulting from the antireflective properties of the thin layer of  $\text{SiO}_2$ . At wavelengths  $> 390\text{ nm}$ , the experimental results exceed the theoretical limits, probably because of a measurement calibration error on the order of 5–10%.

There is an additional benefit from use of the high-quality thermal oxide, believed to be due to suppression of surface states. In Figure 6-2, the two sets of results from Figure 6-1 for the current process are plotted together with data from 645-5, which was made by implanting  $\text{BF}_2$  into bare Si and annealing in a conventional furnace. The addition of  $\text{SiO}_2$  to the devices made on bare Si would be expected to result in an improvement of their quantum efficiency by a factor of 1.7, because of the antireflection properties of this layer. However, the actual improvement is by a factor of  $\sim 2.3$ . Therefore, it appears that in addition to acting as an antireflective layer, the high-quality thermally grown oxide layer may also increase quantum efficiency by suppressing surface states and thereby decreasing the surface recombination velocity. The oxide-coated devices also had lower dark currents (15–30 electrons/pixel-second at  $-50^\circ\text{C}$ ) than the uncoated device 645-5 (70 electrons/pixel-second), which is consistent with the hypothesis that the devices coated with thermal oxide have lower levels of generation-recombination centers at

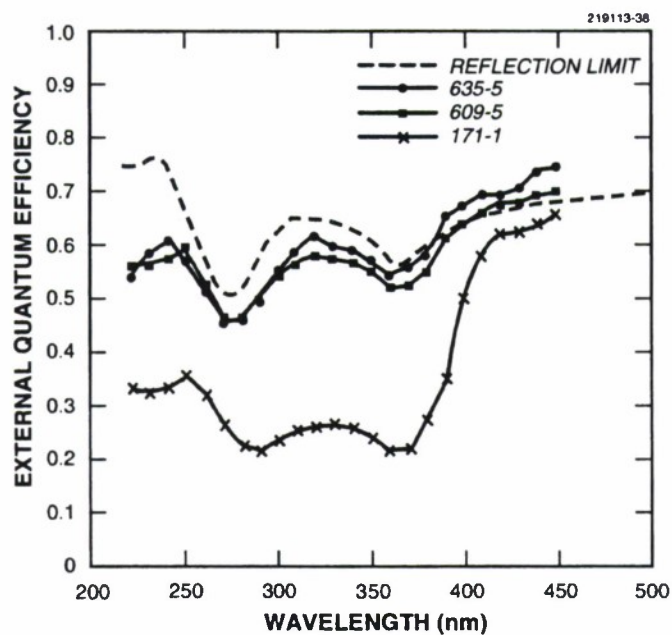


Figure 6-1. Calculated (curves) and measured (points) external quantum efficiency of back-illuminated charge-coupled device (CCD) imagers.

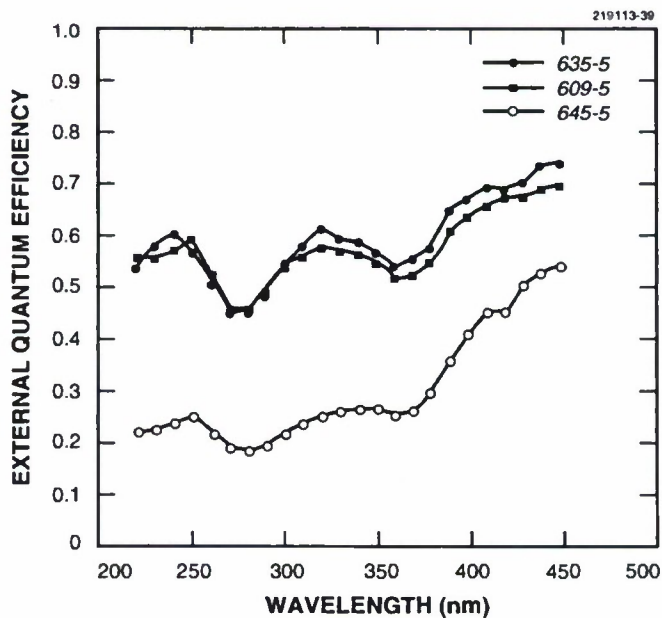


Figure 6-2. Effect of SiO<sub>2</sub> layers on quantum efficiency.

the back surface. Further, measurements made by monitoring external quantum efficiency vs time at  $-50^{\circ}\text{C}$  and 250-nm wavelength indicate that the oxide-coated devices are stable to  $\pm 2\%$  over 1–2 h, while device 645-5 can change in quantum efficiency by as much as a factor of 2 in the same time. This instability may be due to a negative charging of the more plentiful surface states of the device not incorporating a thermal oxide layer.

J. A. Gregory      B. E. Burke  
A. H. Loomis      H. R. Clark

## 6.2 EPITAXIAL SILICON JFET AMPLIFIER FOR LOW-NOISE CHARGE DETECTION

Ultimate low-light-level image sensing requires detectors that can sense single-photon events. To this end, solid state detector arrays have been fabricated that have near-reflection-limited quantum efficiencies [4]. However, the conversion process of the photoelectron signal into a usable output voltage or current is noisy and has generally restricted these devices to sensing relatively large charge packets or operating at low output frequencies. Here, we describe the initial development of a *p*-channel junction field-effect transistor (JFET) fabricated in an epitaxially grown silicon layer. It is designed to sense as small as a single electron charge packet at relatively high clock frequencies.

Figure 6-3 shows the cross section and top view of the JFET structure. The JFET device is compatible with conventional buried-channel CCD processing, but changes are required in the standard sequence after the thermal oxidation of the second polysilicon layer. Instead of depositing a third layer of polysilicon, the silicon substrate is exposed selectively in regions formed between the two previously deposited polysilicon layers. Single-crystal epitaxial silicon is then grown at these seed hole areas, while polysilicon is simultaneously deposited on the adjacent thermal oxide. The drain and source areas of the JFET are created in the epitaxial regions by a subsequent masked boron implantation. The *p*-channel JFET is finished by implanting arsenic to form the back gate of the transistor.

Transistor performance was estimated using the device simulator PISCES, which solves the Poisson and continuity equations. A charge-to-voltage gain (responsivity) of  $160\ \mu\text{V}/e$  was calculated from the simulations. This value is about a factor of 10 better than conventional low-noise charge-sense amplifiers. The noise of the *p*-channel transistor can be estimated using PISCES, assuming that the device is thermal noise limited. This is a reasonable assumption for a *p*-channel JFET, since the measured  $1/f$  noise contribution of a conventional buried-channel MOSFET is low for bandwidths greater than a few megahertz and is expected to be even lower for the JFET [6],[7]. The noise value calculated from PISCES for a 10-MHz bandwidth is  $\sim 0.6$  noise equivalent electrons, assuming the load device is a current source. Because of its high responsivity, the *p*-channel JFET provides a higher output voltage for a given electron signal than conventional charge-sense structures. The increased voltage signal relative to the transistor noise voltage enables detection of small charge packets.

Figure 6-4 shows an operating scheme for detecting photoelectrons with the JFET amplifier. Photocarriers generated by an image are collected by a positively biased electrode  $\phi 1$ . After an integration period, the photocarriers are transferred under the *p*-channel JFET by lowering the bias potential. The



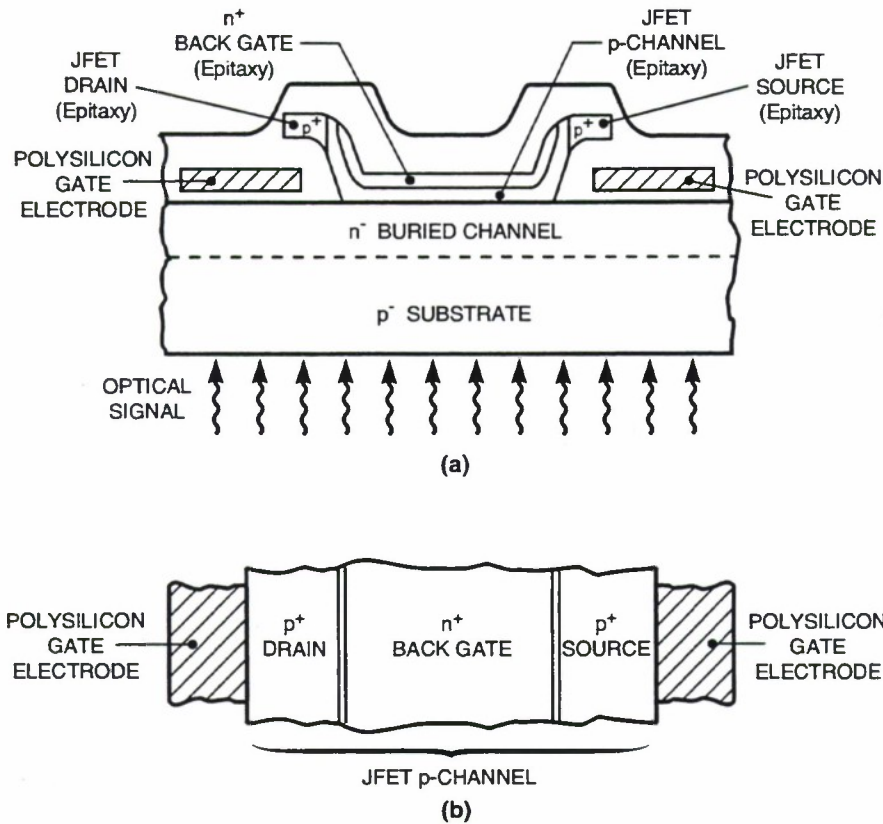


Figure 6-3. (a) Cross section and (b) top view of p-channel charge-sense amplifier as implemented in a conventional three-phase buried-channel CCD process.

photocarriers, in this case electrons, modulate the channel resistance of the JFET, which in turn causes a change in voltage across some load device (either a resistor or current source). The load device is located outside the imaging area and is connected to the source of the JFET by a conductive line. The voltage change constitutes the output signal.

The critical development component of the JFET is the epitaxially grown silicon layer. The single crystalline region of this layer must be defect-free to minimize the generation-recombination leakage current in the JFET device. Epitaxial diode test structures have been fabricated using both conventional chemical vapor epitaxy and also molecular beam epitaxy. The diode leakage current was measured on devices that had areas ranging from  $100 \times 100$  to  $1000 \times 1000 \mu\text{m}$ . All of the diodes measured showed decreasing current with area. However, the  $1000 \times 1000\text{-}\mu\text{m}$  structures did have some randomly occurring sites with relatively high leakage current. The lowest leakage current density, measured on diode test structures fabricated using chemical vapor epitaxy, was  $\sim 1.5 \text{ nA/cm}^2$ . The goal is to achieve leakage

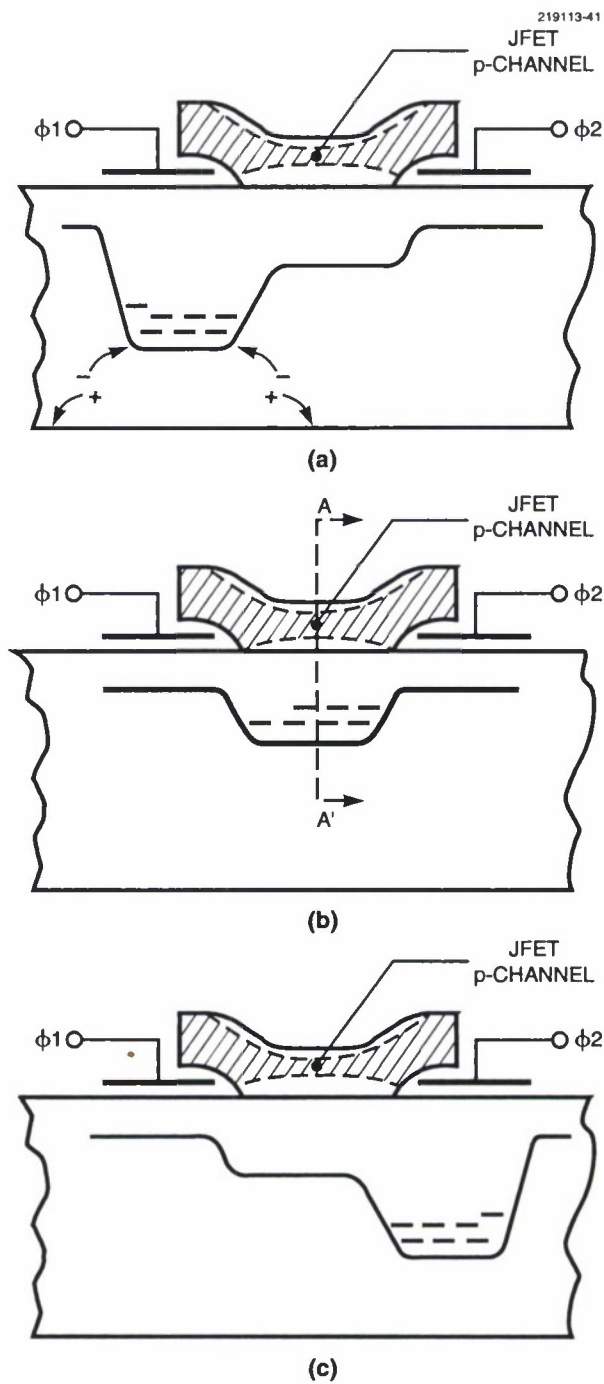


Figure 6-4. Operating sequence for detecting charge with the p-channel junction field-effect transistor amplifier: (a) image, (b) sense, and (c) reset.



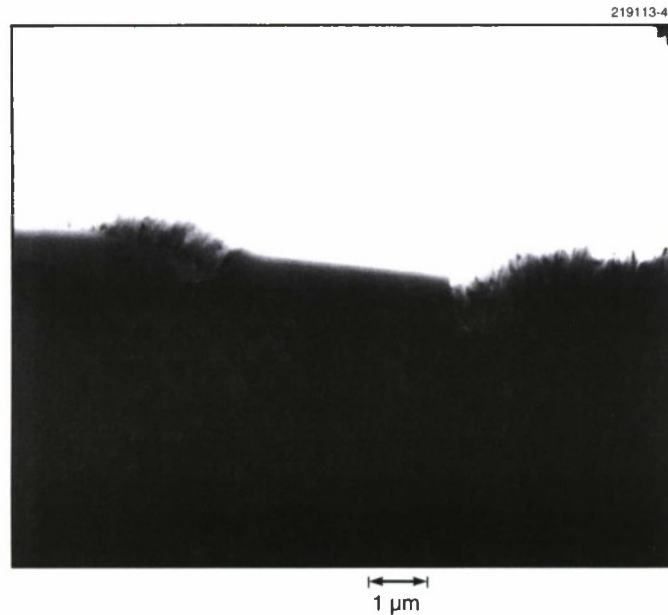


Figure 6-5. Transmission electron micrograph showing cross section of the epitaxial silicon layer that has been grown from seed holes in a thermal field oxide.

current densities  $< 1 \text{ nA/cm}^2$ , which is near the value in the imaging area of our current low-noise CCD solid state detectors [8]. Figure 6-5 shows a transmission electron micrograph (TEM) of the cross section of the epitaxial silicon test diodes. The interface between the silicon substrate and epitaxially grown silicon layer appears uniformly crystalline. Some of the TEM photographs showed defects near the field-oxide bird's-beak edge originating at the polysilicon layer. High leakage currents attributable to these defects were measured on larger-area diodes. Steps are now being taken to reduce the defects.

R. K. Reich  
R. W. Mountain  
B-Y. Tsaur

#### REFERENCES

1. C. M. Huang, B. B. Kosicki, J. R. Theriault, J. A. Gregory, B. E. Burke, B. W. Johnson, and E. T. Hurley, *Proc. SPIE* **1447**, 156 (1991).
2. M. E. Hoenk, P. J. Grunthaner, F. J. Grunthaner, R. W. Terhune, M. Fattahi, and H. F. Tseng, *Appl. Phys. Lett.* **61**, 1084 (1992).
3. B. E. Burke, J. A. Gregory, R. W. Mountain, J. C. M. Huang, M. J. Cooper, and V. S. Dolat, *Proc. SPIE* **1693**, 86 (1992).

4. C. M. Huang, B. E. Burke, B. B. Kosicki, R. W. Mountain, P. J. Daniels, D. C. Harrison, G. A. Lincoln, N. Usiak, M. A. Kaplan, and A. R. Forte, *IEEE Proc. Symp. on VLSI Technology Systems and Applications* (IEEE, New York, 1989), p. 98.
5. F. J. Wilkinson, A. J. D. Farmer, and J. Geist, *J. Appl. Phys.* **54**, 1172 (1983).
6. A. Van der Ziel, *Noise in Solid State Devices and Circuits* (Wiley, New York, 1986), p. 171.
7. V. Radeka, S. Rescia, P. F. Manfredi, and V. Speziala, *IEEE Trans. Nucl. Sci.* **38**, 83 (1991).
8. B. E. Burke and S. A. Gajar, *IEEE Trans. Electron Devices* **38**, 285 (1991).

## 7. ANALOG DEVICE TECHNOLOGY

### 7.1 VME-BUS-COMPATIBLE BOARD FOR AN IMAGE-FEATURE EXTRACTOR

A charge-coupled-device (CCD) programmable image processor, consisting of a 775-stage analog input buffer, 49 multipliers, and 49 8-bit 20-stage local memories, has been developed [1]. The 29-mm<sup>2</sup> chip performs two-dimensional filtering of a gray-level image with 20 programmable 8-bit  $7 \times 7$  spatial filters, and thus can be used as a multi-template two-dimensional far-infrared filter for signal conditioning such as noise reduction and for enhancing and/or skeletonizing an input image. The device can also be employed to detect features in the input image, and for this reason we call it an image-feature extractor (IFE). Better than 99.999% charge-transfer efficiency and  $> 42$ -dB dynamic range have been achieved by the device. At a 10-MHz clock rate, it performs one billion arithmetic operations per second and dissipates  $< 1$  W.

The CCD IFE device has been embedded on a board with a VME-bus interface. The VME bus is a standard computer backplane interface that uses specified protocols and has electrical and mechanical characteristics to enable communication with other devices connected to the same VME bus. A software program has also been developed that allows this VME board to be used as a high-speed co-processor with a host computer to speed up the simulations in various image and neural network applications.

The VME board has two parts: digital control electronics and CCD IFE analog control electronics. The digital control electronics, which is shown in Figure 7-1, provides all the buffering and controls required to transfer data to and from the CCD IFE. This part of the board consists of five functional blocks: a VME-bus interface, input image and feature template buffers, CCD output buffers, CCD timing-control buffers, and control and status registers. Sufficient memory buffering at both the input and output ports to the CCD has been included, so uninterrupted high-speed operations can be provided by the IFE even under different system and environment constraints. The VME board can be used to process input images of different sizes (up to 128 pixels wide), different reference templates (up to  $7 \times 7$  pixels), and different numbers of templates (up to 20). The flexibility is provided by changing the timing controls, which are in turn controlled by the software program. The analog control electronics, illustrated in Figure 7-2, provides metal oxide semiconductor level clocks to the IFE. In addition, hardware has been provided on this part of the board to control the output amplitude by scaling up or down in magnitude by a factor of 2.

An experiment was carried out to demonstrate the functionality of this VME board. The input/output format used is shown in Figure 7-3. In this test, the IFE is programmed to detect 20 oriented line segments in an input image containing two of the stored templates, 1 and 9. Figure 7-4 is the two-dimensional correlation output of the input image with template 9. The feature templates are shown at the top of Figure 7-4. The two correlation spikes indicate the autocorrelation of template 9 and the cross-correlation of template 1 with 9. The correlation outputs indicate that the input feature has been detected.

A. M. Chiang  
J. R. LaFranchise

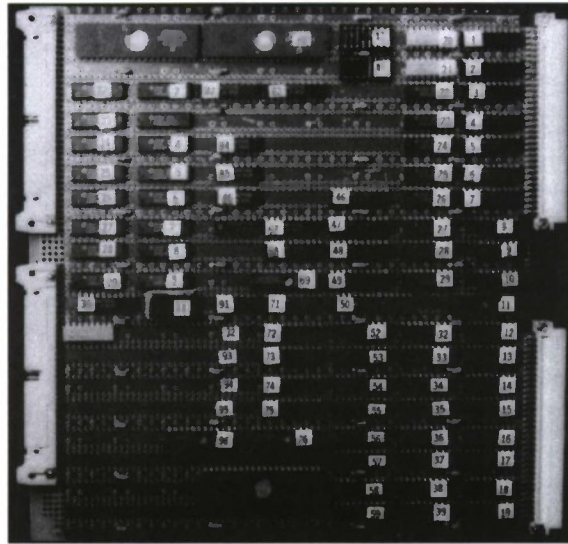


*Figure 7-1. Digital control board.*

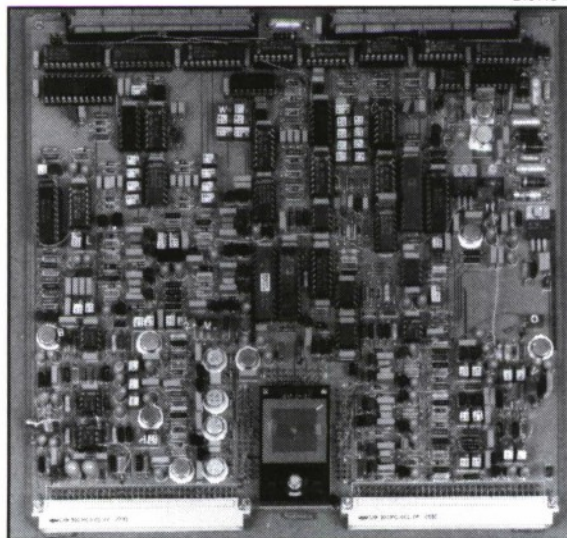


*Figure 7-2. Analog control board.*

219113-45

**IFE USER INTERFACE**

Template Count: 20

Template Size: COL: 7  ROW: 7

Template Filename: 20templates

Image Size: COL: 128  ROW: 128

Image Filename: t1andt9

Output Filename: correlation ▲

CCD GAIN CONTROL

\*\*\*\*\*

STATUS

Figure 7-3. Example of an input/output format for the charge-coupled device (CCD) image-feature-extractor (IFE) VME board.

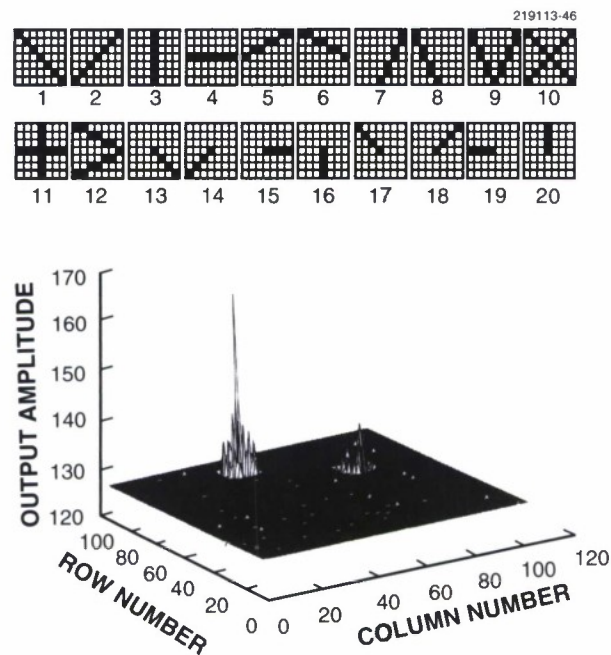


Figure 7-4. Output waveform of the CCD IFE VME board as a feature extractor. Shown at the top are feature templates.



## 7.2 DEMONSTRATION OF A PROTOTYPE HIGH- $T_c$ SUPERCONDUCTIVE WIDEBAND REAL-TIME SPECTRUM-ANALYSIS RECEIVER

Progress in conventional microwave electronics has produced a rapid increase in the use of the microwave frequency spectrum for many commercial and military applications, including global positioning, communications, and radar. High-temperature superconductors (HTSs) can provide passive microwave signal-processing devices with the multigigahertz bandwidths necessary to cover the many bands of interest [2]. An example of a demanding application is an electronic intelligence system that would gather information on microwave signals across very wide frequency bands. A real-time spectrum-analysis receiver can be used as a wideband cueing receiver in such a system. A cueing receiver determines the frequencies of received signals, and controls frequency-agile local oscillators and mixers to shift the intercepted signals into a band where they can be processed for information content by a narrowband receiver.

Demonstration prototypes of many of the passive HTS microwave devices and subsystems that would be used in such an electronic intelligence system have been produced and tested. These include narrowband filters [2], wideband delay lines [3], multigigahertz-bandwidth tapped-delay-line transversal filters [2], phased-array antenna feed networks [4], and chirp-transform spectrum-analysis subsystems [5]. Here we describe a spectrum-analysis receiver that is a prototype of the cueing receiver portion of the electronic intelligence system discussed above. This prototype cueing receiver is constructed using HTS chirp filters and the associated semiconductor circuits necessary for output signal processing. The semiconductor circuits are operated at room temperature in this case.

This spectrum-analysis receiver, also known as a compressive receiver, is based on the chirp-transform algorithm. The system is designed around a Hamming-weighted  $\text{YBa}_2\text{Cu}_3\text{O}_{7-x}$  (YBCO) superconductive chirp filter [6]. A simplified block diagram of the system is shown in Figure 7-5. A space-qualified version is being built by Lincoln Laboratory for incorporation into the Navy's Second High-Temperature Superconductor Space Experiment (HTSSE II). Signals input to the system are mixed with a chirp signal generated by a swept local oscillator (SLO). The four different frequencies shown in the plot of frequency (F) vs time (T) at the input in Figure 7-5 produce four frequency-offset upchirp signals. These frequency-offset chirps are input to a chirp filter with opposite chirp slope, i.e., the slope of the instantaneous frequency-vs-time characteristic differs in sign but not magnitude from the chirped signals. The compressed pulses generated by the chirp filter for each of the frequency-offset chirp signals will exit the filter at different times. The time of exit is proportional to the frequency of the original input signals.

ces. The best error-sidelobe-level performance of the VCO/YBCO chirp filter combination is about 18 dB. This level is determined solely by errors in the chirp slope of the VCO and not by device errors in the YBCO chirp filter. The envelope-detected compressed pulse and the ECL logic pulse produced by the threshold detector are also shown as insets following the envelope detector and the threshold detector, respectively, in the system diagram of Figure 7-6. Figure 7-7. Photograph of asse

bled prototype receiver components. The high-T<sub>c</sub> superconductive chirp filter, r.5-ns-wide compressed pulse. The fast chirp generator (here an SLO) consists of a fast voltage-ramp generator that is used to drive a VCO, which generates the chirp waveform. This upchirp signal from the SLO is mixed with incoming signals and then passed through the YBCO Hamming-weighted compressor. Any compressed pulse generated by signals at the input of the system is passed on to an envelope detector, to a threshold detector, and then into a Si-ECL logic gate to produce an appropriate logic level to latch the counter value into the ECL latch. The output of the counter is placed into a first-in first-out (FIFO) buffer following an ECL-to-TTL level converter. The contents of the FIFO are read by a personal computer through a data interface card. The computer screen displays the frequency of the input signal by showing the most recent history of the frequency bins that have been occupied. The screen is updated every 0.25 s.

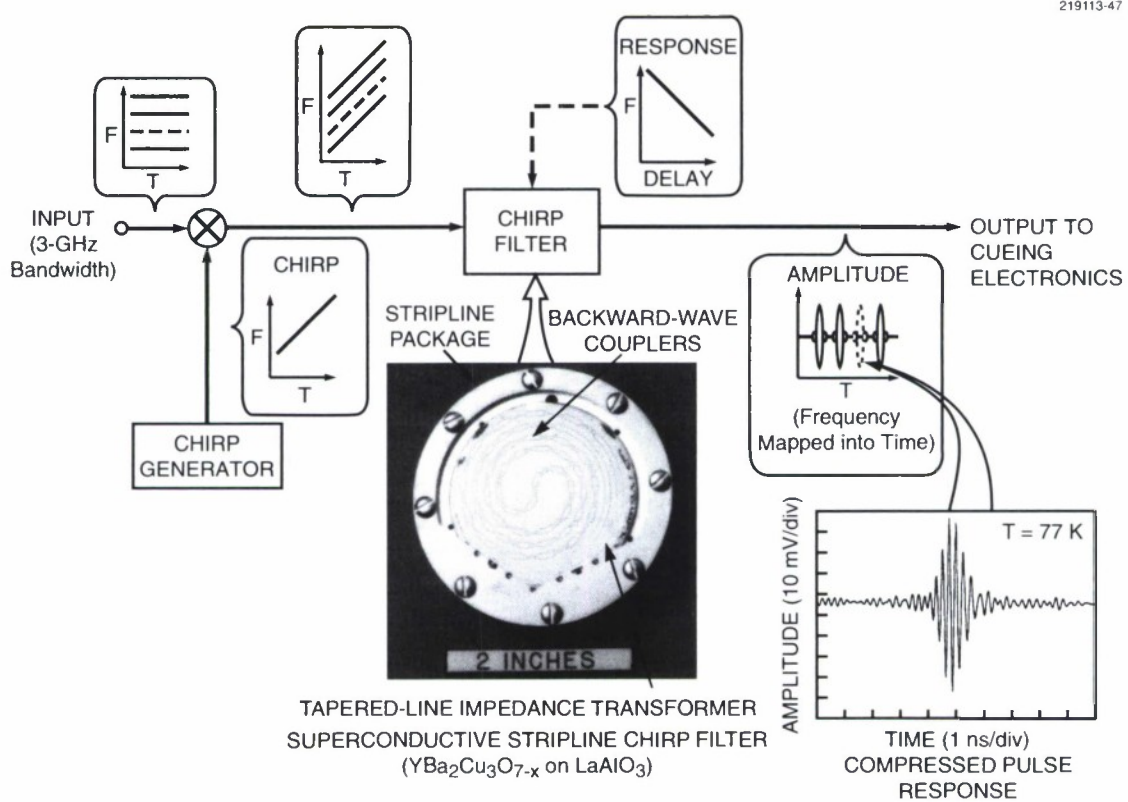


Figure 7-5. Block diagram of demonstration system intended for the Navy's Second High-Temperature Superconductor Space Experiment (HTSSE II). This is a multiply-convolve chirp-transform configuration for a compressive receiver.

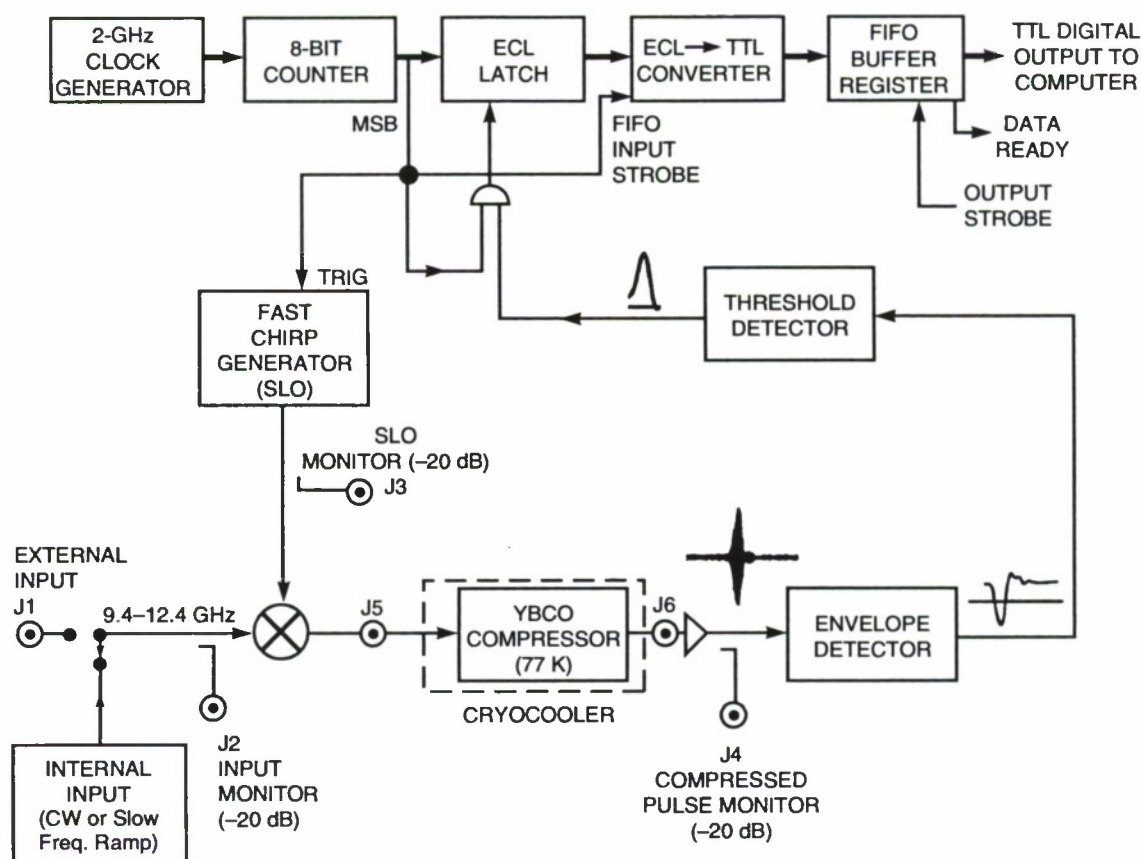


Figure 7-6. Detailed system diagram of the spectrum-analysis receiver for HTSSE II. The compressed-pulse signal, envelope-detected signal, and ECL-compatible logic signal are shown in the signal path.

The compressed pulse produced by passing a VCO-generated flat-weighted chirp waveform through a Hamming-weighted YBCO chirp filter operating at 72 K is shown as an inset above the compressed pulse monitor point J4 in Figure 7-6. The sidelobes (above the Hamming sidelobe level of -42 dB) on the compressed pulse generated in this way are produced by errors in the devices. The best error-sidelobe-level performance of the VCO/YBCO chirp filter combination is about -18 dB. This level is determined solely by errors in the chirp slope of the VCO and not by device errors in the YBCO chirp filter. The envelope-detected compressed pulse and the ECL logic pulse produced by the threshold detector are also shown as insets following the envelope detector and the threshold detector, respectively, in the system diagram of Figure 7-6.



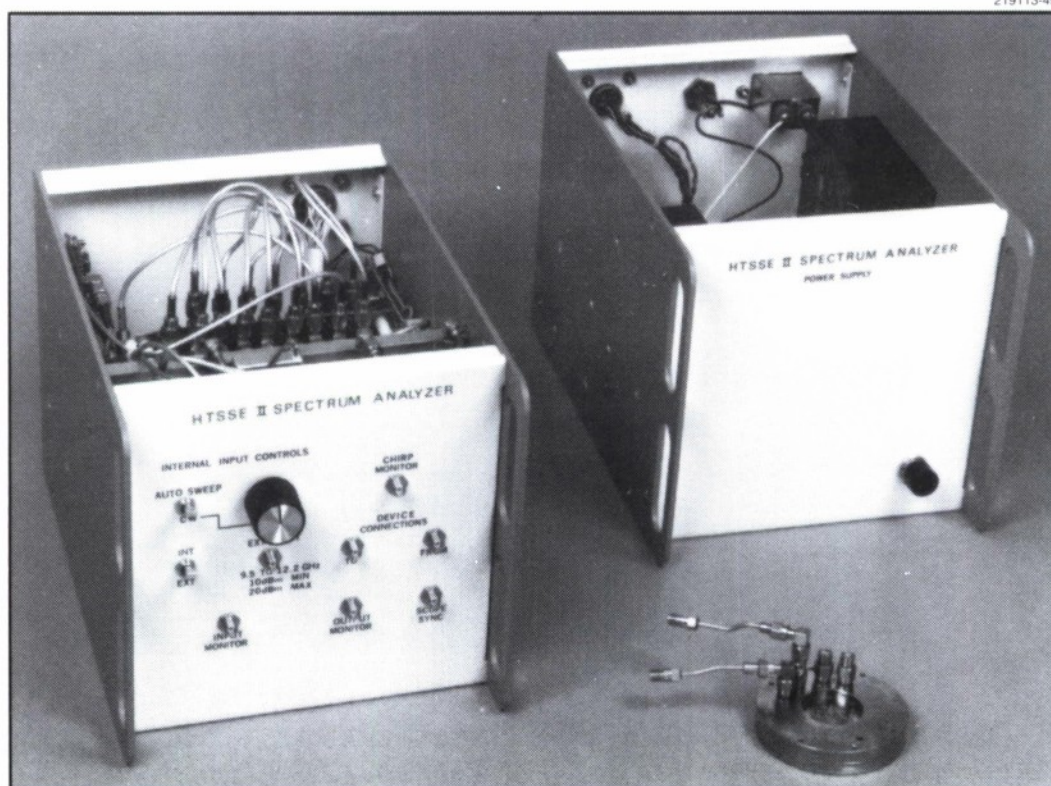


Figure 7-7. Photograph of assembled prototype receiver components. The high- $T_c$  superconductive chirp filter, room-temperature electronics box, and power supply box are shown.

Figure 7-7 is a photograph of the assembled prototype HTSSE II receiver showing the YBCO chirp filter, the room-temperature electronics box, and the power supply box. Test points are illustrated in the system diagram of Figure 7-6 and are visible on the room-temperature electronics box in Figure 7-7. The input signal monitor J2, the compressed pulse monitor J4, and the SLO (chirp generator) monitor J3 are all provided using 20-dB couplers. Points J5 and J6 are connections to and from the superconducting YBCO chirp filter. Figure 7-8, a snapshot of the computer display, shows the various frequency bins that were occupied when a CW tone was swept slowly across the analysis bandwidth of the receiver.

The 3-GHz instantaneous analysis bandwidth of this system is beyond that available with conventional technology. This prototype compressive receiver represents a very practical marriage between high- $T_c$  superconductivity and conventional semiconductor circuits.

W. G. Lyons      R. R. Boisvert  
D. R. Arsenault   T. C. L. G. Sollner  
M. M. Seaver

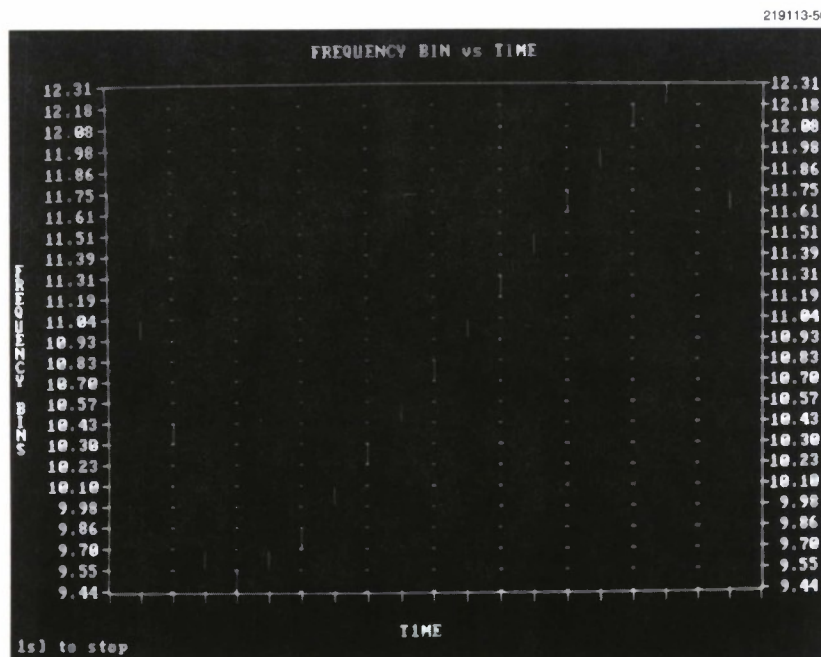


Figure 7-8. Screen display for slowly swept input signal. Frequency-bin data are updated at a slow rate of every 0.25 s so that a human operator can follow the display. The update rate could be much faster in an all-electronic system.

## REFERENCES

1. A. M. Chiang and M. L. Chuang, *IEEE J. Solid-State Circuits* **26**, 1894 (1991).
2. W. G. Lyons, R. S. Withers, J. M. Hamm, A. C. Anderson, P. M. Mankiewicz, M. L. O'Malley, R. E. Howard, R. R. Bonetti, A. E. Williams, and N. Newman, *1991 IEEE MTT-S Int. Microwave Symp. Dig.* (IEEE, New York, 1991), Vol. 3, p. 1227.
3. W. G. Lyons, R. S. Withers, J. M. Hamm, R. H. Mathews, B. J. Clifton, P. M. Mankiewicz, M. L. O'Malley, and N. Newman, *OSA Proc. Picosecond Electronics and Optoelectronics*, Vol. 9 (Optical Society of America, Washington, D.C., 1991), p. 167.
4. J. S. Herd, J. P. Kenney, K. G. Herd, W. G. Lyons, A. C. Anderson, P. M. Mankiewicz, and M. L. O'Malley, *1992 IEEE Antennas and Propagation Soc. Int. Symp. Dig.* (IEEE, New York, 1992), Vol. 2, p. 974.
5. W. G. Lyons, D. R. Arsenault, M. M. Seaver, R. R. Boisvert, T. C. L. G. Sollner, and R. S. Withers, to be published in *IEEE Trans. Appl. Supercond.* **3** (1993).
6. W. G. Lyons, R. S. Withers, J. M. Hamm, A. C. Anderson, D. E. Oates, P. M. Mankiewicz, M. L. O'Malley, R. R. Bonetti, A. E. Williams, and N. Newman, *AIP Conf. Proc. on Superconductivity and Its Applications*, Vol. 251 (American Institute of Physics, New York, 1992), p. 639.



